

**Surface-Mounted Metal-Organic Frameworks as the
Platform for Surface Science: Photoreactivity,
Electroreactivity, and Thermal Reactivity**

Zur Erlangung des akademischen Grades eines

DOKTORS DER NATURWISSENSCHAFTEN

(Dr. rer. nat.)

von der KIT-Fakultät für Chemie und Biowissenschaften des

Karlsruher Instituts für Technologie (KIT)

genehmigte

DISSERTATION

von

M.Sc. Jimin Song

aus

Dao County, Hunan, China

KIT-Dekan: Prof. Dr. Hans-Achim Wagenknecht

Referent: Prof. Dr. Christof Wöll

Korreferent: Prof. Dr. Stefan Bräse

Tag der mündlichen Prüfung: 20.07.2023

I declare hereby, that this dissertation represents the results of my own original research work from October 2020 to June 2023 in the Institute of Functional Interfaces (IFG), Karlsruhe Institute of Technology (KIT), under the supervision of Prof. Dr. Christof Wöll, and it has not been submitted to any other institution for another degree or qualification. All the text and figures that taken from other sources and references, are cited faithfully and properly.

Karlsruhe, 12.06.2023

Jimin Song

Abstract

Previously, researchers developed model systems such as single crystal metals or metal oxides to better understand real powder systems. However, questions still remain regarding the surface structure and reactivity of MOFs. Fortunately, surface-oriented SURMOFs provide an alternative approach for building model platforms to study these fundamental aspects of MOFs. This thesis focuses on organic photochemistry, electrocatalysis, and thermal pyrolysis of MOFs from a physical-chemical perspective by utilizing surface science techniques and SURMOF platforms. The goal of this thesis is to not only advance the knowledge of MOFs and SURMOFs, but also to showcase the power of surface science techniques and methodology in the field of chemical reactions. To achieve this, the thesis employs state-of-the-art UHV-IRRAS apparatus. A surface-mounted MOF (SURMOF) model system with azide side groups has been successfully fabricated and precisely monitored for chemical changes that occur during its operation. The comprehensive results acquired by combining IRRAS with in situ XRD, MS and XPS reveal that the photoreaction of azide is initiated by the formation of highly active nitrene groups that subsequently react with adjacent framework C=C bonds, yielding pyrrole derivatives via intramolecular amination. High quality ZIF-67 SURMOF was fabricated via a liquid phase layer-by-layer fashion and employed in OER for the first time. The catalytically active species, CoOOH, in the SURMOF derivatives were identified, offering insights into the structural transformation mechanisms and structure-performance relationships. With Ni and B additives, the overpotential decreased to 375 mV at 10 mA/cm². Also, in situ IRRAS and XPS were applied to reveal the structural transitions of ZIF-67 to carbon materials with N elements. NEXAFS data shows a final graphitic structure of the carbon materials after pyrolysis at 900 K. Hopefully, this thesis can broaden the fundamental understanding and application fields of MOF and SURMOF-based materials.

Zusammenfassung

Bisher haben Forscher Modellsysteme wie Einkristallmetalle oder Metalloxide entwickelt, um reale Pulversysteme besser zu verstehen. Es bestehen jedoch immer noch Fragen hinsichtlich der Oberflächenstruktur und Reaktivität von MOFs (Metallorganische Gerüstverbindungen). Glücklicherweise bieten oberflächenorientierte SURMOFs (surface-oriented SURMOFs) einen alternativen Ansatz für den Aufbau von Modellplattformen zur Untersuchung dieser grundlegenden Aspekte von MOFs. Diese Arbeit konzentriert sich auf die organische Photochemie, Elektrokatalyse und thermische Pyrolyse von MOFs aus einer physikalisch-chemischen Perspektive unter Verwendung von Oberflächenwissenschaftstechniken und SURMOF-Plattformen. Das Ziel dieser Arbeit besteht nicht nur darin, das Wissen über MOFs und SURMOFs zu erweitern, sondern auch die Leistungsfähigkeit von Oberflächenwissenschaftstechniken und -methoden im Bereich chemischer Reaktionen zu demonstrieren. Zu diesem Zweck verwendet die Arbeit eine hochmoderne UHV-IRRAS-Apparatur (Ultra-High-Vacuum Infrared Reflection Absorption Spectroscopy). Ein auf der Oberfläche montiertes MOF (SURMOF) Modellsystem mit Azid-Seitenketten wurde erfolgreich hergestellt und genau überwacht, um chemische Veränderungen während des Betriebs zu erfassen. Die umfassenden Ergebnisse, die durch die Kombination von IRRAS mit in situ XRD, MS und XPS erzielt wurden, zeigen, dass die Photoreaktion von Azid durch die Bildung von hochaktiven Nitren-Gruppen initiiert wird, die anschließend mit benachbarten C=C-Bindungen des Gerüsts reagieren und Pyrrol-Derivate durch intramolekulare Aminierung erzeugen. Ein hochwertiges ZIF-67-SURMOF wurde in einem Flüssigphasen-Schicht-für-Schicht-Verfahren hergestellt und erstmals in der Sauerstoffentwicklungskatalyse (OER) eingesetzt. Die katalytisch aktiven Spezies, CoOOH, in den SURMOF-Derivaten wurden identifiziert, was Einblicke in die Mechanismen der strukturellen Transformation und die Struktur-Leistungs-Beziehungen bietet. Durch Zugabe von Ni und B wurde die Überspannung auf 375 mV bei 10 mA/cm² reduziert. Zusätzlich wurden in situ IRRAS und XPS verwendet, um die strukturellen Übergänge von ZIF-67 zu kohlenstoffhaltigen Materialien mit Stickstoffelementen zu enthüllen. NEXAFS-Daten zeigen eine abschließende graphitische Struktur der kohlenstoffhaltigen Materialien nach Pyrolyse bei 900 K.

Hoffentlich kann diese Arbeit das grundlegende Verständnis und die Anwendungsfelder von auf MOF und SURMOF basierenden Materialien erweitern.

Contents

1	Introduction.....	- 1 -
1.1	MOF.....	- 1 -
1.2	SURMOF.....	- 5 -
1.2.1	From the first SURMOF HKUST-1 to beyond.....	- 5 -
1.2.2	Methods for the fabrication of SURMOF thin films.....	- 10 -
1.2.3	Characterization of SURMOF.....	- 16 -
1.2.4	Applications of SURMOF thin films.....	- 23 -
1.3	Chemical reactions within MOF and SURMOF.....	- 29 -
1.3.1	As reactants.....	- 29 -
1.3.2	As catalysts.....	- 33 -
2	Methods.....	- 40 -
2.1	Infrared spectroscopy.....	- 40 -
2.1.1	Theoretical background.....	- 40 -
2.1.2	Infrared reflection-absorption spectroscopy (IRRAS).....	- 42 -
2.2	RAMAN spectroscopy.....	- 44 -
2.3	X-ray diffraction.....	- 46 -
2.3.1	Theoretical background.....	- 46 -
2.3.2	X-ray diffraction of the MOF thin film: in plane and out of plane.....	- 47 -
2.4	AFM.....	- 48 -
2.5	SEM.....	- 48 -
2.6	Mass spectroscopy.....	- 48 -
2.7	Electrocatalytic OER.....	- 49 -
2.8	UHV apparatus.....	- 49 -
2.8.1	THEO.....	- 49 -
2.8.2	UHV-IRRAS.....	- 53 -
2.8.3	XPS.....	- 56 -
2.8.4	NEXAFS.....	- 57 -
3	Photo-activation of Azide inside Cu-DA-SBDC SURMOF Matrices.....	- 60 -
3.1	Introduction.....	- 60 -
3.2	Experimental.....	- 62 -
3.3	Results and discussion.....	- 64 -
3.3.1	Pristine film characterization.....	- 64 -
3.3.2	In situ photoreaction under IRRAS observation.....	- 66 -
3.3.3	Chemical and structural changes during photoreaction.....	- 70 -
3.3.4	Study of solvent effects.....	- 75 -
3.4	Conclusions.....	- 77 -
4	MOF-on-MOF Epitaxial Growth of ZIF-67 SURMOF for Electrocatalytic Water Oxidation (OER).....	- 79 -
4.1	Introduction.....	- 79 -
4.2	Experimental.....	- 81 -
4.2.1	Synthesis of ZIF-67 SURMOF.....	- 81 -
4.2.2	Catalytic performance tests.....	- 82 -
4.3	Results and discussion.....	- 83 -
4.3.1	ZIF-67 SURMOF before OER.....	- 83 -
4.3.2	Evolution of active sites during OER.....	- 89 -
4.3.3	Doping strategy for improving catalytic performance.....	- 95 -
4.4	Conclusions.....	- 96 -
5	Thermolysis of ZIF-67 SURMOF.....	- 97 -

5.1 Introduction.....	- 97 -
5.2 Experimental.....	- 98 -
5.3 Results and discussion	- 98 -
5.3.1 In situ pyrolysis of ZIF-67 and its IRRAS.....	- 98 -
5.3.2 Chemical species evolution.....	- 100 -
5.3 Conclusion	- 104 -
6 Summary.....	- 105 -
Abbreviation List	- 107 -
Acknowledgements.....	- 108 -
References.....	- 110 -

1 Introduction

1.1 MOF

Metal-organic frameworks (MOFs), also known as porous coordination polymers or PCPs, are a class of novel porous solid materials that were first introduced in the 1990s. With ultrahigh porosity (up to 90% free volume) and enormous internal surface areas exceeding 6000 m²/g, MOFs have emerged as one of the most prosperous research fields in recent years. The remarkable degree of variability for both the organic and inorganic components further enhances their potential applications.[1-3] Additionally, MOFs have already been produced in tons by major chemical companies such as BASF, Sigma-Aldrich, and Strem Chemical, indicating their practical significance in industrial-scale production. The unique properties of MOFs have opened up exciting applications in various fields, including gas storage, energy conversion, chemical sensing, drug delivery, proton conductivity, and catalysis. They have been utilized in oleo-chemical and textile industries, transportation, all-electric automobile prototypes, food packaging, and respiratory systems.[4-6] Overall, the exceptional properties and versatile applications of MOFs have made them a promising material for further research and practical use in various industries.

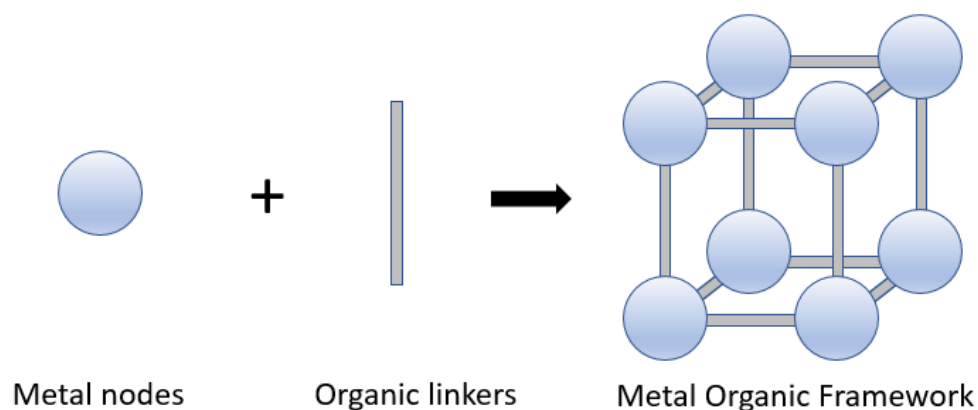


Figure 1.1 Structure of MOF.

The structure of MOFs (as shown in **Figure 1.1**) is composed of metal ions and organic ligands, which form building units known as secondary building units (SBUs). These SBUs are molecular complexes and cluster entities that repeat in three

dimensions to create a regular and periodic framework.[1, 7] The transformation of SBUs into extended porous networks using polytopic linkers enables the prediction of framework topology and the design and synthesis of a new class of porous materials with robust structures and high porosity.[8] To study MOFs, it is essential to consider the geometries of SBUs, their connectivity, and compositions. It is important to note that each metal ion does not necessarily connect to only one linker molecule, and 131 SBUs have been reported thus far. In fact, there are 131 SBUs reported so far. For instance, MOF-5 ($Zn_4O(BDC)_3$, BDC=1,4-benzenedicarboxylate) (as shown in **Figure 1.2**) is a good example that closely resembles **Figure 1.1**.^[9] It crystallizes in the cubic space group $Fm\bar{3}m$ (space group no. 225), with a yellow sphere representing the cavity. The Zn_4O nodes (SBU) are located at the eight corners of the cube and are connected linearly by terephthalate linkers. The carboxylate groups of the terephthalate linkers are connected to the outer four Zn^{2+} ions, with an O^{2-} ion at the center.

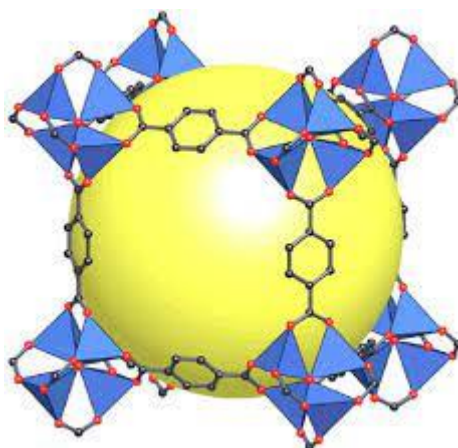


Figure 1.2 Structure of MOF-5.

The polynuclear nature of SBUs provides a stable and directional building unit for the design of robust crystalline materials with predetermined structures and properties. **Figure 1.3** shows the structural diversity of MOFs, which results from the wide range of accessible SBU geometries. When choosing suitable MOFs for various applications, such as gas adsorption, separation processes, sensors, and catalysis, it is crucial to consider the specific MOF structure, crystallinity, and porosity that arise from different SBUs due to their unique chemical nature.

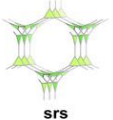
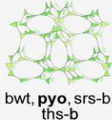

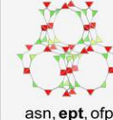
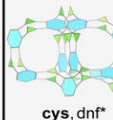
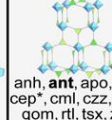
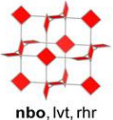
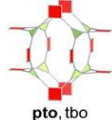

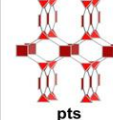
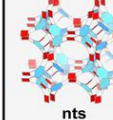
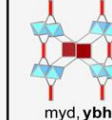
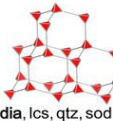
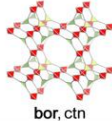
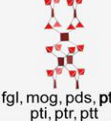

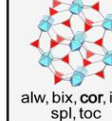
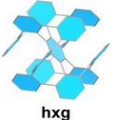
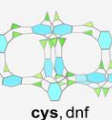
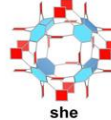
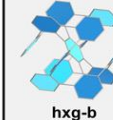
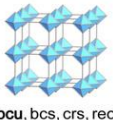
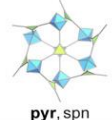
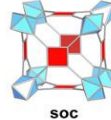
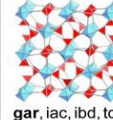
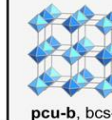
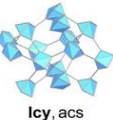

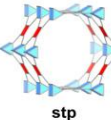
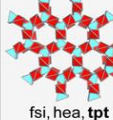
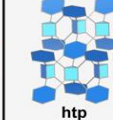
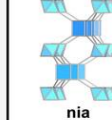
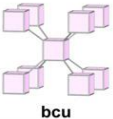
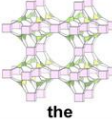
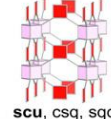

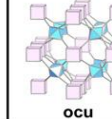
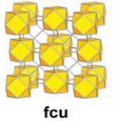
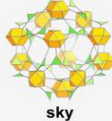
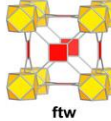
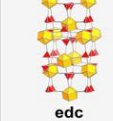
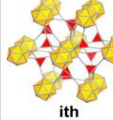
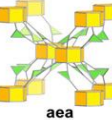
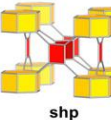
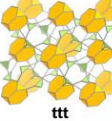
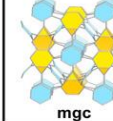
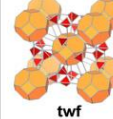
Building unit 1 \ Building unit 2	2-c Linear	3-c Triangle	4-c Square	4-c tet	6-c Hexagon	6-c oct
3-c Triangle	 srs	 bwt, pyo, srs-b, ths-b	 fjh, fmj, gee, iab, yac, yao	 asn, ept, ofp	 cys, dnf*	 anh, ant, apo, brk, cep*, cml, czz, eea, qom, rtl, tsx, zzz
4-c Square	 nbo, lvt, rhr	 pto, tbo	 cev, cdl, cdm, cdm, cds, cdz, mot, muo, qdl, qzd, ssd, sse, ssf, sst	 pts	 nts	 myd, ybh
4-c tet	 dia, lcs, qtz, sod	 bor, ctn	 fgl, mog, pds, pth, pti, ptr, ptt	 bnl, byl, cag, cbt, coe, crb, fel, icm, kea, lon, pcl, qtz-b, sca, tpd, ucn	-	 alw, bix, cor, ing, spl, toc
6-c Hexagon	 hxg	 cys, dnf	 she	-	 hxg-b	-
6-c oct	 pcu, bcs, crs, reo	 pyr, spn	 soc	 gar, iac, ibd, toc	-	 pcu-b, bcs-b
6-c trp	 lcy, acs	 ceq, dag, fmz, hwx, moo, sab, sit, ydq	 stp	 fsi, hea, tpt	 htp	 nia
8-c cub	 bcu	 the	 scu, csq, sqc	 flu	-	 ocu
12-c cuo	 fcu	 sky	 ftw	 edc	-	-
12-c ico	-	-	-	 ith	-	-
12-c hpr	-	 aea	 shp	-	-	-
12-c tte	-	 ttd	-	-	 mgc	-
24-c tro	-	-	-	 twf	-	-

Figure 1.3 The reticular table.[10]

In the early 1990s, the development of the molecularly-based field of crystal engineering prompted coordination chemists to shift their focus towards assembling organic and inorganic building blocks into porous structures. The zeolite, which is another porous solid structure, quickly became of interest to scientists working in the field of MOFs, as it had already been successfully applied in industry for decades. Consequently, chemists with a background in zeolites began to evaluate organic molecules not only as structure-directing agents but also as reactants, as part of the framework structure. The concept of solvothermal reaction conditions in zeolite chemistry is structure-oriented. To date, the creation of a vast chemical space has led to the discovery of more than 100,000 MOFs (**Figure 1.4**). This number is rapidly increasing in terms of topologies, structural types, building units, linkage chemistry, and functional groups. The main goal of MOF synthesis is to establish synthesis conditions that lead to the formation of defined inorganic substances, while ensuring that the building blocks of the organic linker remain stable during the synthesis. Additionally, the crystallization kinetics must be appropriate to allow for the desired stages of nucleation and growth.

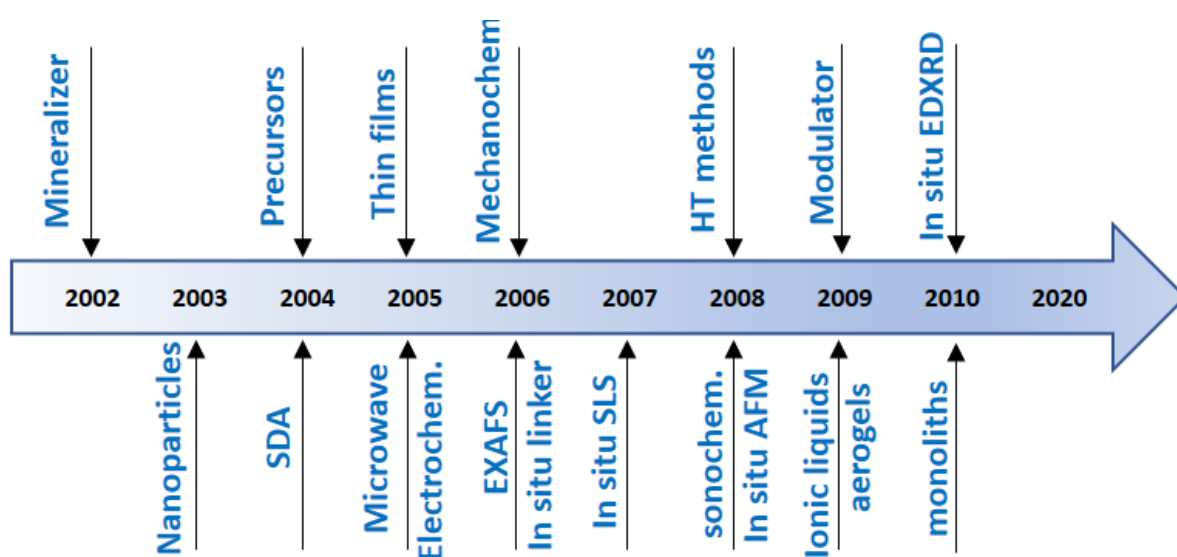


Figure 1.4 Historical developments in the synthesis of porous MOFs.[11]

In the last two decades, a variety of preparation methods have been employed to synthesize MOFs. These methods include the use of structure directing agents, ionic liquids, biphasic solvent mixtures, molecular precursor, or in situ linker synthesis.

More recently, computer-aided synthesis through machine learning has proved to be a valuable tool in predicting and accelerating the MOF discovery process.[12]

The versatile chemistry of MOFs allows for the design and preparation of the required framework by selecting appropriate metal ions and organic ligands. The size and shape of the cavity and channels connecting them can be adjusted by using different lengths and connectivity of organic ligands or metal or metal/carbonyl connectors. Furthermore, the chemical and physicochemical properties of MOFs can be modified not only by binding different functional groups to organic compounds prior to MOF assembly, but also through post-synthesis modification (PSM). MOFs can assemble organic junctions and metal or metal carbonyl nodes of higher subjects by combining molecular building blocks, especially two-bit building blocks, which means that the number of structures that can be achieved is almost limitless. Additionally, binary compounds can be created by modifying substantially any organic molecule with suitable coupling groups, such as carboxylic acid groups or pyridine units. Therefore, the number of possible MOF structures far exceeds the number of known structures.

1.2 SURMOF

SURMOF represents a new class of MOFs thin films. It can be used as the main structure of molecules or nanoparticles in gases, for example, storage systems, optical sensors, or catalytically active materials. Their geometric hole properties can be adjusted using external triggers such as lights. As a result, molecules can be captured in the pores and released again "push the button". SURMOF can also be chemically adjusted for storing pharmaceutical active substances in biology and medical fields. For example, implants can be coated with SURMOF, which are loaded with anti-inflammatory substances before use, and then these are released substances in the body exist in a slow and controlled speed and quantity.

1.2.1 From the first SURMOF HKUST-1 to beyond

For many advanced applications in nanotechnology, it is required that the nanomaterials are deposited on solid substrates to form films, such as in electronic, photonic, and sensing devices. As most MOFs present in the form of powders, there is an increasing demands of MOF thin films. There are several methods to fabricating MOF thin films: 1) *growth/deposition from solvothermal mother solutions*; 2) *direct*

oriented growth/deposition from solvothermal mother solutions; 3) microwave-induced thermal deposition; 4) colloidal deposition method; 5) electrochemical synthesis; 6) evaporation induced crystallization; 7) gel-layer synthesis; 8) layer-by-layer or liquid phase epitaxy (LPE)[13].

Among the all kinds of MOF thin films, there is one monolithic, crystalline, homogeneous, and highly oriented MOF thin films called surface mounted MOF thin films (SURMOF) via the 8) *layer-by-layer or liquid phase epitaxy (LPE)* method.[14] In 1937, Blodgett and I. Langmuir fabricated the multilayer organic barium stearate films via the layer-by-layer (lbl) firstly.[15] In 2007, for the first time, Wöll and his colleagues established a stepwise layer-by-layer (lbl) or liquid-phase epitaxy (LPE) growth process to produce crystalline MOF thin films (**Figure 1.5**).[16] In ordinary synthesis protocols of MOFs powders, the reactants (primary building blocks, typically two) are mixed together and reacted under solvothermal conditions. While in Wöll's contribution the substrate is immersed into solutions of the metal precursor or linker separately, in a sequential, stepwise fashion. Besides, unlike the synthesis of MOF powders usually carried out at elevated temperatures, in contrast, the layer by-layer fabrication of SURMOFs proceeds at room or low temperature.

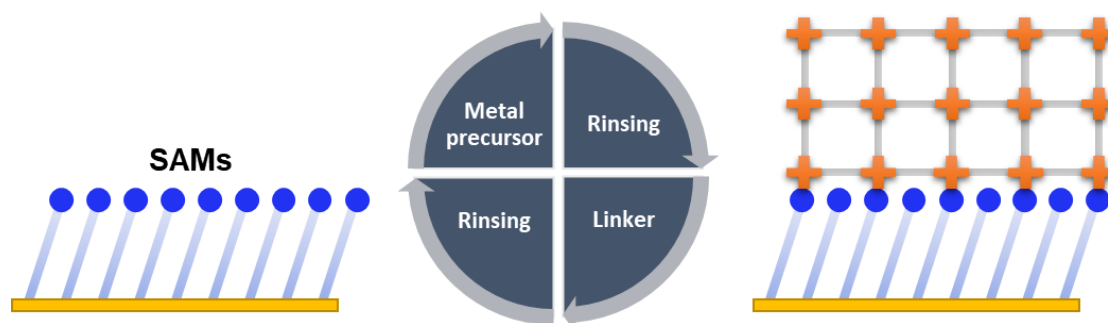


Figure 1.5 Layer-by-layer (lbl) synthesis of SURMOF on SAMs (self-assembled monolayers) pretreated substrates.

The HKUST-1 is a prototypical and classic SURMOF. HKUST-1 SURMOF can be grown on surface-functionalized Au-coated Si substrates by employing a layer-by-layer fashion. As one of the most-investigated and well-understood MOF materials, it offers a standard MOF model for initial and fundamental study in this field. The discovery of the first surface mounted frameworks thin films (SURMOF), HKUST-1, in 2007 marked the beginning of a new era in materials science. Since then, the family of SURMOF has grown significantly, with new materials being discovered and

synthesized at an unprecedented rate. **Table 1.1** shows the development of HKUST-1 SURMOF chronologically. And **Table 1.2** shows the SURMOF aside from HKUST-1. The development of new SURMOF materials with unique properties and applications is an exciting area of research, and it is expected to have a significant impact on science and technology in the coming years. The ability to control the properties of these materials at the atomic and molecular level offers unprecedented opportunities for the design of novel materials with tailored properties and functionalities.

Table 1.1 Development of HKUST-1 SURMOF.

Year	Sample	Fabrication method	Orientation	Contribution
2007	HKUST-1	Dipping	[100]	SURMOF fabrication[16]
2009	HKUST-1	Dipping	[100]/[111]	Growth mechanism[17]
2010	HKUST-1	Dipping	[100]	Growth mechanism[18]
2010	HKUST-1	Dipping	[100]	Guest loading[19]
2011	HKUST-1	Spray coating	[111]	SURMOF fabrication[20]
2012	HKUST-1	Spray coating	[100]	Control of defects[21]
2013	HKUST-1/[Cu(BDC)] _n	Spray coating	[100]	Dielectric; optical properties[22]
2013	HKUST-1	Spray coating	[111]	SAM patterning[23]
2014	HKUST-1/[Cu ₂ (NDC) ₂ (dabco)] _n	Pump coating	[111]/[001]	Heterostructure SURMOFs[24]
2014	HKUST-1	Spray coating	[100]	Guest loading[25]
2015	HKUST-1	Spray coating	[111]	Nanomechanical investigation[26]
2015	HKUST-1	Spray coating	[100]	Optical sensing[27]
2015	HKUST-1	dipping	[100]	Optical applications[28]
2015	HKUST-1	Spray coating	[111]	Loading; electrically conductive SURMOFs[29]
2016	HKUST-1	Spray coating	[100]	Anisotropic thermal expansion[30]
2016	HKUST-1	Pump coating	[100]	Resistive switching nanodevices[31]
2016	HKUST-1	Spray coating	[100]	Guest loading[32]
2017	HKUST-1	Dipping	[111]	Organic field-effect transistor[33]
2017	HKUST-1	Spray coating	[111]	Catalysis[34]
2017	HKUST-1	Dipping	[111]	Guest loading; photoswitching uptake[35]
2017	HKUST-1	Spray coating	[100]	Electrically conductive SURMOFs[36]

Table 1.1 Continued.

2017	HKUST-1	Spray coating	[111]	Loading; enantioselective adsorption[37]
2018	HKUST-1	Dipping	[111]	Morphology of SURMOFs[38]
2018	HKUST-1	Dipping	[100]	Growth mechanism[39]
2019	HKUST-1	Dipping	[111]	Biological applications[40]
2019	HKUST-1	Dipping	[100]	Guest loading conductivity[41]
2020	HKUST-1	Dipping	[100]/[111]	Optimized growth[42]
2020	HKUST-1	Spin coating	[111]	Dye adsorption; water oxidation[43]
2020	HKUST-1	Pump coating	[100]/[111]	Ambipolar resistive[44]
2020	HKUST-1	Dipping	[111]	SURMOF on polymer[45]
2020	HKUST-1	Dipping	[100]/[111]	Gas sorption[46]
2020	HKUST-1	Pump coating	[100]	Defect creation[47]
2021	HKUST-1/ZIF-8	Dipping	[001]	Adsorption[48]
2021	HKUST-1	Pump coating	[111]	SAM patterning[49]
2021	HKUST-1	Spray coating	[100]/[111]	Growth method[50]
2022	HKUST-1	Dipping	[111]	Hybrid electronics[51]
2022	HKUST-1	Spray coating	[001]	Conductive SURMOFs[52]
2023	HKUST-1	Spray coating	[100]	Optical resonator[53]

Table 1.2 Development of other SURMOFs.

Year	Sample	Fabrication method	Orientation	Contribution
2009	$[\text{Zn}_2(\text{BDC})_2(4,4'\text{-bipy})]_n$	Dipping	[001]	Controlling interpenetration[17]
2012	$[\text{Zn}_2((\text{p})\text{cam})_2(\text{dabco})]_n/[\text{Zn}_2((-)\text{cam})_2(\text{dabco})]_n$	Pump coating	[110]/[001]	Enantioselective adsorption[54]
2012	$[\text{Cu}_2(\text{NDC})_2(\text{dabco})]_n$	Pump coating	[001]	Selective modification[55]
2013	$[\text{Cu}_2(\text{NDC})_2(\text{dabco})]_n$	Dipping	[001]	Guest loading[56]
2013	$[\text{Cu}_2(\text{NH}_2\text{BDC})_2(\text{dabco})]_n$ -on- $[\text{Cu}_2(\text{BDC})_2(\text{dabco})]_n$	Pump coating	[001]	Heterostructured SURMOFs[57]
2013	$[\text{Cu}_2(\text{NH}_2\text{BDC})_2(\text{dabco})]_n$ -on- $[\text{Cu}_2(\text{BDC})_2(\text{dabco})]_n$	Pump coating	[001]	Post-synthetic modification[58]
2014	$[\text{Cu}_2(\text{AB-BPDC})_2(\text{BiPy})]_n$ -on- $[\text{Cu}_2(\text{BPDC})_2(\text{BiPy})]_n$	Pump coating	[001]	Photoswitching release molecular[59]
2014	$[\text{Cu}_2(\text{Dcam})_{2x}(\text{Lcam})_{2-2x}(\text{dabco})]_n$	Dipping	[001]/[110]	Chiral SURMOFs[60]

Table 1.2 Continued.

2014	$[\text{Zn}_4\text{O}(\text{dmcapz})_3]_n/[\text{Zn}_4\text{O}(\text{BD C})_3]_n$	Pump coating	[100]	Sorption[61]
2015	$[\text{Cu}_2(\text{F4BDC})_2(\text{dabco})]_n$	Dipping	[100]	Growth mechanism[62]
2015	$[\text{Zn}(\text{N}_3\text{-BPDC})_2(\text{dabco})]_n$	Spray	[001]	SAMs patterning[63]
2016	$[\text{Cu}_2(\text{atBDC})_2(\text{dabco})]_n/[\text{Cu}_2(\text{BDC})_2(\text{dabco})]_n$	Pump coating	[001]	Guest loading[64]
2016	ZIF-8	Dipping	[001]	Gas separation[65]
2016	$[\text{Zn}(2,20\text{-bipyridine-5,50-dicarboxylic acid}(\text{Re}(\text{CO})_3\text{Cl}))]_n$	Spray coating	[100]	Electrocatalytic device[66]
2018	$[\text{Zn}(3,9\text{-perylene dicarboxylic acid})]_n$	Spray coating	[001]	Guest loading; up-conversion[67]
2018	$[\text{Zn}(5,15\text{-bis}(4\text{-azidophenyl)-10,20-bis}(4\text{-carboxyphenyl)porphyrin})]_n$	Spray coating	[001]	Antimicrobial activity polymer[68]
2017	$[\text{Zn}_2(\text{BA-BDC})_2(\text{dabco})]_n$	Pump coating	[100]	Polymer gels[69]
2018	$[\text{Zn}(\text{TCPP})]_n$	Pump coating	[001]	Solar cells[70]
2018	$[\text{Zn}(\text{TPE-BDC})]_n$	Spin coating	[010]	Controlling oxidative photocyclization[71]
2018	$[\text{Cu}_2(\text{BDC})_2]_n/[\text{Zn}_2(\text{BDC})_2]_n$	Spray coating	[010]	Oxidative polymerization[72]
2019	$[\text{Co}(\text{TCPP})]_n$	Spin coating	[011]	Nonlinear optical application[73]
2019	MOF-76 ($[\text{Ln}(\text{BTC})]_n$)	Pump coating	[001]	Tunable energy transfer[74]
2019	$[\text{Ni}/\text{Co}(\text{BDC})]_n$	Pump coating	[200]	Electrocatalysis[75]
2019	UiO-66 ($[\text{Zr}_6\text{O}_4(\text{BDC})]_n$)	Pump coating	[510]	Growth method[76]
2019	$[\text{Cu}_2(\text{BDC})_2(\text{bipy})]_n$	Pump coating	[100]/[001]	Growth mechanism[77]
2019	$[\text{Cu}_2(\text{BDC})_2(\text{dabco})]_n/[\text{Cu}_2(\text{C}_4\text{H}_4\text{BDC})_2(\text{dabco})]_n$	Pump coating	[100]/[001]	Growth mechanism by mixing linkers strategy[78]
2019	$[\text{Zn}(\text{porphyrin linkers})]_n$	Spin coating	[010]	Computational screening porphyrinic linkers[79]
2019	$[\text{Zn}_2(\text{Lcam})_2\text{DAP}]_n$	Pump coating	[001]	Circularly polarized luminescence[80]

Table 1.2 Continued.

2019	[Cu ₂ (DCam) ₂ (AzoBiPyB)] _n	Dipping	[001]	Photoswitching enantioselectivity[81]
2020	[Cu ₂ (e-BPDC) ₂ (dabco)] _n	Dipping	[100]	Photomodulated conductive SURMOFs[82]
2020	[Cu ₂ (FBDC) ₂ (dabco)] _n	Dipping	[001]	Synthetic conditions[83]
2020	[Cu(BDC)] _n	Spray coating	[001]	Conductive SURMOFs[84]
2020	[Zn(DPA-TPE)] _n	Spin coating	[010]	Optical applications[85]
2021	[Cu ₂ (BDC) ₂ (dabco)] _n / [Cu ₂ (adc) ₂ (dabco)] _n	Dipping	[001]	Photoswitching conductive SURMOFs[86]
2021	[Cu(QPDC)] _n	Spray coating	[001]	Encapsulation of Au55 clusters[87]
2021	[Cu(TCPP)] _n	Dipping	[001]	Optical limiting[88]
2021	[Cu ₃ (HHTP) ₂] _n	Spray coating	[001]	Conductive SURMOFs[89]
2021	[Zn(cNDIs)] _n /[Zn(TPE)] _n	Spin coating	[010]	Photoinduced delamination[90]
2022	[Zn(bianthryl linker)] _n	Spin coating	[010]	Photoinduced topotactic transformation[91]
2022	[Cu ₃ (HHTP) ₂] _n	Spray coating	[001]	Growth mechanism[92]
2023	MIL-68(In)	Pump coating	[010]	Optical sensing[93]

1.2.2 Methods for the fabrication of SURMOF thin films

The first example of SURMOF was conducted by hand dipping, manually. It's a simple and straightforward method. However, it takes a lot of labor and time. The complete for the first SURMOF HKUST-1 sample took 3 days. In this regard, automated robot fabrication process entered. It provides easy and accurate control of the operation times and greatly increases the reproducibility of SURMOF syntheses. In addition, different methods have been developed to satisfy the specific needs for different samples. In recent years, new methods including the dipping, spraying, pumping, and spin coating methods, and the quartz crystal microbalance (QCM) system-based method have been developed.[94]

1.2.2.1 Self-assembled monolayers (SAMs) on Surfaces

In principle, SURMOFs can be grown on any smooth and functionalized substrate surfaces. However, only a limited number of solid materials, such as gold, silver, silicon, alumina, glass, quartz glass, FTO, and metallic oxide, have been successfully used to prepare SURMOFs. A range of surface treatments are required for all substrates to meet the conditions of growing different MOFs on the substrate surface. However, inhomogeneous, mixed-oriented, and polycrystalline MOFs will be obtained on the substrate with pronounced surface defects and relatively high roughness.

In order to control the surface properties, growth of SURMOFs requires surface functional group to bond with the metal ions chemically. Bare surfaces adsorb tend to be covered by organic molecules and oxidic layers from the atmosphere to lower free energy. These randomly adsorbed organic molecules on surfaces, however, lack of specific chemical functionality. Thus, no reproducible physical properties (conductivity, wettability, passivation etc.) could be guaranteed. Self-assembled monolayers (SAMs) on surfaces can provide a well-defined orientation of identical molecules as a 2D crystal in form of a monolayer. Convenient, simple and flexible system with SAMs are accessible to tailor the interfacial properties of metals, metal oxides, polymers and semiconductors.

As the Chinese proverb goes, "If the upper beam is crooked, the one below is necessarily so." So it is the same with the construction of SURMOF. The structural quality of the SAMs for the SURMOF deposition process plays a crucial role. Low-quality SAMs with a high density of defects, contaminations or structural defects can result in a low quality of the deposited MOF and even in the failure to obtain the growth of crystalline structures.[95] Selection of proper SAMs is determined by the specific substrates. Gold, silver, silicon, silicon oxide, glass, quartz, alumina, titanium, titanium oxide, calcium fluoride, indium tin oxide, and fluorine doped tin oxide, and soft materials like plastics, papers, and textiles are plausible as the substrates for SURMOF synthesis.[96, 97] In general, any solid material with coordinating functional groups can be served as SURMOF substrates, which can provide a seeding and binding layer sufficient to anchor the deposited metal ions or linkers in the first growth step. Depending on which substrates are used and which

functional groups are needed, the functionalization of substrate can be varied (**Figure 1.6**). For a metal substrate like gold, thiol based chemical functionalization is the proven choice. The gold surface is soaked into an ethanol solution of thiol-terminated molecules such as 16-mercaptohexadecanoic acid (MHDA), (4-(4- pyridyl) phenyl)-methanethiol (PP1) or 11-mercapto-1-undecanol (MUD). The thiol groups react covalently with gold to form a self-assembled monolayer (SAM) ($\text{RSH} + \text{Au} \rightarrow \text{RS-Au} + 1/2\text{H}_2$). For some other nonmetallic materials, plasma treatment can be used to clean the surface as well as increase the density of surface hydroxyl groups. This can also be achieved by a chemical process (e.g. cleaning with piranha solution). To obtain carboxyl groups, the hydroxyl layer can be reacted with 11-(triethoxysilyl) undecanal. The now aldehyde groups presenting surface can be oxidized by potassium permanganate to form the carboxyl groups surface.

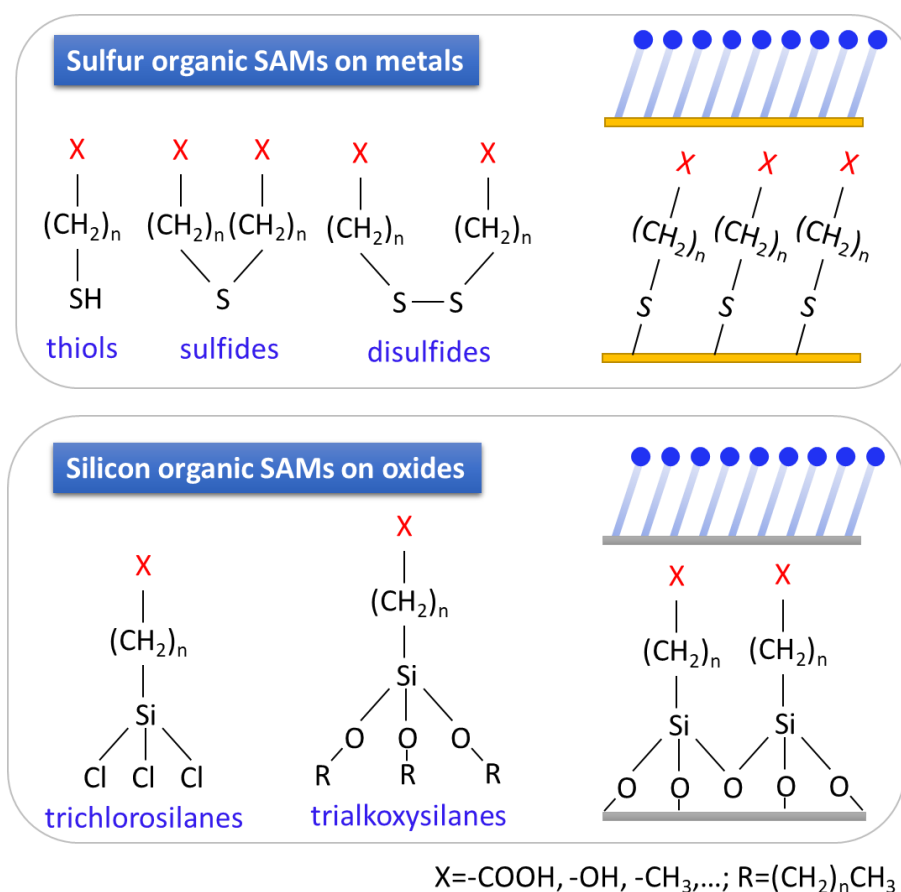


Figure 1.6 Self-assembled monolayers (SAMs) on Surfaces.

1.2.2.2 Dip-coating strategy

Dip coating is a widely used classic deposition technique used to obtain nanometric films. In the dip-coating method, the functionalized substrate is immersed sequentially

in three different solutions (metal salts, organic ligands and rinsing solutions) as shown in **Figure 1.7**.^[16] Previously, this process was conducted by hand then developed with an automatic robot method. The precise control of the immersion speed, the immersion time and the withdrawal speed influence the depth and the characteristics of the resultant coating. For example, in the first step of HKUST-1 synthesis, the modified substrate is added to the Cu^{2+} solution (copper acetate in ethanol), where Cu-dimer ions bind to carboxylate groups on the surface of the organic film. Therefore, these groups are fixed on the substrate. In the second step, the substrate is rinsed with a solvent (ethanol), then brought into contact with the ligand solution (in this case 1,3,5-benzyltricarboxylic acid, H_3BTC , ethanol solution) and rinsed again. By subsequent replicates and alternating immersion in metal ion solutions and ligand molecular solutions, three-dimensional SURMOF is epitaxially grown layer by layer (LBL).

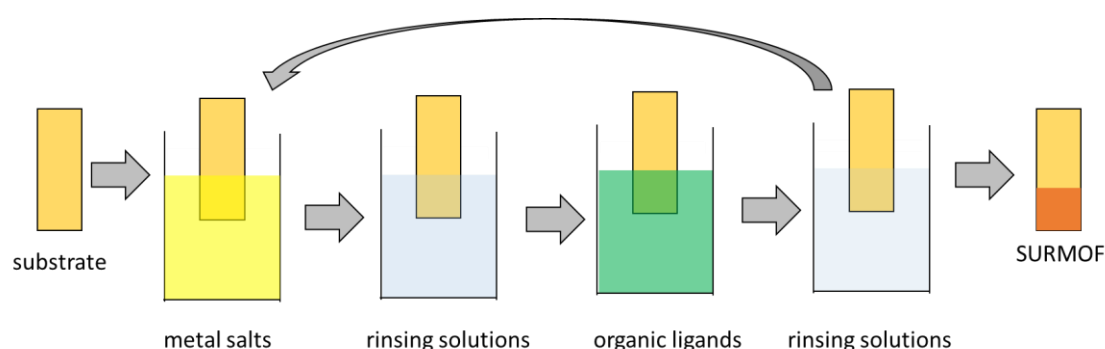


Figure 1.7 Dip coating.

1.2.3.3 Pump-coating strategy

The pump-coating method is one of the standard techniques for SURMOF preparation. A typical setup of pump system is shown in **Figure 1.8**.^[98] Instead of moving the substrate to each solutions, the solutions of metal salts, rinsing and organic ligands are brought to contact with the substrate through pumps, respectively. The excess of liquid each metal salts, organic ligands or rinsing solvent solutions will be drained from the surface after keeping with controlled volume and immersion time. All the steps are performed automatically by a software program. The substrate is kept in a pumping reactor with water-bath heating under desired temperature during the synthesis. Depending on whether the synthesis is sensitive to moisture and ambient atmosphere, the pumping reactor can be designed as open or closed cell with respect to the air.

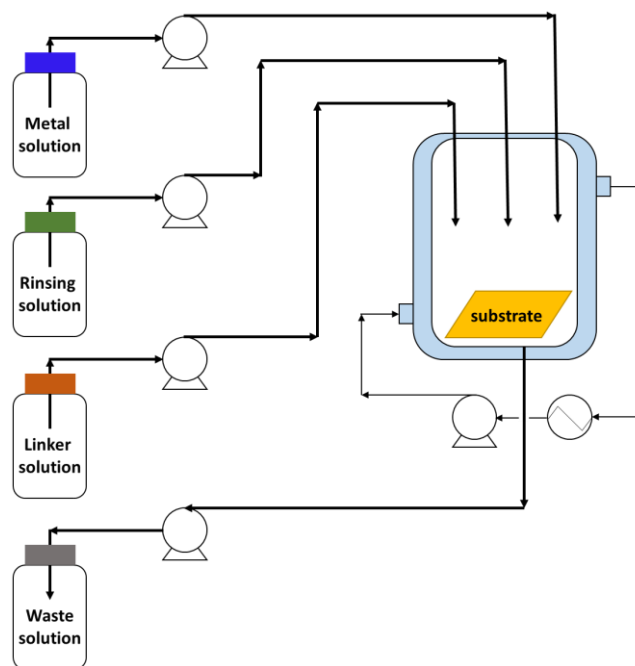


Figure 1.8 Pump coating.

1.2.3.4 Spray-coating strategy

Different from immersing the substrate in different metal precursor and linker solutions, in the spray-coating these solutions can be sprayed with a high-pressure sprayer. It is a high throughput approach, reducing the coating time from several minutes to a few seconds. It is quite often that preparing coatings with thicknesses exceeding 100 nm. This thickness, which for a typical MOF material corresponds to about 100 layers, requires 400 different immersion cycles. Even with an automatized pump system, the fabrication of a SURMOF requires a time period on the order of three days. For many applications, in particular those related to separation, at least one μm is required for the mechanical stability, which takes 30 days in this case.

Figure 1.9 shows a typical nozzle spray system. Carried by the flowing gas through a small nozzle, an aerosol of solutions is generated. Droplets of the aerosol hit the targeted substrate, then thin films deposit at the solid–liquid interfaces (LPE process). Three nozzles are responsible for metal salts, organic ligands and rinsing solvent, respectively. For the HKUST-1, the spray time are only 10–20 s for metal salts and ligand solutions while the spray time of rinsing step is 5 s.[20]

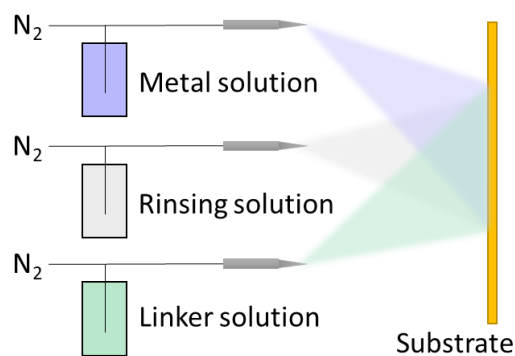


Figure 1.9 Spray coating.

1.2.3.5 Spin-coating strategy

Spin coating takes advantage of centrifugal force to spread uniform thin films on flat substrates (**Figure 1.10**). Usually volatile and evaporates solvent are applied during deposition. Firstly, a solution of metal ions is dispensed onto the center of the substrate, which is then rotated at high speed. Rotation continues until the excess solution spins off the substrate then the film is left on the substrate. Then the substrate is cleaned via the injection of micro drops of rinsing solvent. The same procedure is repeated for the organic ligand solution and rinsing step. This method offers substantial advantages and a great prospective due to its associated short growth time and lessened chemicals consumption.

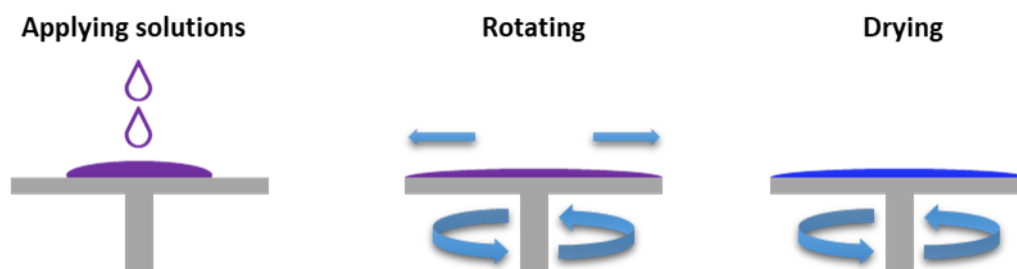


Figure 1.10 Spin coating.

1.2.3.6 Guest encapsulation

The same as MOF, the SURMOF is born with crystalline micropores, providing void for loading metal ions, dye molecules, coordination polymers and nanoparticles (**Figure 1.11**). Generally, there are three strategies for guest encapsulation: (a) *direct encapsulation strategy*; (b) *stepwise encapsulation strategy*, (c) *epitaxial encapsulation strategy*. Before the loading, SURMOF has to be activated in a flowing inert gas environment or vacuum under high temperature, to remove the residual molecules within during synthesis or absorption from the atmosphere.[99]

- (a) *Direct encapsulation strategy.* The as-activated SURMOF is treated with guest directly in liquid or gas phase. Wöll et al. reported a $\text{La}(\text{OTf})_3$ loaded into $\text{Cu}_3(\text{BTC})_2$ SURMOF via a solution impregnation method (one of direct encapsulation method). [25]
- (b) *Stepwise encapsulation strategy.* During the synthesis of some nanoparticles, the growth of particle size can be very fast. Thus make it hard to load these nanoparticles with desired small size. Adopting stepwise strategy, firstly loading part of precursors of the nanoparticles into the SURMOF, then introducing the other, the synthesis of nanoparticles takes place inside the pores of SURMOF. Through the stepwise approach, MAPbI_2X QDs are loaded successfully into the pores of MOF thin film.[64]
- (c) *Epitaxial encapsulation strategy.* In this method, nanoparticles are mixed with the precursor solutions, metal ions or organic linkers. Particle size larger than the SURMOF pore window length can be achieved in this way. Applying the epitaxial encapsulation method during pump coating, a photochromic molecule azobenzene loaded MOF HKUST-1 with high oriented and homogeneous thin film.[100]

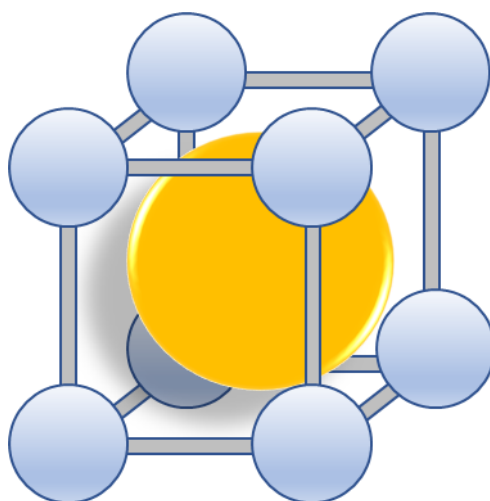


Figure 1.11 Encapsulating functional guest species in SURMOF thin film.

1.2.3 Characterization of SURMOF

1.2.1.1 Control over SURMOF growth direction

The orientation of SURMOFs can be controlled by the substrate surface functionalization. During the synthesis, the first nucleation of metal ions on the

substrates surface at the first deposition cycle determines the growing facets of SURMOF. A schematic view of this scenario is shown in **Figure 1.12a**.

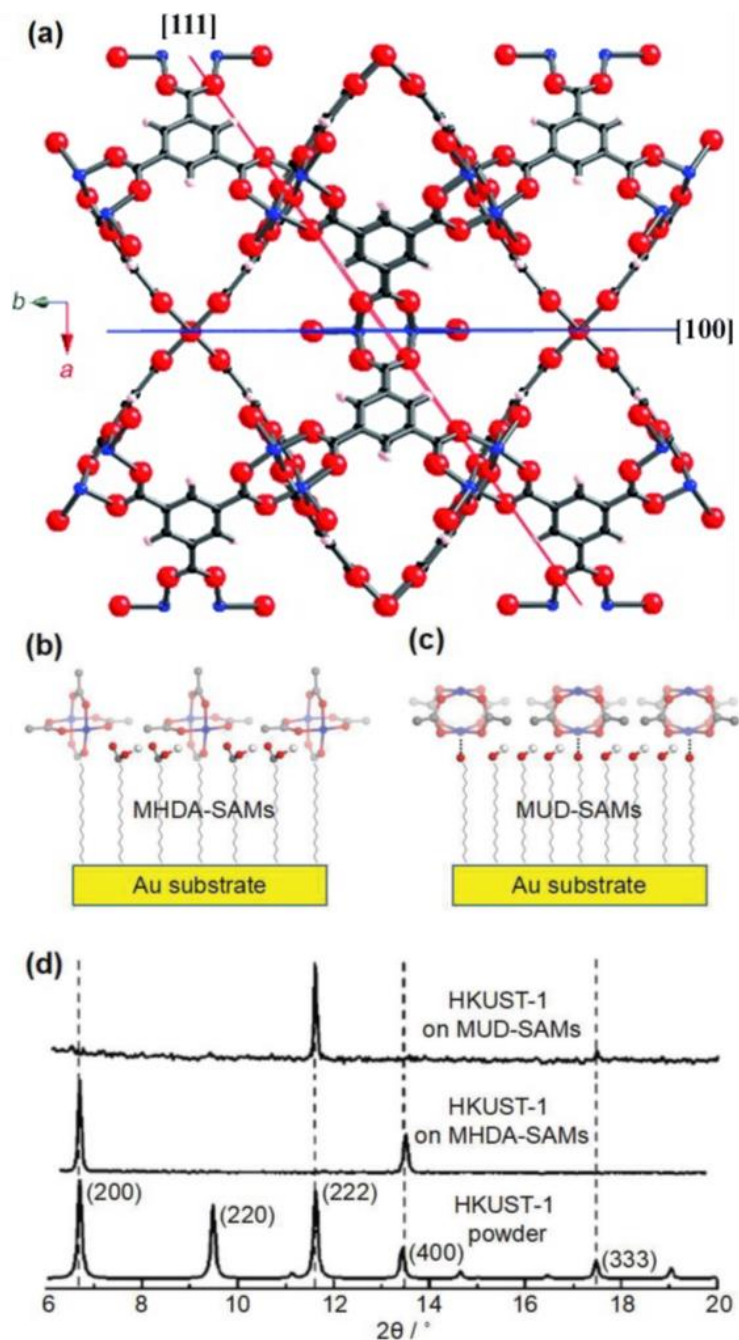


Figure 1.12 a) Crystal structure of HKUST-1. b) Paddle-wheel unit grafted to MHDA SAMs with COOH-terminated functional group. c) Paddle-wheel unit grafted on MUD SAMs with OH-terminated functional group d) Comparison of X-ray diffraction patterns recorded from HKUST-1 powder, HKUST-1 SURMOFs grown on MHDA-SAMs modified gold substrate, and HKUST-1 SURMOFs grown on MUD-SAMs modified gold substrate. (carbon: dark gray ball, oxygen: red ball, copper: blue ball, and hydrogen: gray ball). Modified from Ref[101].

Each 1,3,5-benzenetricarboxylic acid (H_3btc) consists the linker of HKUST-1. While for the metal node, it comprises a Cu(II) dimer, or so called copper paddle wheel

(PW), to which four carboxylate groups are bonded. The two axial positions of the metal dimer are unoccupied and can bind H₂O, CO, or pyridyl groups. The orientation of the PW can be tuned along with different directions. Growing on the COOH groups gives a standup PW orientation (**Figure 1.12b**), and on the OH groups yields a lying down orientation instead (**Figure 1.12c**), as verified by XRD (**Figure 1.12d**).

1.2.1.2 In situ observation of the layer-by-layer growth

A particular advantage of the layer-by-layer method, is the possibility to monitor the deposition of both ligands and coupling units. Not only ex situ using the methods just mentioned, but also in situ, employing either surface plasmon resonance (SPR) spectroscopy or a quartz crystal microbalance (QCM). **Figure 1.13** shows the in-situ growth of HKUST-1 SURMOF thin films via the observation from a quartz crystal microbalance (QCM). The two components, copper(II)acetate (Cu(ac)₂) and 1,3,5-benzenetricarboxylic acid (H₃btc), were separately dissolved in ethanol and the substrate was immersed into each solution in a cyclic way. Each immersion was followed by rinsing with pure ethanol. By starting with Cu(ac)₂, a linear increase of thickness of the deposited HKUST-1 layer with the number of (alternating) immersion cycles in Cu(ac)₂ and H₃btc is observed when measuring the thickness of the deposited films. For each immersion in linkers or metal precursors, an increase of mass signal was observed. This evidenced the step-by-step growth of SURMOF thin films. This LPE-method has been used successfully for the controlled and selective growth of many different types of MOFs including HKUST-1, Cu₂(ndc)₂(dabco), Cu₂(bdc)₂(dabco) and Zn₂(bdc)₂(dabco) (dabco=1,4-diazabicyclo[2.2.2]octane), ndc=1,4-naphthalenedicarboxylate).[102]

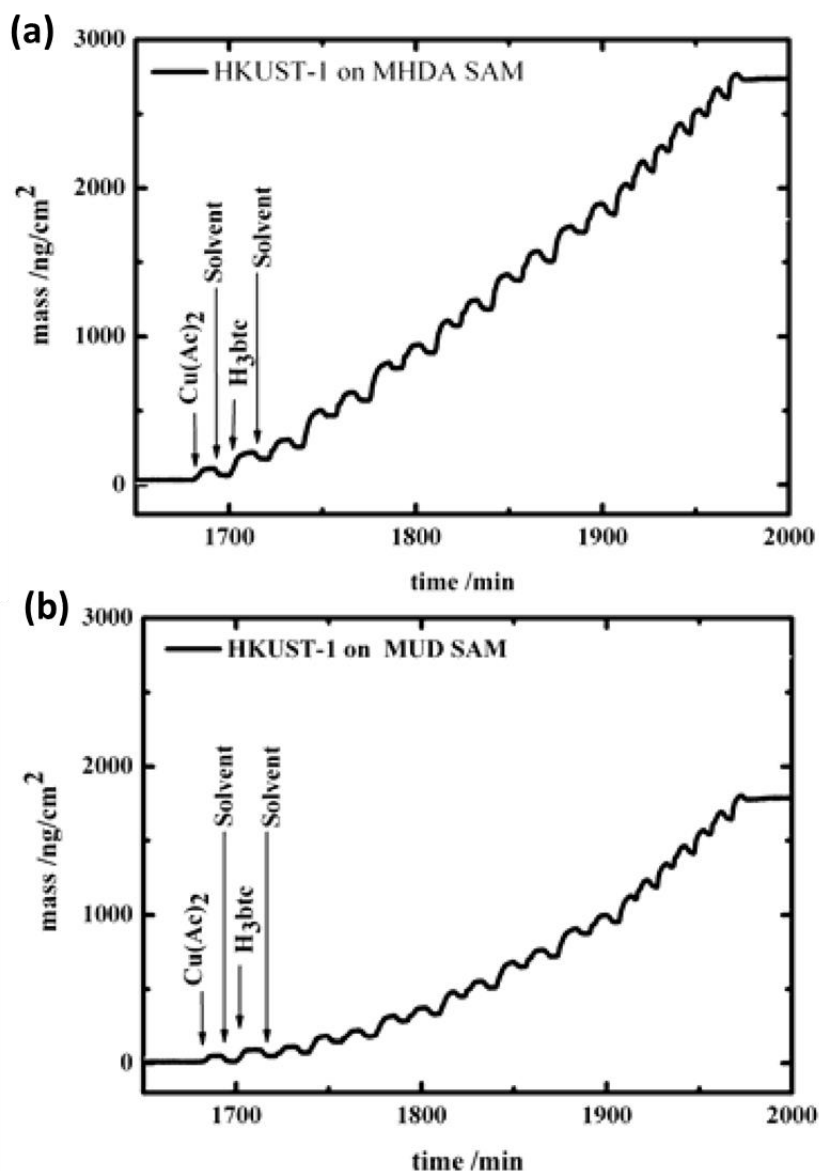


Figure 1.13 QCM signal as a function of time recorded in situ during sequential injections of Cu(Ac)₂, ethanol and H₃btc on the QCM substrate covered by a MHDA SAM (a), and a MUD SAM (b).[102]

1.2.1.3 Control over thin film thickness

As the illustration of stepwise mass increasing in QCM, it is also possible to control the thickness of the thin film. For each cycle of deposition, a 0.68 nm increase in thickness is expected in HKUST-1 SURMOF (**Figure 1.14a**) along the [100] direction when prepared on an MHDA -COOH terminated substrate.

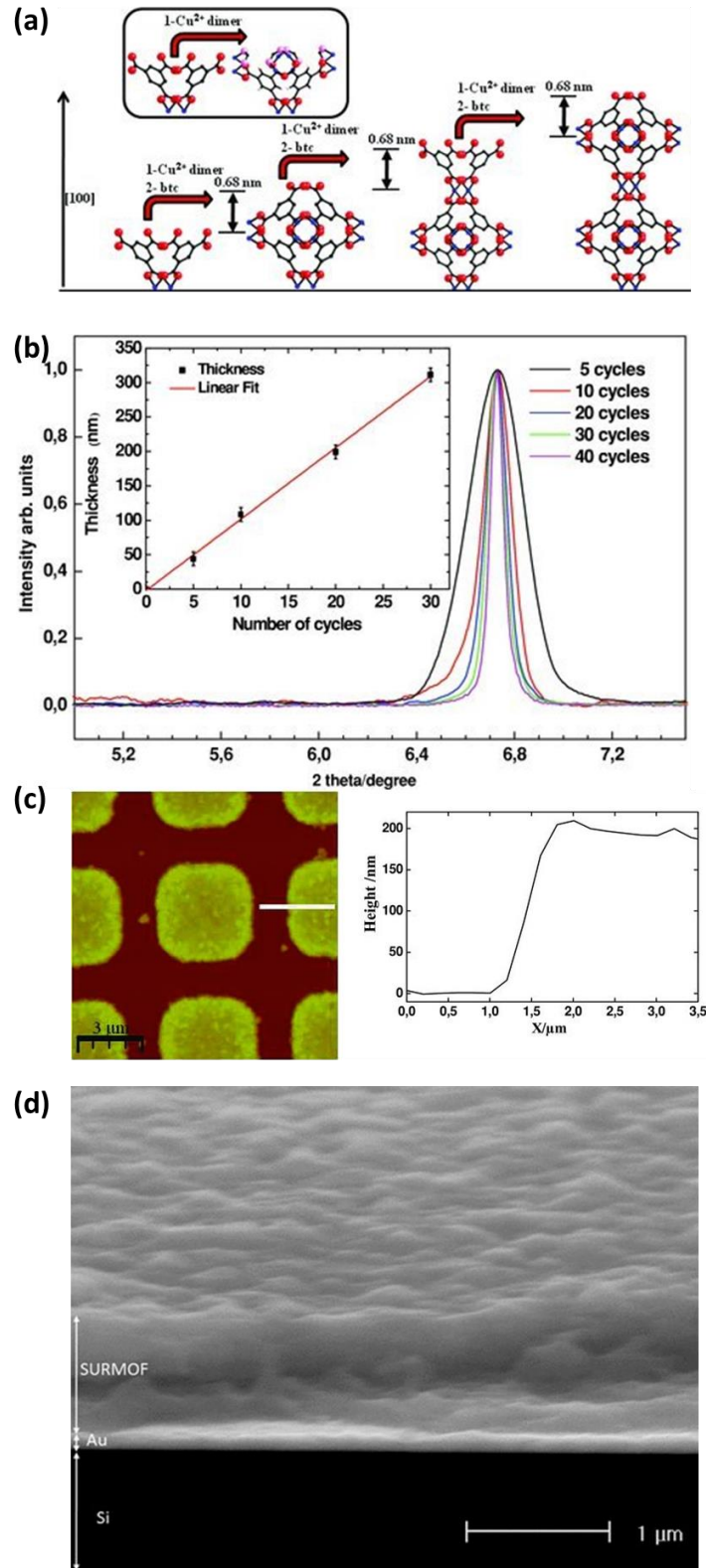


Figure 1.14 a) Fundamental steps in the liquid phase epitaxy of $\text{Cu}_3(\text{btc})_2 \cdot n\text{H}_2\text{O}$ along the [100] direction. b) Line profile of the HKUST-I SURMOF (200) diffraction peaks (fwhm) for different numbers of deposition cycles. c) AFM image of HKUST-1 SURMOF (20 cycles). d) A cross-section scanning electron micrograph of HKUST-1 SURMOF. Modified from Ref[20].

In **Figure 1.14b** presents profiles of the (200) XRD peaks of HKUST-1 SURMOF, measured with an increasing number of deposition cycles. With increasing number of cycles, the peak width Δ decreases clearly. Using the expression: $\Delta = \lambda/(N*d*\cos \theta)$, thickness of the deposited SURMOFs can be calculated(**Figure 1.14b** insterted). λ denotes the wavelength of the X-ray radiation, N the number of the MOF lattice planes, d the interplanar distance, and θ the diffraction angle. AFM measurements (**Figure 1.14c**) yield results consistent with those obtained from the XRD profile analysis. Selectively grown MOF platelets on a patterned SAM substrate, the thickness is determined to be 200 nm for 20 deposition cycles. Scanning electron microscopy (SEM) cross section images (**Figure 1.14d**) demonstrate also the thickness and the homogeneity of the deposited layers.

1.2.1.4 Surface science perceptions on HKUST-1 SURMOF

As mentioned earlier, one notable feature of SURMOF is their potential as a model system for studying surface properties. Involving both physical and chemical analysis techniques, the study and analysis of surfaces provide fundamental understanding of SURMOF. By using high-resolution ultrahigh vacuum infrared spectroscopy (UHV-FTIRS), active sites and reaction mechanisms in CO oxidation over HKUST-1 SURMOF were systematically investigated. For the pristine HKUST-1 SURMOF with CO adsorption, the intrinsic Cu^{2+} sites (2179 cm^{-1}) was the predominant species in HKUST-1 with a small amount of native Cu^+ defects as minor species (2125 cm^{-1}).^[103] Upon purging O_2 , the CO peaks vanished, indicating CO oxidation even at temperatures as low as 105 K. Notably, this reaction takes place only on the intrinsic Cu^{2+} CUS, whereas, rather unexpectedly, the Cu^+ defect sites are inactive for the low-temperature CO oxidation. The mechanism different from metal oxides or oxide-supported metal NPs was proposed. In the presence of pre-adsorbed CO the impinging O_2 molecule is activated, thereafter, interacts with two iso-carbonyl species at neighboring CUS to yield two CO_2 molecules.

For pristine HKUST-1 SURMOF there is a small amount ($\sim 4\%$) of Cu^+ species (defects), as shown in XPS (**Figure 1.15a**). Upon heating, the temperature-induced creation of Cu^+ defects were clearly observed. The intentional creation of defects

inside SURMOFs provides alternative for tuning the electronic structure and catalytic properties of MOF materials.

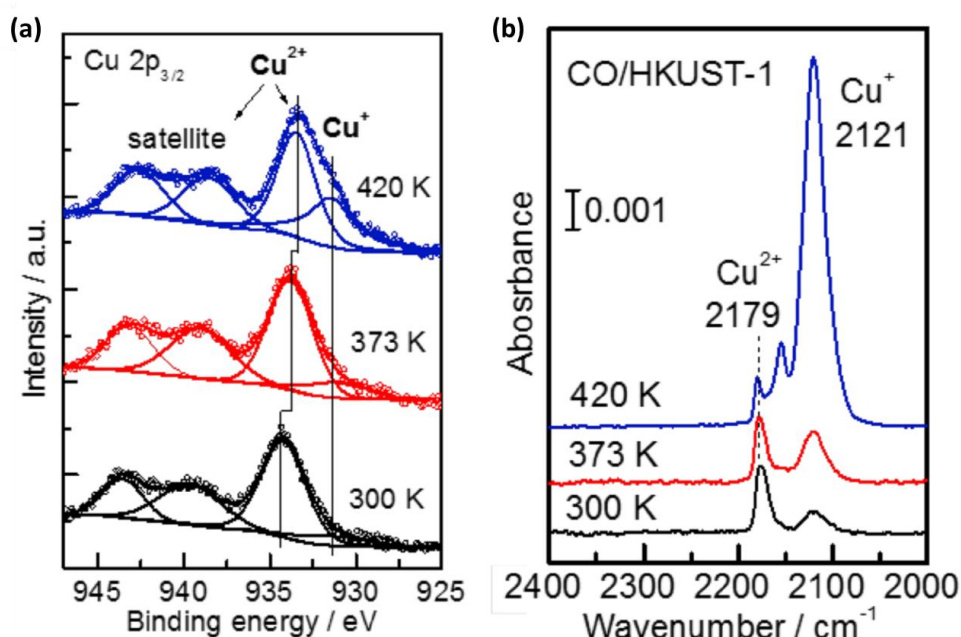


Figure 1.15 a) XPS of HKUST-1 SURMOF at different temperatures. b) UHV-IRRAS spectra of CO adsorbed on activated HKUST-1 SURMOF at 110 K. Aside from room temperature 300K (black), the sample was annealed at 373 (red) and 420 K (blue).[21]

Combining advanced IR spectroscopy and density functional theory a new reaction mechanism was proposed, where the key intermediate is an uncharged O₂ species, weakly bound to Cu⁺/Cu²⁺ (**Figure 1.16**). After exposing the pristine HKUST-1 SURMOF to O₂ at 55 K, the carboxylate-related vibrations at 1394/1656 cm⁻¹ ($\nu_{s(\text{OCO})}/\nu_{as(\text{OCO})}$) showed small red-shifts to 1386/1650 cm⁻¹ as a result of the dioxygen adsorption. A very weak signal at 1550 cm⁻¹ was also observed, slightly red-shifted with respect to the gas phase value (1556 cm⁻¹). The pristine Cu²⁺-related O₂ band at 1550 cm⁻¹ disappears at about 60 K, while the signal at 1546 cm⁻¹ disappears only after heating to 67 K. Based on DFT calculations, the latter one is assigned to activated, uncharged dioxygen species adsorbed to Cu²⁺ CUS of the reduced Cu⁺/Cu²⁺ dimers. The computed frequency (10 cm⁻¹ red-shift in comparison to O₂ on pristine paddle wheel) and binding energy (0.1 eV) are in good agreement with the experimental results that show the binding only occurs at low temperatures.

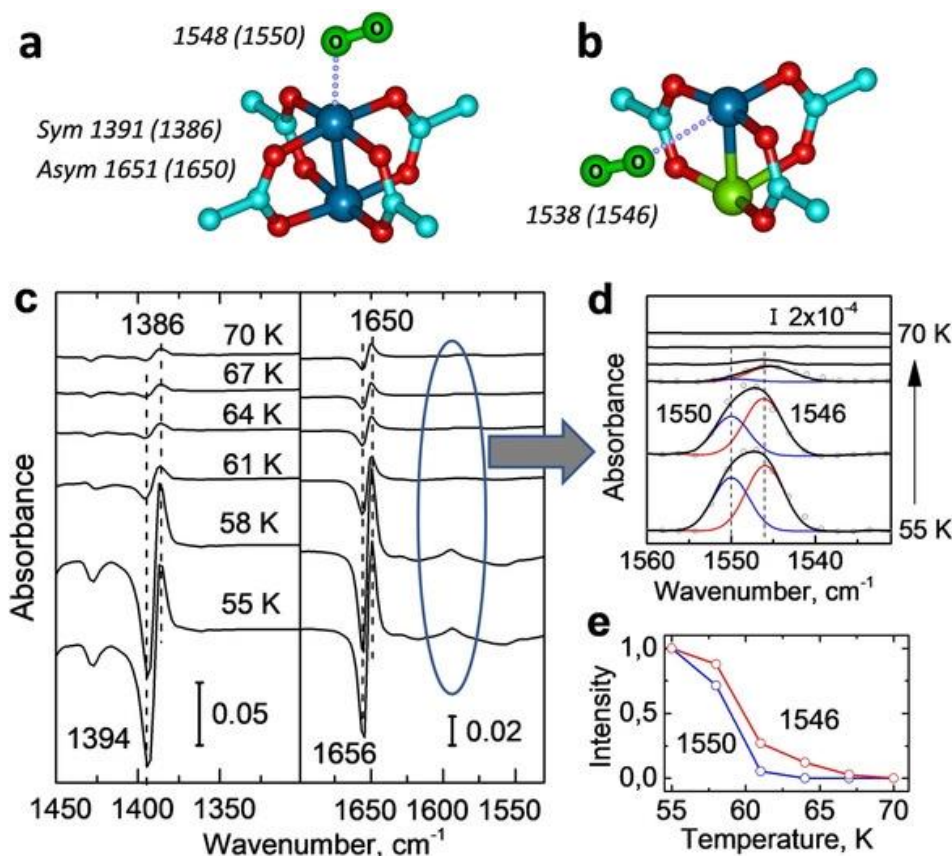


Figure 1.16 Interaction between dioxygen and HKUST-1 SURMOFs. DFT-optimized atomic structures of O₂ adsorbed to a) Cu²⁺/Cu²⁺ dimers of pristine HKUST-1 as well as b) to Cu⁺/Cu²⁺ defects of DE-HKUST-1, together with the computed O₂ and carboxylate stretch frequencies. For comparison, the corresponding experimental values are given in the parenthesis. c) IRRAS data in the region of carboxylate vibrations acquired after O₂ adsorption on DE-HKUST-1 SURMOF at 55 K and heating to indicated temperatures. d) Magnification of the O-O stretching region 1560–1530 cm⁻¹, the data were deconvoluted by fitting the individual components. e) Relative intensity evolution of the O-O vibration at 1550 and 1546 cm⁻¹ as a function of temperature. C of MOF-cyan, O of MOF-red, Cu²⁺-blue, Cu⁺-green, O of O₂-lime.[104]

1.2.4 Applications of SURMOF thin films

SURMOFs has gained attention for their potential applications in various fields, including electronics and energy.

1.2.4.1 Gas separation

One of the main applications of SURMOF thin films is in gas separation. Due to their high surface area and tunable pore size, SURMOFs have shown promise as selective and efficient membranes for the separation of gases such as hydrogen, carbon dioxide, and nitrogen. Compared to traditional separation methods driven thermodynamically such as distillation, a membrane-based process can substantially reduce the energy and capital cost of separating molecules on a large scale.[105] This makes them

attractive for use in applications such as hydrogen fuel cell technology and carbon capture and storage.

Using a photoswitchable SURMOF membrane, $\text{Cu}_2(\text{AzoBPDC})_2(\text{AzoBiPyB})$ (AzoBPDC: 2-phenyldiazenyl-4,40-biphenyldicarboxylic acid; AzoBiPyB: (E)-4,40-(2-(phenyldiazenyl)-1,4-phenylene dipyridine)), the permeate flux can be continuously adjusted (**Figure 1.17**).[106] The photoswitchable membrane was fabricated on an $\alpha\text{-Al}_2\text{O}_3$ substrate by LPE with a thickness of $\sim 2 \mu\text{m}$. The azobenzene moieties can be switched from the trans to the cis configuration and vice versa by irradiation with ultraviolet or visible light, resulting in a substantial modification of the membrane permeability and separation factor due to the precisely adjusted pore volume. By controlling irradiation times or by simultaneous irradiation with ultraviolet and visible light, the separation for H_2 : CO_2 can be adjusted between 3 and 8 (N_2 : $\text{CO}_2 = 5\text{--}8$).

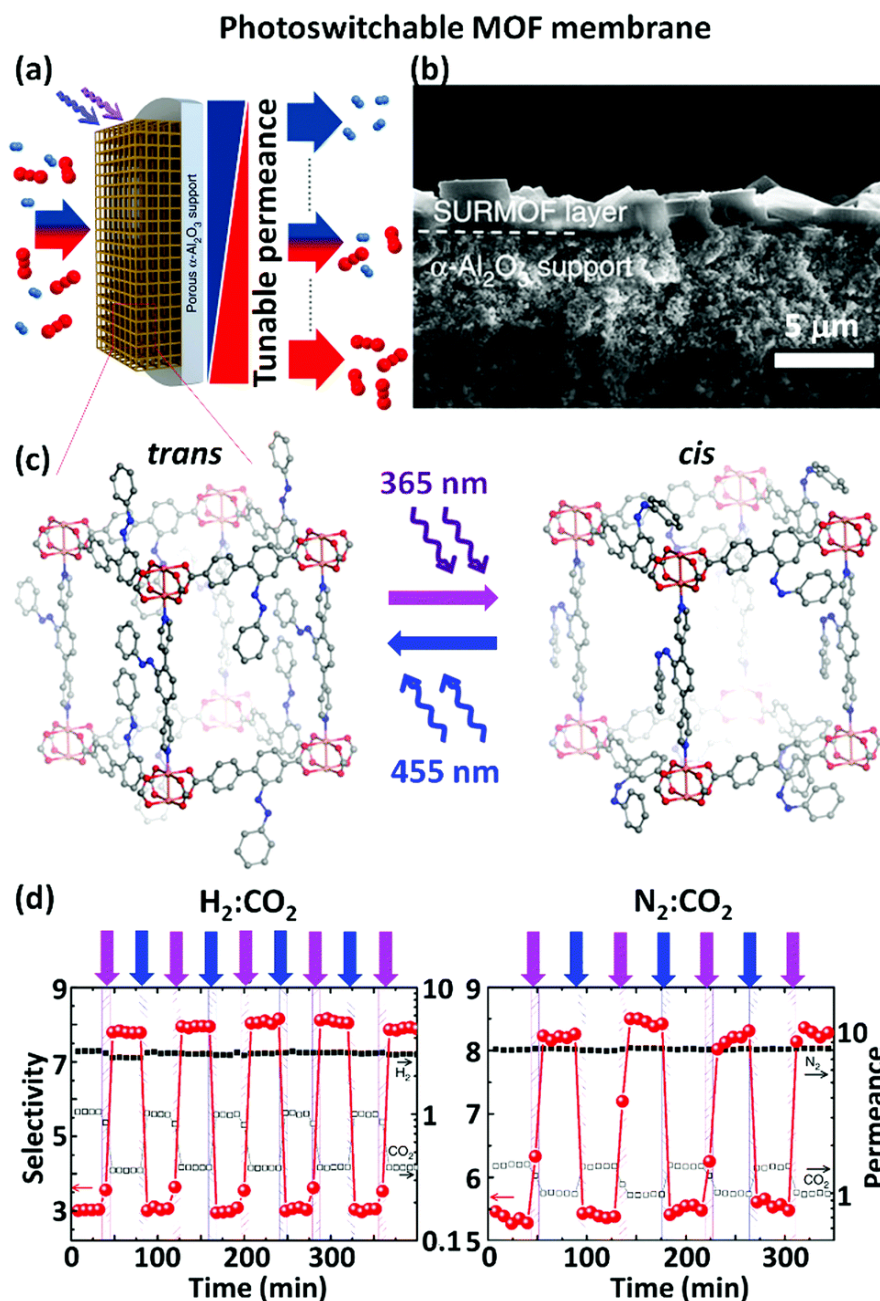


Figure 1.17 (a) Schematic illustration of tunable, remote-controllable molecular selectivity by a photoswitchable MOF membrane. (b) SEM cross-section image of the SURMOF membrane on the mesoporous $\alpha\text{-Al}_2\text{O}_3$. (c) The structure of $\text{Cu}_2(\text{AzoBPDC})_2(\text{AzoBiPyB})$ with the azobenzene groups. The transition between *trans* and *cis* states can be tuned by irradiation with 365 nm and 455 nm light, respectively. (d) The separation of $\text{H}_2:\text{CO}_2$ and $\text{N}_2:\text{CO}_2$ mixtures. The membrane is irradiated by 365 nm and 455 nm light for 5 min each. The permeances of H_2 and CO_2 (left), as well as N_2 and CO_2 (right), are shown in black with the unit of $\text{mol s}^{-1} \text{m}^{-2} \text{Pa}^{-1}$. The molecular selectivities (or separation factors) are shown in red. [106]

1.2.4.2 Electronic devices

The special properties of MOFs make them attractive candidates to also play passive roles in conventional electronic circuits. Also, it was demonstrated that MOFs can be

rendered with electric conductivity. Owing to the tunable structure of MOF, essential properties of electronic devices, such as electric conductivity[107], thermoelectric behavior[108], and magnetism[109], can be improved by designing new types of MOFs or post synthetic modifications. Since these applications require electrical contacts, the SURMOF deposited on conducting substrates (such as gold, Ag and Si) shows promising in the memristor[31], sensors[110], and organic field-effect transistors (OFETs).[33] In 2021, Bufon et al., report the first observation of room-temperature NDR in HKUST-1 SURMOF vertical heterojunctions (**Figure 1.18**).[111] The device structure relies on rolled-up metallic nanomembrane, which allows soft contacting the sub-15 nm thick HKUST-1 layer from the top. By precisely controlling the relative humidity (RH) around the device and the applied electric field, the NDR appears at low voltages (less than 2 V) with PVCR of about 2. The underlying physical mechanism is understood through band diagram analysis, density functional theory (DFT) calculations, and ab initio molecular dynamics simulations for quasi-saturated water conditions. The potential of the SURMOF-based NDR device is demonstrated by realizing a typical MVL application, a low-voltage ternary inverter. These results show that by effectively controlling the experimental conditions in a suitable manufacturing platform, SURMOFs allow the exploitation of exciting quantum electronic effects to realize novel devices.

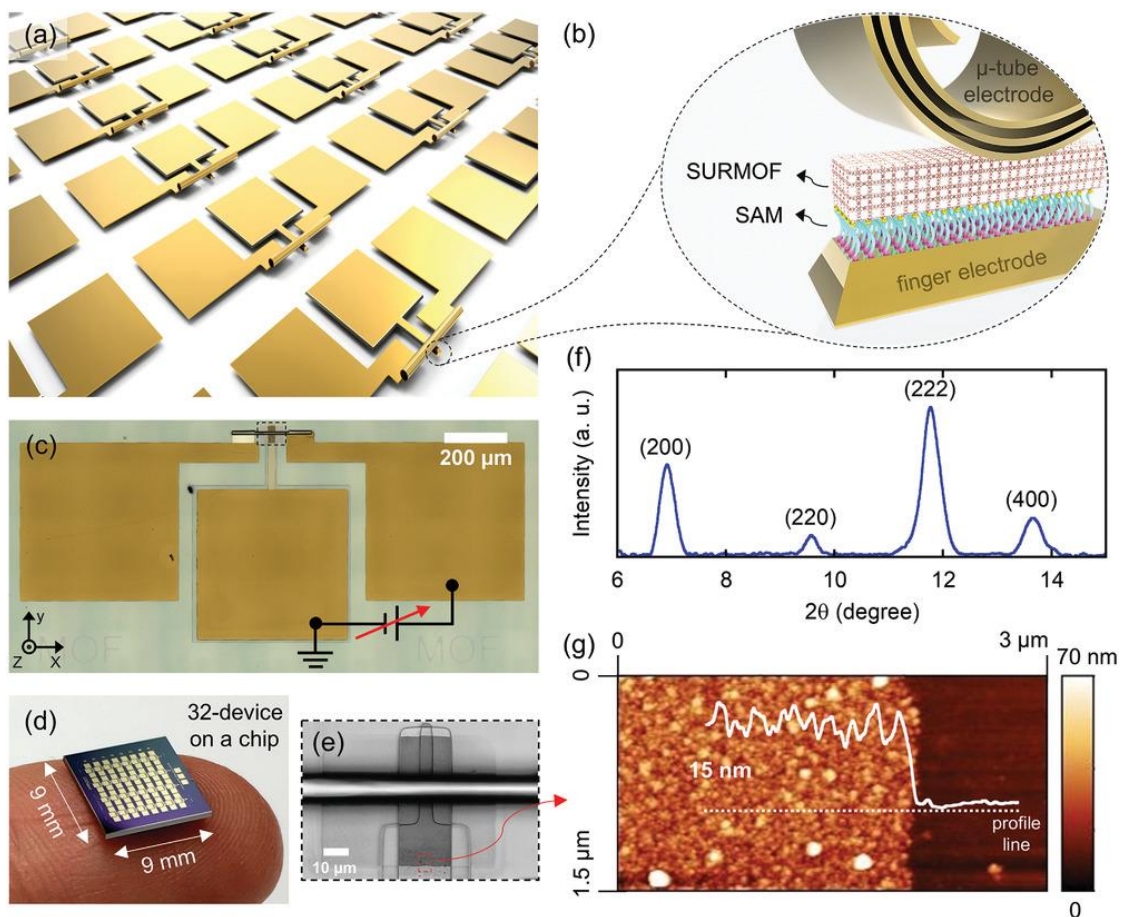


Figure 1.18 a,b) Illustration of an array of devices and the respective cross-sectional view (Au/SAM-HKUST-1/Au). c) LSCM image from a single device with the bias configuration for electrical measurements. d) Image of a microchip containing 32 devices. e) LSCM image from the dotted region in (c), showing the active device area in detail. f) GIXRD pattern for HKUST-1. g) AFM topography image from the dotted region in (e) and the respective profile thickness for HKUST-1.[111]

1.2.4.3 Energy storage

SURMOFs have been explored for use in energy storage applications, such as supercapacitors, due to their high surface area and porosity, which can contribute to high charge storage capacity. In batteries, the separator material can prevent lithium dendrimer formation and protect the electrodes from degradation. This requires a non-conductive porous solid with good physical properties. In this regard, SURMOF HKUST-1 as separators has been applied in Li-ion batteries, ILs@MOFs as (quasi) solid-state electrolytes (**Figure 1.19**).[112] There are different behaviors for samples using MOF powder pressed into pellets and SURMOF films. In the former, the conductance increases dramatically with loading, but this is attributed to excess IL in the pellets. In contrast, the conductance in MOF films can be purely attributed to the IL in the pores and shows a complex behavior. The conductivity of

$[\text{Li}_{0.2}\text{BMIM}_{0.8}][\text{TFSI}]$ in HKUST-1 only slightly decreases by less than one order of magnitude, with increasing pore loading.

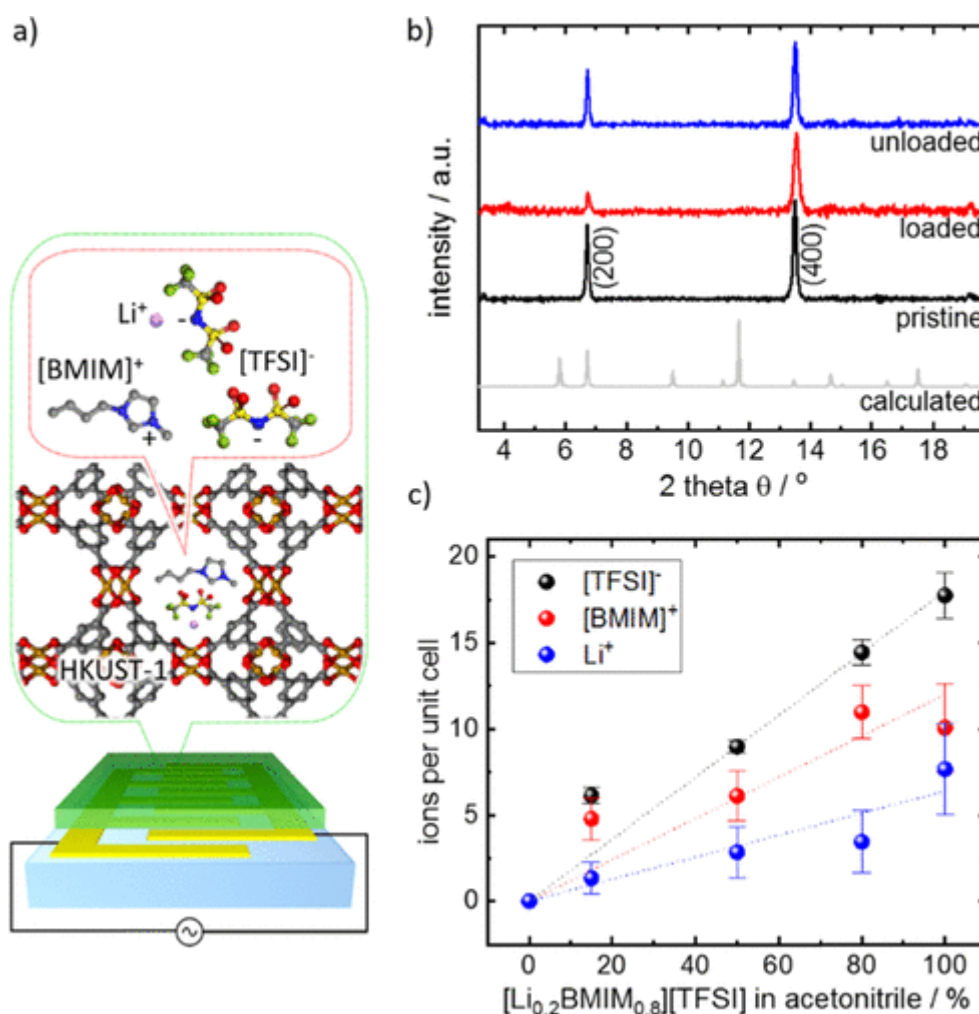


Figure 1.19 (a) Sketch of $[\text{Li}_{0.2}\text{BMIM}_{0.8}][\text{TFSI}]$ IL in the pores of the HKUST-1 MOF thin films. For measuring the conductivity of IL@MOF via EIS, the MOF films were grown on glass substrates with deposited interdigitated gold electrodes. The color code for the atoms is as follows: C gray, O red, Cu orange, N blue, F green, S yellow, and Li violet. H is not shown. (b) X-ray diffractograms of the pristine HKUST-1 SURMOF (black), the sample loaded with $[\text{Li}_{0.2}\text{BMIM}_{0.8}][\text{TFSI}]$ (red) and after unloading the sample by rinsing with ethanol (blue) compared with the calculated data for the corresponding powder structure (gray). The experimentally observed diffraction peaks are labelled. (c) Concentration of $[\text{BMIM}]^+$, $[\text{TFSI}]^-$, and Li^+ in the SURMOF loaded from different $[\text{Li}_{0.2}\text{BMIM}_{0.8}][\text{TFSI}]$ -acetonitrile solutions determined by energy-dispersive X-ray spectroscopy (EDX). The amounts of $[\text{TFSI}]^-$ and $[\text{BMIM}]^+$ relative to HKUST-1 are determined via fluorine, nitrogen, and copper. Based on the charge neutrality, the lithium amount is determined by the difference of $[\text{TFSI}]^-$ and $[\text{BMIM}]^+$. [112]

1.2.4.4 Optical application

By precisely controlling orientation, thickness, mass, crystallinity and roughness of the SURMOF, the production of large-scale optical devices is possible. lanthanoid elements. By using a layer-by-layer (LbL) approach, lanthanide-based SURMOFs

(Eu(III)BTC and Tb(III)BTC (BTC = 1,3,5-benzenetricarboxylate)) are fabricated for optical applications (**Figure 1.20**).[74] By stacking SURMOFs made from different Ln-ions, multilayer systems with predefined emission color could be fabricated just by changing the number of deposition cycles of the Eu(III)BTC top layer on the Tb(III)BTC bottom layers.

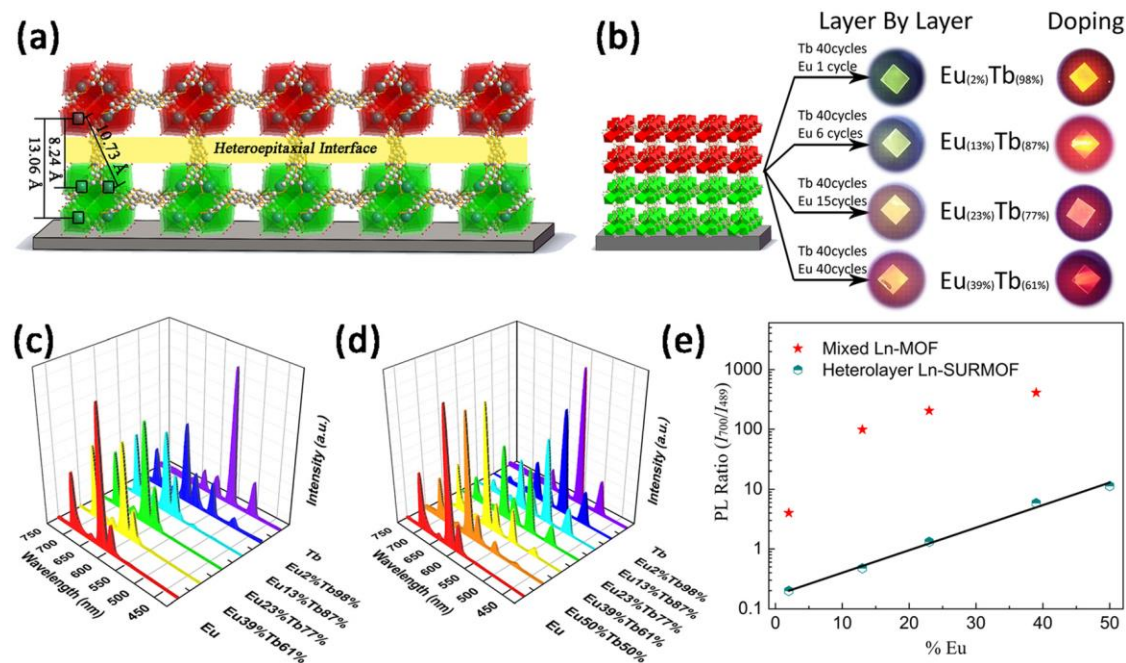


Figure 1.20 (a) Schematic illustration of the heteroepitaxial interface between Tb and Eu; (b) (left) structure of Eu/Tb-SURMOF on substrate and (right) photoluminescent color comparison between the SURMOFs fabricated by the LbL assembly approach and the doping method; (c) emission spectra of Ln-SURMOFs fabricated by doping Eu/Tb method; and (d) emission spectra of Ln-SURMOFs fabricated by the LbL assembly approach; (e) ratio between the intensity of the Eu(III) peak (700 nm) and the Tb(III) peak (489 nm) in mixed Ln-MOF and heterolayer Ln-SURMOF. Reproduced from Ref[74].

1.3 Chemical reactions within MOF and SURMOF

There are multiple application fields for the MOFs, such as gas separation, adsorption, water treatment, sensors, optics, and catalysis. Here we focus the utilization of MOFs in the chemical reactions, in which MOF works as a platform both as reactants itself or as catalysts.

1.3.1 As reactants

Ring-opening reactions provide a versatile route to irreversible binding of a range of function that are otherwise difficult to access in MOFs. An amine-containing metal–organic framework (MOF), IRMOF-3, has been irreversibly functionalized with sulfonate and alkylamine moieties through ring-opening reactions of 1,3-propanesultone and 2-methylaziridine (**Figure 1.21**).[113]

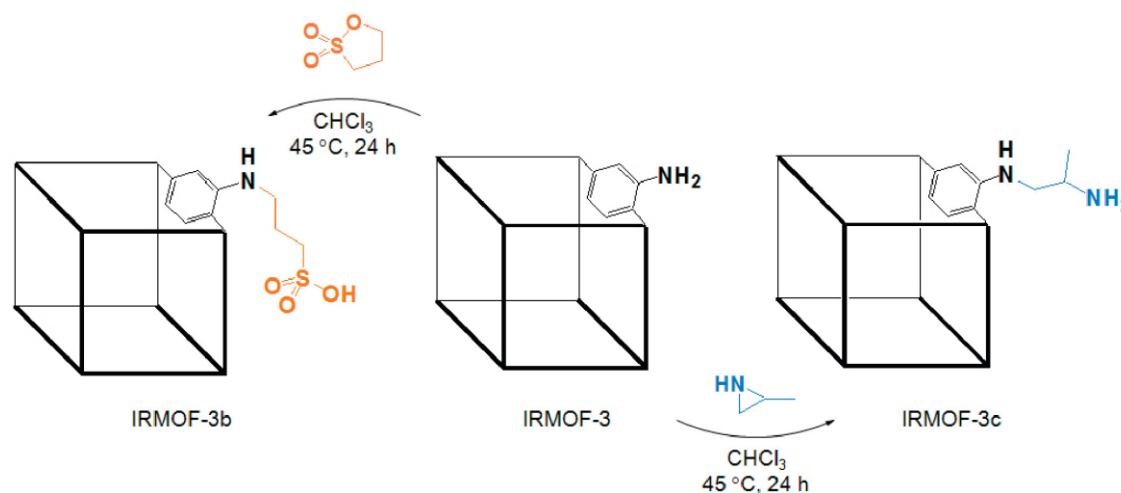


Figure 1.21 Ring-opening reactions performed on IRMOF-3 leading to covalently functionalized products IRMOF-3b and IRMOF-3c. The cage of the MOF is represented as a cube where vertices replace the metal clusters and edges replace the organic linkers.[113]

Post-synthetic modifications (PSM) on MOFs, in which chemical transformations or exchanges are made on pre-synthesized MOF materials, are found to be a powerful strategy for fabricating novel MOFs based on already existing MOFs. The term PSM was derived from the posttranslational modification of proteins.[114, 115] The chemical functionality is introduced by modification of an intact polypeptide. Taking this concept, PSM of MOFs may also serve to introduce chemical functionality that is not readily attainable from the constituent building blocks.

There is a difference between a solution and a MOF-based chemical reaction. A cubic MOF $Zn_4O(SDC)_3$ was treated with Br_2 . [116] Then the SDC ligands were converted to the dibromide adduct. Most importantly, the sole product of the MOF reaction with Br_2 was the meso-stereoisomer. This is in striking contrast to the homogenous reaction of the ligand with Br_2 in CH_2Cl_2 , which resulted in a 4[thin space (1/6-em)]:[thin space (1/6-em)]1 ratio of meso- to rac-isomers (**Figure 1.22**). Restricted bond rotation within the MOF leads to a single stereoisomer. Taking advantage of the matrix of a MOF, an unstable organic intermediate could be even isolated and structurally characterized.[117]

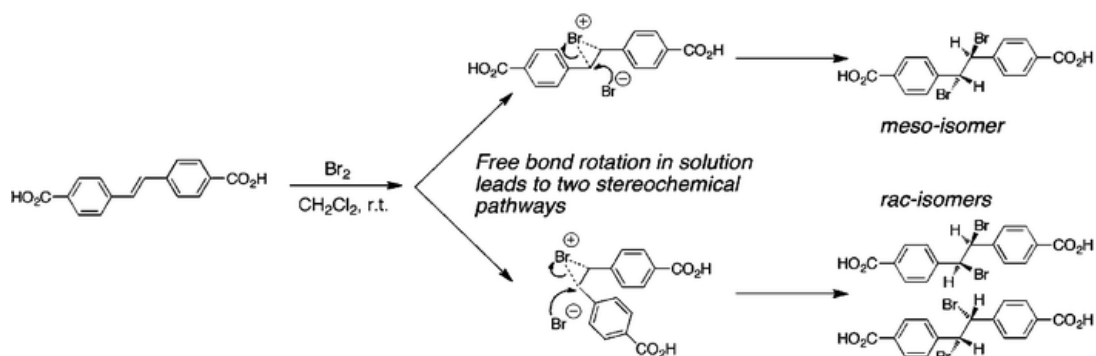
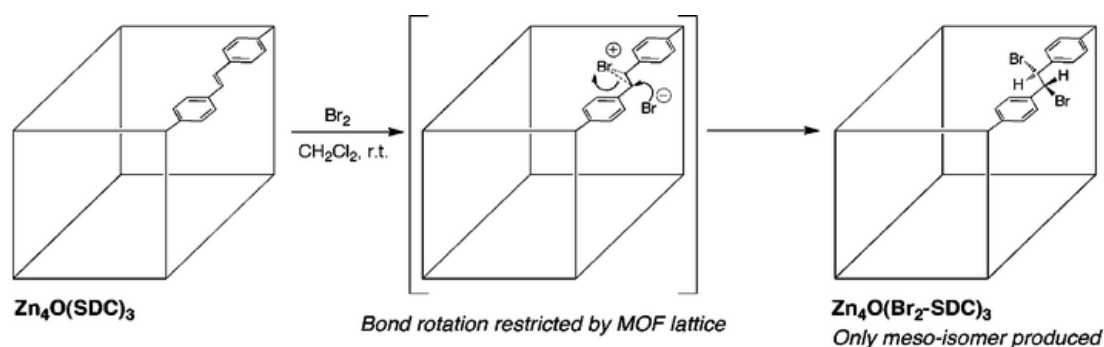


Figure 1.22 Bromination reactions within MOF (top) and in solution (bottom). [116]

By designing and construction of a PCP framework (CID-N₃; CID: coordination polymers with interdigitated structures) with a photoresponsive aryl azide molecule, a nanoporous compound with a photonicly switchable pore surface was achieved (**Figure 1.23**). The bare triplet nitrenes after photoactivation were accessible to and reacted with adsorbed oxygen or carbon monoxide molecules. It showed not only activation of the pore surface, but also a high probability of chemical trapping and conversion of guest molecules by light stimulation.[118]

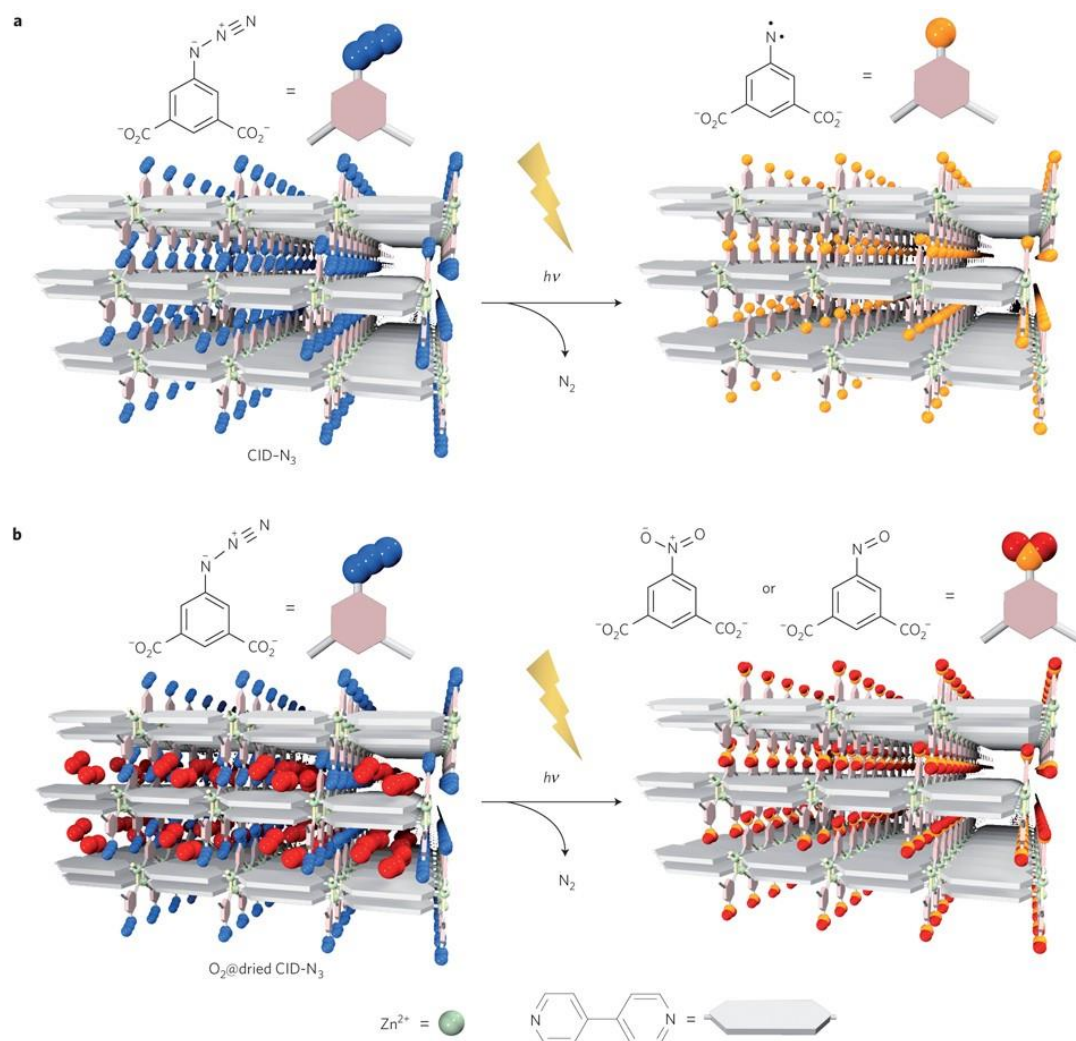


Figure 1.23 The framework of CID-N₃ is formed by interdigitations of two-dimensional sheets composed of Zn²⁺, 5-azidoisophthalate and 4,4'-bipyridine. Photoactivation of the azide moieties leads to the formation of triplet nitrenes on the pore surface (a) and photochemical trapping of physisorbed oxygen molecules in the framework of dried CID-N₃(O₂@dried CID-N₃) (b).[118]

Versatile of MOF structure bring opportunity to varies chemical reactions. The special structure of MOF, especially the coordination unsaturated sites, played an important role in these reactions. Through a so-called defect-engineering, where structural imperfections are created in a controlled fashion.[119] The chemical properties of MOF materials can be further modified by integration and decoration of linkers or loading with guest species, such as metal or metal-oxide nanoparticles or nanoclusters.

MOF provides a well-defined crystalline porous environment that can accommodate guest molecules, allowing spectroscopic studies of the system. Compared to solvent or polymer matrices, MOF provides a strictly periodic, very well-defined structural

framework in which the molecular environment of each embedded guest molecule is identical. In this respect, MOF is superior to an amorphous and inert matrix of gas, where the environment varies from sites to sites, resulting in uneven expansion of the spectral properties of the embedded guest, including the vibration band.[120]

1.3.2 As catalysts

Aside from the reactions where MOF itself acts as the reactants, catalytic reactions can also take place in MOF when it works as catalysts. Catalyst refers to a substance that increases the rate of a reaction without modifying the overall standard Gibbs energy change in the reaction; the process is called catalysis (IUPAC). The application in heterogeneous catalytic reactions is also not negligible for MOFs. As MOFs are a class of porous materials, they have gained significant attention in recent years due to unique properties, including high surface area, tunable pore size, and exceptional stability. Unlike their inorganic relatives (zeolite, aluminium phosphate), the structure of which is fixed, the MOF can be modified with the full toolbox organically synthesis, its pores can be decorated catalytic sites. These pores make it possible to control the transfer of reaction substrates and products by tuning the pores environment (size, topology, hydrophilic and hydrophobic etc.) The structural diversity and tunability of all MOF components (nodes, compounds and pores) enables the development of MOF-based catalysts by fixing different catalytic sites into a single MOF. For reaction mechanism, the well-defined structure also provides a good opportunity to understand the reaction at the molecular level.

A prominent example is Fujita's seminal 1994 report on Cd-4,4'-bipyridine coordination polymers that promote cyanosilylation of carbonyl compounds. This is one of the earliest proof-of-concept studies in the field of MOF catalysis.[121] Up to now, MOFs have been successfully applied in a variety of catalytic reactions (**Table 1.3**). MOFs have been successfully used in various types of catalytic reactions, including organic synthesis, electrocatalysis, and environmental remediation. For example, MOFs have been used as catalysts in the production of fuels and chemicals, as well as in the removal of toxic pollutants from wastewater. In addition, MOFs can also be used as precursors for the synthesis of other porous materials, such as zeolites, and can be modified to improve their catalytic performance. Besides, it bridges homogeneous catalysis and heterogeneous catalysis.[122] The born nature, insoluble

character, of MOFs heterogeneous catalysis makes it easy recycling. And, their open channels favor the transport and diffusion of substrates and products with minimized mass-transfer limit. Overall, MOFs have shown great potential in catalysis, and ongoing research continues to explore new applications and improve their performance.

Owing to the structural tailorability of MOFs, metal nodes, organic linkers and voids can work as catalytic active sites(**Figure 1.24**). Heterogeneous catalysis takes place on the interface between the catalysts and reactants, where normally the metal elements sites act as the active sites. Due to the metal centers, highly ordered porous structure, uniform pore sizes and environments, high surface areas of MOFs, they are superb templates for catalysts. Also, functional organic linkers can be grafted with the other metal sites. With the rich pores of MOF, nanoparticles or small clusters can be loaded inside as catalysts. The confinement environment of pores can limit the growth of these nanoparticles, which thus maintains the size of catalysts and catalytic stability. Tailoring the pore size, shape and spatial characters provide opportunities for the size-selective catalysis. More recently, the so-called defect-engineering, where structural imperfections are created in a controlled fashion, have shown unique physical and chemical properties in catalysis.[119]

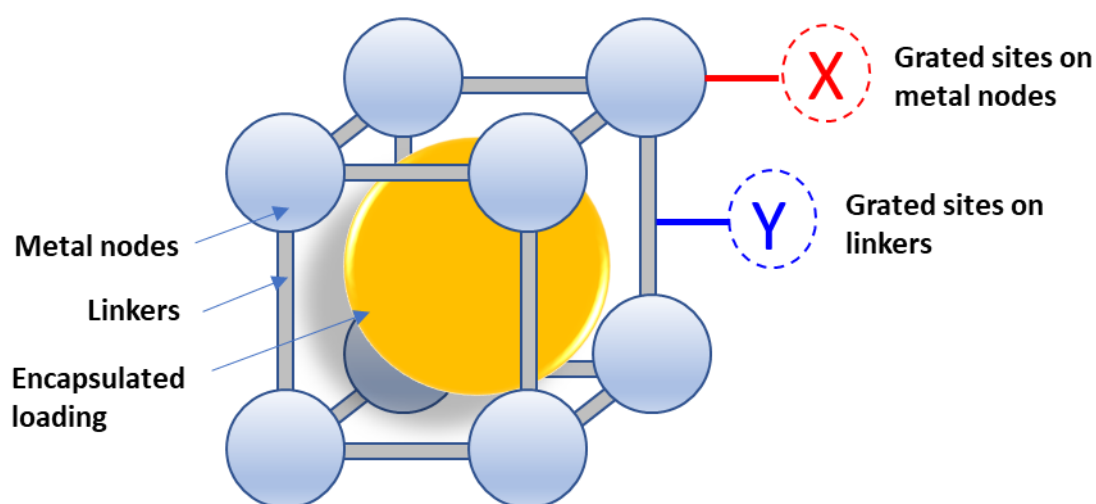


Figure 1.24. Catalytically active site origin in MOF-based materials.

Table 1.3 Representatives of MOFs applied in catalysis.

Reaction type	Reactions	Catalysts	Performance
Dehydrogenation reaction	$\text{NaBH}_4 + 2\text{H}_2\text{O} \rightarrow \text{NaBO}_2 + 4\text{H}_2$	CoNPs@ZIF-8	14 000 mLH ₂ min ⁻¹ g Co ⁻¹ and 19 400 mLH ₂ min ⁻¹ gCo ⁻¹ at 30 °C[123]
	$\text{HCOOH} \rightarrow \text{CO}_2 + \text{H}_2$	AuPd@MIL-101-NH ₂	100% H ₂ selectivity and an initial TOF 526 h ⁻¹ at 298 K[124]
	Hydrogenation of benzene	Ti-BDC MOF (MIL-125)	TOF value of 7017 h ⁻¹ with 0.005 mol % Ti ₈ -BDC-CoCl[125]
	Hydrogenation of 4-nitrophenol	Cu ₂ O@ZIF-8	Rate constant: 0.28 min ⁻¹ [126]
Hydrogenation reactions	Hydrogenation of α,β-unsaturated aldehydes to alcohols	MIL-101(Cr)@Pt@MIL-101(Fe)	45.0% conversion, 96.3% selectivity to unsaturated alcohol with TOF 76.3 h ⁻¹ [127]
	CO ₂ hydrogenation	CuZn@UiO-bpy	2.59 gMeOH kg Cu ⁻¹ h ⁻¹ , 100% selectivity to methanol, and stability over 100 h[128]
	Fischer–Tropsch synthesis	ZIF-67@SiO ₂	CTY 4.4 10 ⁻⁵ mol COG ⁻¹ Co s ⁻¹ , TOF 3.1 10 ⁻² s ⁻¹ [129]
	Transfer hydrogenation	Co-DABCO-TPA@C-800	Catalyzed the synthesis of more than 140 amines, reused 6 times without significant activity reduction[130]
Oxidation reactions	Hydrogenation of diphenyl sulfoxide	Ru/Zn-MOF	Conversion higher than 99%, 98% yield for diphenyl sulfide with a TOF value of 207.6 h ⁻¹ at 95 °C[131]
	Fluorene oxidation to fluorenone	Cu-CuFe ₂ O ₄ @HKUST-1	High activity (conversion: 99%) and selectivity of fluorenone formation (99%) at 60 °C[132]
	Oxidation of 2-aminobenzyl alcohol to 2-aminobenzaldehyde	Ru ₃ (CO) ₁₂ @ZIF-8	TOF of Ru ₃ /CN (4320 h ⁻¹) is about 23 times higher than that of small-sized (ca. 2.5 nm) Ru particles (TOF = 184 h ⁻¹)[133]
	CO oxidation	HKUST-1	-[104]
C-C coupling	$[\text{H}_2\text{S} + 1/2\text{O}_2 \rightarrow (1/n) \text{Sn} + \text{H}_2\text{O}]$	NH ₂ -MIL-53(Fe)	H ₂ S conversion, selectivity, and yield of S were all around 100% in the temperature range of 130~160 °C maintained 17h[134]
	Oxidative carbonylation of cyclohexanamine with CO	Au–Pd/MOF-253	TOF (2573 h ⁻¹) and selectivity (over 98%) were achieved after 20 h at 90 °C in THF (with the optimized Au:Pd molar ratio = 26:74)[135]
	A ³ coupling	AgNP@IRMOF-3	TOF 105 h ⁻¹ , recycled 8 times without decrease of activity[136]
C–H bond activation	Heck Coupling	Pd@MIL	44 h ⁻¹ [137]
	C–H bond halogenation	PCN-602(Mn) [Ni ₈ (OH) ₄ (H ₂ O) ₂ (TPPP-Mn) ₃]	Chlorination of cyclopentane up to 95% and the bromination of cyclohexane and cyclopentane up to 85 and 89%, respectively[138]
	Oxidation of ethane to ethanol by N ₂ O	Fe-MOF-74	-[139]
Biomass conversion	Transesterification of soybean oil to biodiesel	Fe ₃ O ₄ @HKUST-1-ABILs	Conversion to biodiesel reached 92.3% within 3 h, recycled 5 times[140]
	Self-Hydrogen transfer hydrogenolysis of β-O-4 linkages	Pd ₁ Ni ₄ /MIL-100(Fe)	High conversion (100%) and good yield (95%) were obtained under argon after 6 h at 130 °C[141]

Table 1.3 Continued.

Electrocatalysis	Hydrogen evolution reaction (HER) $2\text{H}^+ + 2\text{e}^- \rightarrow \text{H}_2$	Co-MOFs (CTGU-5 and -6)	Onset potential of 18 mV, low Tafel slope of 45 mV dec^{-1} , higher exchange current density of $8.6 \times 10^{-4} \text{ A cm}^{-2}$ [142]
		$\text{Cu}_3\text{P@NPPC}$	Onset potential of 89 mV, Tafel slope of 87 mV dec^{-1} , 3000 cycles and 11 h[143]
	Oxygen evolution reaction (OER) $2\text{H}_2\text{O} \rightarrow \text{O}_2 + 4\text{H}^+ + 4\text{e}^-$	PANI/ZIF-67	330mV, Tafel slope of 37 mV dec^{-1} [144]
	Oxygen reduction reaction (ORR) $\text{O}_2 + 4\text{H}^+ + 4\text{e}^- \rightarrow 2\text{H}_2\text{O}$	Ni-MOF@Fe-MOF	265mV, Tafel slope of 82 mV dec^{-1} [145]
		Fe-doped ZIF-8	Onset potential 0.90V, half-wave potential 0.77V[146]
Photocatalysis		Co/Zn-ZIF	94% CO Faradaic efficiency and a current of 18.1 mA cm^{-2} at an overpotential of 520 mV and activity with TOF = 18200 h^{-1} in 0.5 M KHCO_3 (pH = 7.2)[147]
	CO_2 reduction reaction (CO_2RR)	In-MIL-68	Faradaic efficiency for formic acid (96.5%) and a current density of 43.8 mA cm^{-2} [148]
		HKUST-1	Faradaic efficiency of 45% for C_2H_4 , and a current density of 262 mA cm^{-2} was achieved at -1.07 V (vs RHE).[149]
	Hydrogen Production Reaction	HM-TiPPh	H_2 production rate $945 \mu\text{mol h}^{-1} \text{ g}^{-1}$, sacrificial reductant TEOA, visible light, H_2O [150]
		Pt/MIL-125/Au	H_2 production rate $1743 \mu\text{mol h}^{-1} \text{ g}^{-1}$, sacrificial reductant TEOA, visible light, H_2O [151]
	CO_2 Photoreduction	Ni MOFs	CO H_2 $12.5 \mu\text{mol h}^{-1}$; $0.28 \mu\text{mol h}^{-1}$ 5 W LED lamp $\text{CH}_3\text{CN}/\text{H}_2\text{O} = 3:2$ [152]
	Photodegradation	TP-222(Zn)	RhB removals 100% in 270min under visible light[153]

SURMOF for photocatalysis

A hybrid-photocatalysts are prepared using a $\text{Bi}_2\text{O}_3\text{@HKUST-1}$ system by photodecomposition of BiPh_3 loaded into the pores of a metal–organic framework, yielding Bi_2O_3 -particles of a rather uniform size distribution, encapsulated into the pores of the MOF (**Figure 1.25**). The photocatalytic activity of $\text{Bi}_2\text{O}_3\text{@HKUST-1}$ was demonstrated using a standard test reaction, the degradation of a common dye, nuclear fast red (NFR). The hybrid $\text{Bi}_2\text{O}_3\text{@HKUST-1}$ SURMOF photocatalyst can be easily separated and recycled and it shows no significant loss in its photocatalytic activity.[32]

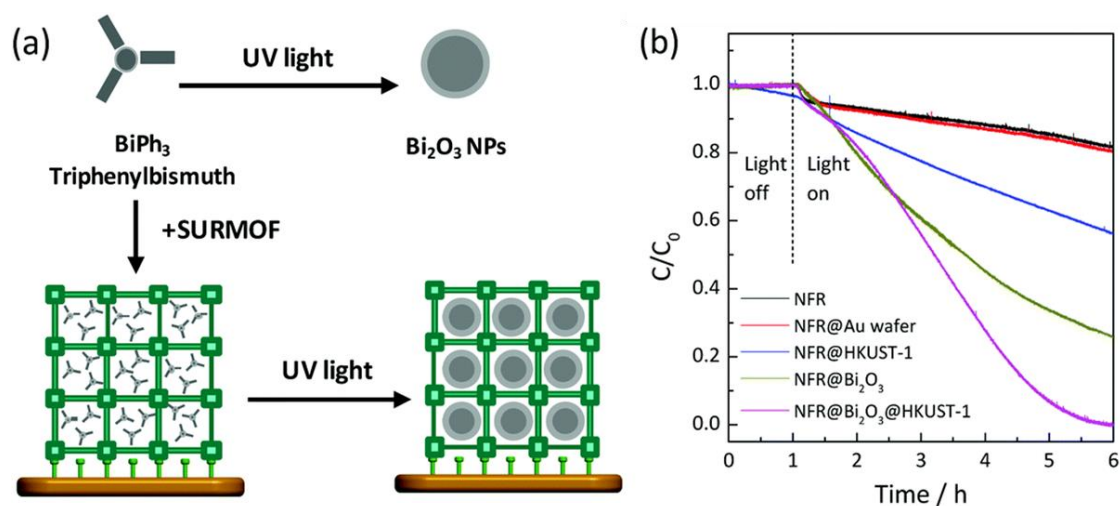


Figure 1.25 (a) Synthesis scheme of Bi₂O₃@HKUST-1 SURMOFs. (b) Photodegradation under different catalytic conditions [empty (black), Bi₂O₃@HKUST-1 SURMOF (red), HKUST-1 SURMOF (blue), powder Bi₂O₃ (dark yellow) and gold wafer (red)] under UV light irradiation. Reproduced from [32].

SURMOF for electrocatalysis

SURMOF thin film can also achieve a high Faraday efficiency of electrocatalytic conversion of CO₂ to CO. Via a spray coating method, SURMOF with metal salt (zinc acetate) and organic ligand (ReL(CO)₃Cl, L = 2,2'-bipyridine-5,5'-dicarboxylic acid) were deposited onto the FTO substrate.[66] The [001] oriented homogeneous Re-SURMOF with a sheet-like hierarchical structure was beneficial for the adsorption of CO₂ and provided a large electrocatalytically active surface area. The catalytic performance tests showed a higher Faraday efficiency (**Figure 1.26**) with a value of $93 \pm 5\%$ of CO production at -1.6 V vs. NHE.

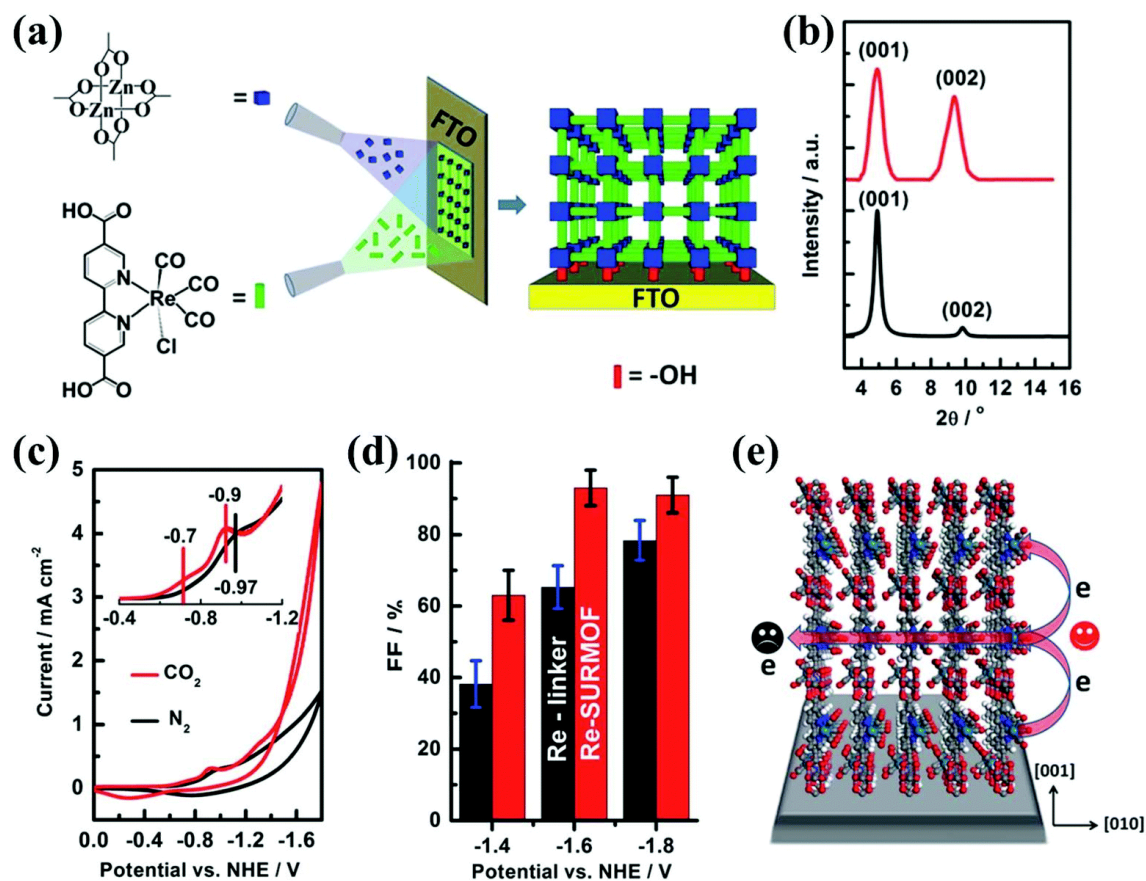


Figure 1.26 (a) The fabrication process of Re-SURMOFs on the functionalized FTO substrate in a LBL spray fashion; (b) the XRD data of Re-SURMOF; the CV (c) and faradaic efficiency (d) of Re-SURMOFs; (e) schematic representation of the preferred charge transfer pathway in epitaxial Re-SURMOFs fabricated on a FTO substrate along the [001] direction. Reproduced from [66].

A NiFe-BDC SURMOF (BDC=1,4-benzenedicarboxylic acid) was synthesized and transformed into a NiFe-based oxy-hydroxide thin film, which retains the BDC component (NiFe-BDC SURMOFD, denoted as 1-H), via a facile one-step alkaline treatment (**Figure 1.27**). Various functional groups such as -Br, -OCH₃, and -NH₂ were introduced to BDC in order to stimulate defect strain and to tailor the binding energies of the SURMOFDs for an enhanced OER activity. For the optimized NiFe-BDC(NH₂) SURMOFD (denoted as 1-NH₂) shows particularly high OER activity, with an anodic current density of 200 mA cm⁻² at an overpotential of just \approx 210 mV. Moreover, 1-NH₂ remains stable for more than 120 h at a current density of 500 mA cm⁻². The $\Delta E_{\text{ORR-OER}}$ was found to be \approx 0.69 V, outperforming the state-of-the-art catalysts.

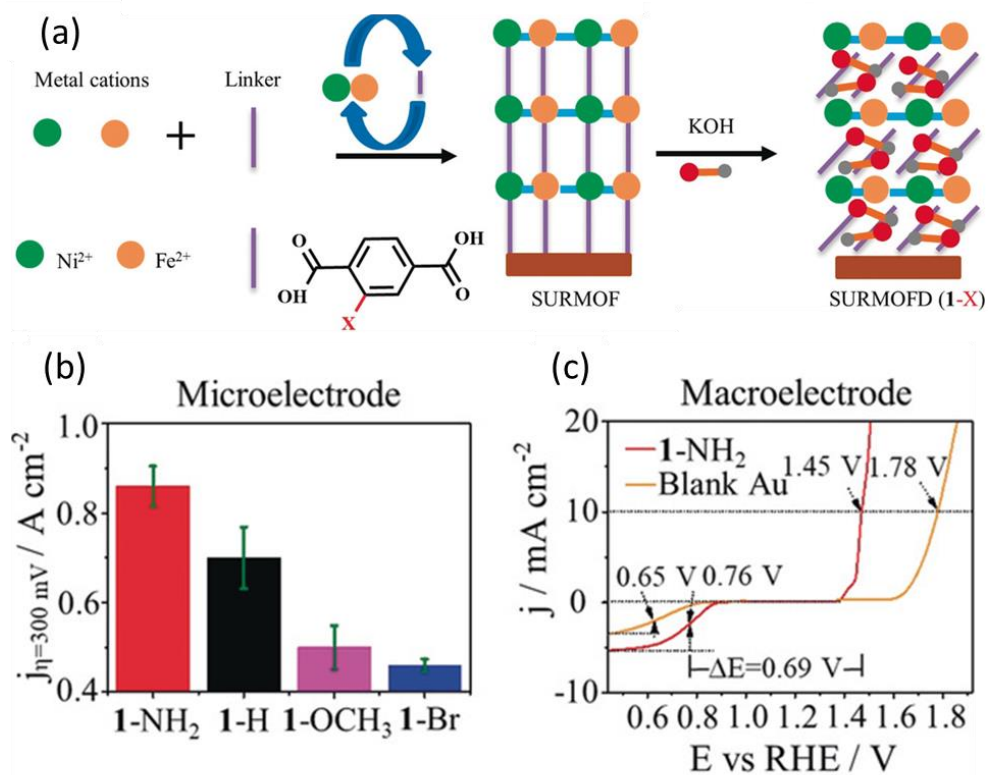


Figure 1.27 a) Preparation of NiFe-BDC (X) SURMOFs (X=NH₂, H, OCH₃ and Br) by layer-by-layer deposition and transformation of NiFe-BDC (X) SURMOFs to NiFe-BDC (X) SURMOFDs b) Comparison of the current density of 1-NH₂, 1-H, 1-OCH₃ and 1-Br for the OER at 1.53 V vs. RHE ($\eta=300$ mV); c) Anodic polarization curves from ORR to OER regime on 1-NH₂. Reproduced from [154].

2 Methods

2.1 Infrared spectroscopy

Infrared spectroscopy is one of the most powerful analytical techniques available for the characterization of catalytic systems, including single crystals and supported thin films as model catalysts, and catalysts powders (nanoparticles) and so on. A major breakthrough in IR spectroscopy was the introduction of Fourier-transform spectrometers. This type of instrument employs an interferometer and exploits the well-established mathematical process of Fourier-transformation. FTIR spectroscopy has dramatically improved the quality of IR spectra in terms of sensitivity and spectral resolution and minimized the time required to obtain data.

2.1.1 Theoretical background

Infrared spectroscopy is a technique where the vibrations and rotations of the atoms of a molecule are determined. These molecular excitations provide characteristic fundamental information on molecular species. The interaction of the radiation with molecules can be described in terms of a resonance condition where the specific oscillating radiation frequency matches the natural frequency of a particular transition of the bond or group in motion. In order for energy to be transferred from the IR photon to the molecule via absorption, the molecular vibration or rotation must cause a change in the dipole moment of the molecule. This is the general selection rule for IR spectroscopy, which requires a change in the electric dipole moment during the transition for the vibration to be IR active. **Figure 2.1** shows the oscillating electric field of the IR radiation generating forces on the molecular dipole. The oscillating electric field drives the oscillation of the molecular dipole moment, alternately increasing and decreasing the dipole spacing.

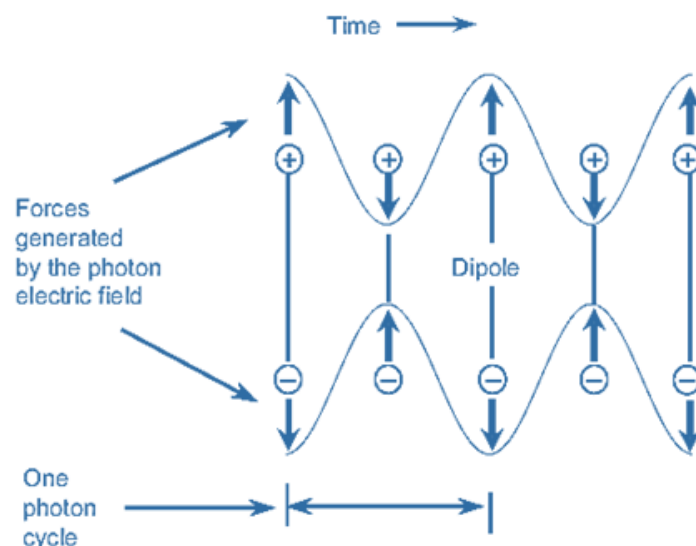


Figure 2.1 The oscillating electric field of the photon generates oscillating, oppositely directed forces on the positive and negative charges of the molecular dipole. The dipole spacing oscillates with the same frequency as the incident photon.[155]

The dynamic dipole moment of uncharged molecules originates from the partial charges of the atoms, which can be determined by molecular orbital calculations. Symmetric molecules or bonds do not have a dipole moment and therefore do not absorb infrared radiation. For example, N_2 has no dipole moments and thus IR inactive. In contrast, heteronuclear diatomic molecules such as HCl, NO, and CO have dipole moments. So, their corresponding vibrations are IR active. For complex molecules, they often contain more chemical bonds and correspondingly show more complex vibrational spectra, in which IR active and IR inactive both exists. The normal vibrations of molecules containing N atoms are described by the internal degrees of freedom resulting in the well-known $3N-6$ and $3N-5$ rule-of-thumb for non-linear and linear molecules, respectively. The fundamental vibrations for the water (non-linear, $3 \times 3 - 6 = 3$) and carbon dioxide (linear, $3 \times 3 - 5 = 4$) molecules, which involve two types of normal vibrations: stretching modes (changing band lengths) and bending modes (changing band angles). However, the CO_2 symmetrical stretching is IR inactive because it has no dipole moment (**Figure 2.2**).

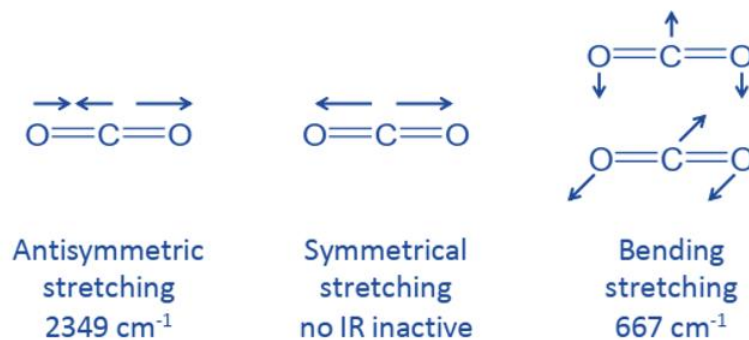


Figure 2.2 The vibrational modes in the linear molecule CO_2 .

2.1.2 Infrared reflection-absorption spectroscopy (IRRAS)

Depending on the type of the sample, infrared spectra can be obtained using either reflection or transmission geometries, e.g. for single crystals or powder particles, respectively. To characterize thin films or monolayers on substrate surfaces, infrared reflection-absorption spectroscopy has been widely applied. An incident IR beam irradiates the sample layer, and is reflected toward the detector by the underneath metallic layer as metal substrates present a good IR reflectivity. Part of the spectrum is then absorbed by the sample layer while passing through it. The incident light can be divided into two parts, the part of the electric field that is parallel to the plane of incident (E_p) and the part that is perpendicular to the plane of incident (E_s , german: senkrecht), see **Figure 2.3** left.

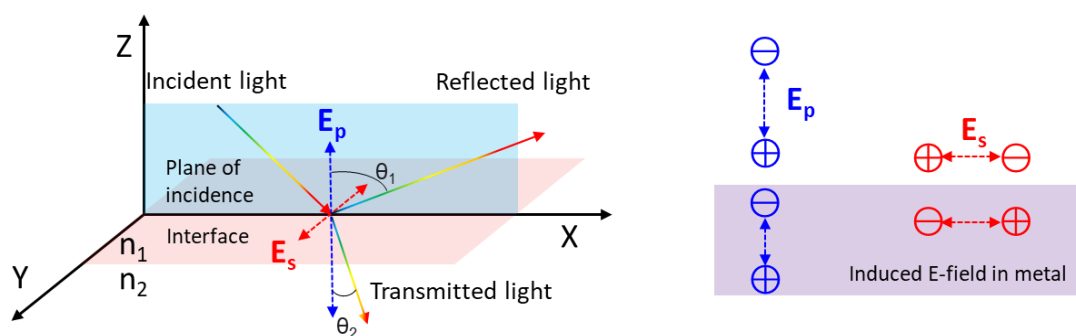


Figure 2.3 Left: Schematic representation of an incident light beam reflected at the interface of two optically different materials ($n_1 \neq n_2$). Right: Schematic explanation of the surface selection rule, the induced red dipole moment is enhanced while the blue ones cancel out each other.

Depending on the angle of incidence (θ_1), polarization, and the small amount of energy of the light, different substrate materials, such as gold, silver, silicon, or glass, exhibit different reflectivities for adsorbate-coated substrates. The reflectance difference between the adsorbate-coated substrates and the blank substrates may even

be negative, leading to negative absorption bands in the spectra. In general, materials respond differently to portions of light that are parallel to the plane of incidence compared to portions perpendicular to that plane. For unpolarized light, the intensity of the vibrational bands may be small if the wrong angle of incidence or substrate material is chosen. A material that exhibits high reflectivity and no part of the perpendicular light is gold. Gold exhibits a maximum reflectance of about 87°, about 50 times greater than the maximum reflectance of silicon (**Figure 2.4**).

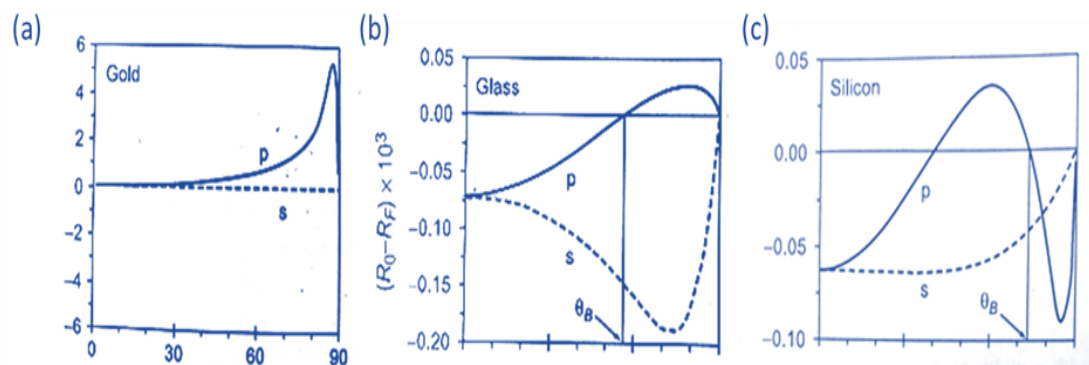


Figure 2.4 Calculated reflectivity differences between the clean substrate (R_0) and adsorbate-covered substrate (R_F) for different substrate materials.[156]

The basic layout of IRRAS is shown in **Figure 2.5**. The path of the infrared beam is shown by the thick yellow line. There are four main components, namely, infrared ray source (laser diode), interferometer, sample holder and detector. The IRRAS of the samples in this study were acquired with a resolution of 2 cm^{-1} using a FTIR spectrometer (Bruker VERTEX 80v). All the IRRAS results were recorded in grazing incidence reflection mode at an angle of incidence amounting to 80° relative to the surface normal using liquid nitrogen cooled mercury cadmium telluride narrow band detectors. Perdeuterated hexadecanethiol self-assembled monolayers (SAMs) on Au/Si were used for reference measurements.

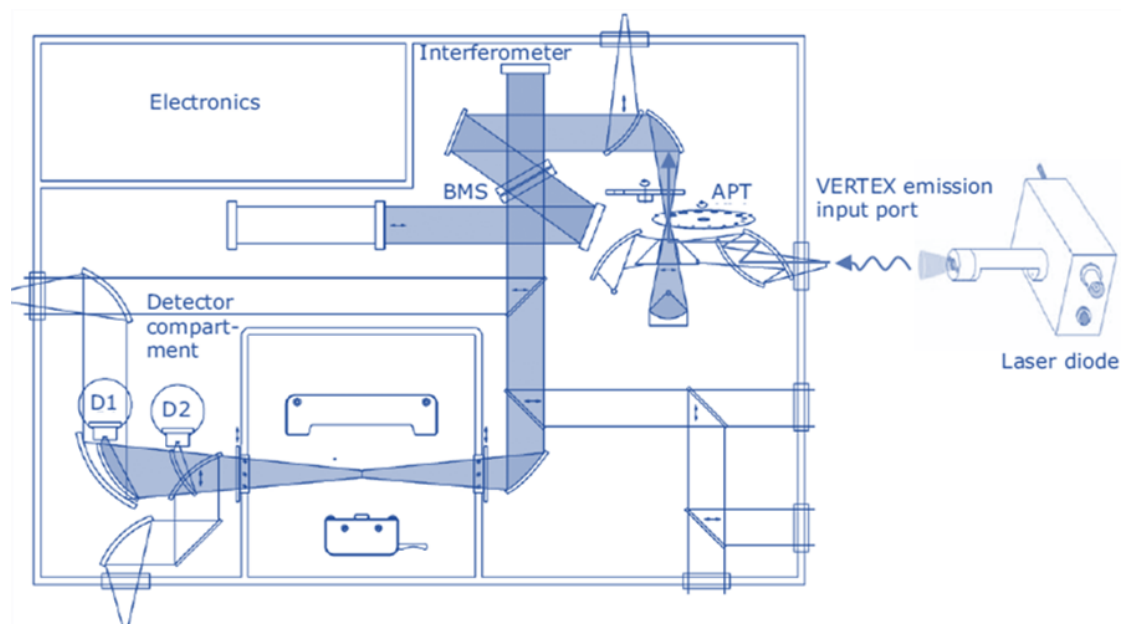


Figure 2.5 Schematic of an IRRAS instrument.

2.2 RAMAN spectroscopy

Raman spectroscopy is the complementary vibrational spectrum of infrared. It performs chemical analysis of samples using light to generate (excite) molecular vibrations and then interpret this interaction. It is based on the inelastic scattering of light that occurs when a substance is illuminated with light. After this light interacts with the sample, a very small fraction of it changes wavelength. This change is called the Raman effect. Collecting this light produces information about the sample.

The Raman effect is the inelastic scattering of photons off matter, meaning that there is both an exchange of energy and a change in the direction of light. Typically, this effect involves molecules gaining vibrational energy when incident photons are shifted from visible laser light to lower energies. This is called standard Stokes Raman scattering (**Figure 2.6**). When photons (light) "impact" matter, most of the scattered light remains unchanged in its wavelength. Aiming a green laser pointer at a wall, you will always see a green dot. The scattered light is obviously the same color, and this phenomenon is called Rayleigh scattering.

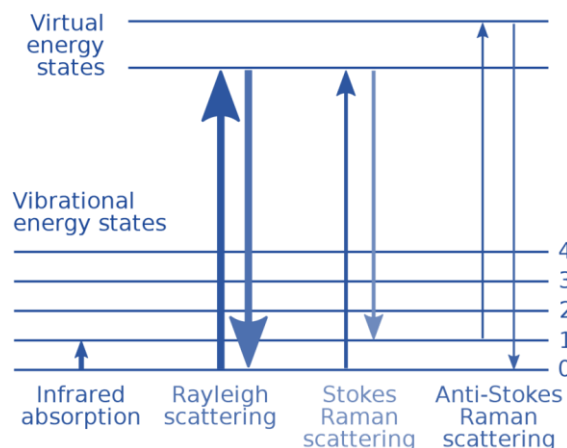


Figure 2.6 Energy-level diagram of scattering.

Raman spectroscopy really took off with the discovery of the laser, as the use of monochromatic light played a major role. To do this, the sample is irradiated with a laser (**Figure 2.7**) and part of the scattered light is analyzed with a spectrometer (dispersive or FT technique). Finally, Raman spectroscopy reveals characteristic signals, or "bands," of the material under study. Raman measurements in this thesis were recorded with a FT-Raman Spectrometer "MultiRam" (Bruker Optics, NdYAG Laser $\lambda = 1064 \text{ nm}$, $P_{\text{max}} = 1 \text{ W}$). The position of the Raman bands is given in wavenumbers [cm^{-1}].

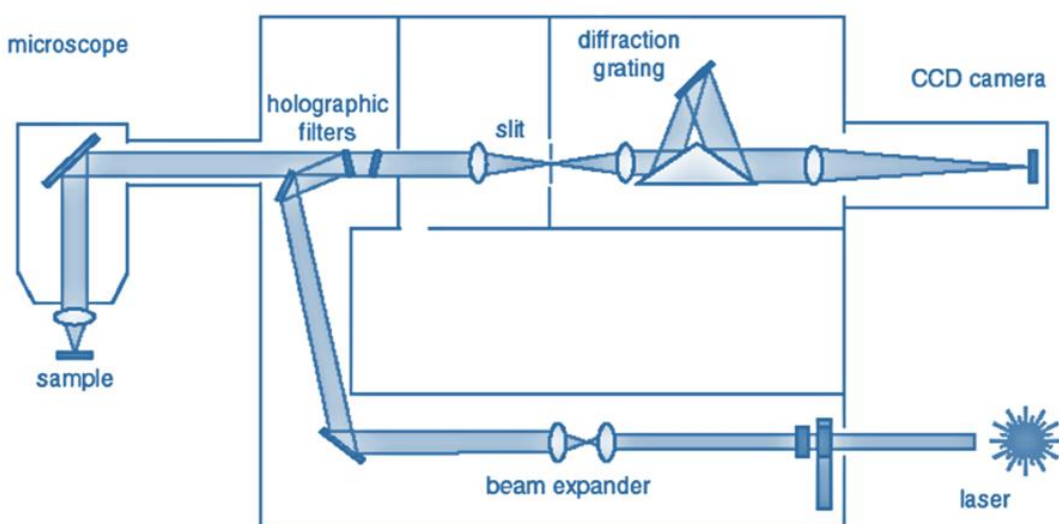


Figure 2.7 Schematic of the Raman instrument.

2.3 X-ray diffraction

X-ray diffraction (XRD) techniques give information about the structure of solids in a non-destructive way. Qualitatively, it provides the kinds of materials that compose a solid; quantitatively, it shows the quantity of materials that compose the solid.

2.3.1 Theoretical background

XRD originates from the constructive interference of monochromatic X-rays within a crystalline sample. It is based on Bragg's law: the diffracted X-rays exhibit constructive interference and diffraction patterns are visible when the path difference between the X-rays diffracted on the parallel and adjacent lattice planes is a multiple of the X-ray wavelength (**Figure 2.8**). This is given by the equation:

$$n \lambda = 2d \sin \theta$$

n : the diffraction order ($n=1$ for first order, $n=2$ for the second order)

λ : the wavelength

θ : the glancing angle (optics)

d : the grating constant of the crystal being connected

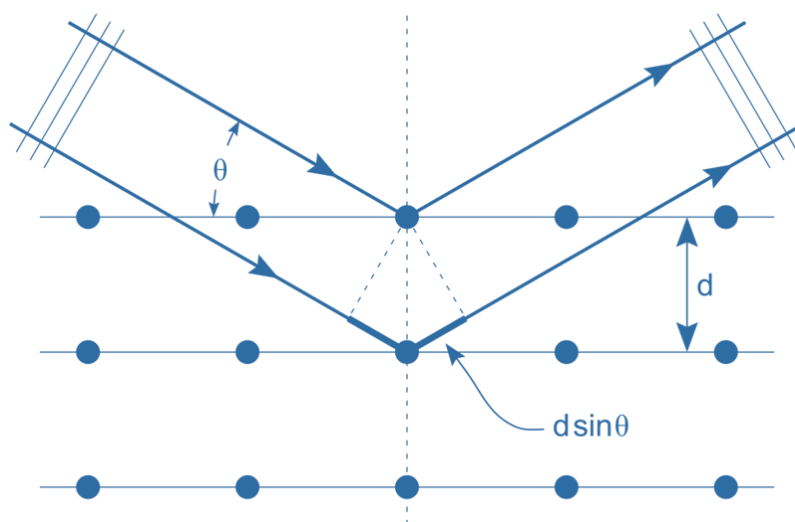


Figure 2.8 Schematic illustration of Bragg diffraction.

A crystalline material possesses an ordered and periodic arrangement of elements. The distances between the nearest neighboring atoms or ions are typically a few angstroms and are comparable with the magnitude of X-ray wavelengths. Therefore, when the monochromatic X-rays hit into the crystalline sample, the interaction of the

incident X-rays with the crystalline sample will exhibit constructive interference in some scattering direction.

2.3.2 X-ray diffraction of the MOF thin film: in plane and out of plane

Unlike powdery samples which have a random orientation distribution of crystals, the thin film samples like SURMOFs mainly possess one orientation to the supporting surface normal. To determine the crystalline structure and orientation of such thin films, the combination of in-plane and out-of-plane XRD techniques is needed. As shown in **Figure 2.9**, these two techniques provide orientation information in the directions perpendicular and parallel, respectively, to the sample surface.

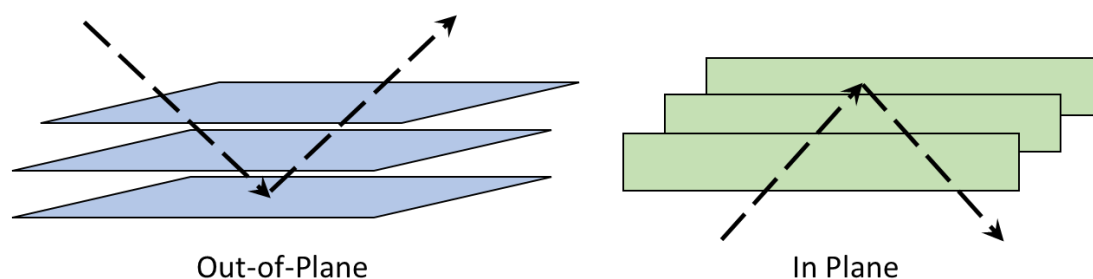


Figure 2.9 Geometries showing the out-of-plane and in-plane XRD measurements.

The out-of-plane diffraction technique records the X-rays scattered from the lattice planes parallel to the surface, and provides the crystallographic information along the direction perpendicular to the surface. This means only the crystallographic information along one direction of the crystal are obtained. In contrast, the in-plane diffraction technique monitor the X-rays scattered from the lattice planes perpendicular to the surface, and can provide the information for any direction tangential to the surface, though the geometry displays only one example of lattice plane orientation.

Generally, an X-ray diffractometer consists of three essential components: an X-ray source, an X-ray detector and a goniometer. For the characterization of SURMOFs in this thesis, the out-of-plane remeasurements were carried out using a Bruker D8-Advance diffractometer in θ - θ geometry equipped with a PSD Lynxeye®. The in-plane XRD measurements were carried out using Bruker D8 Discover equipped with a quarter Eulerian cradle, tilt-stage and 2.3° Soler-slits installed in both sides. A Göbel-mirror, and a PSD Lynxeye® in θ - 2θ geometry were applied. For both

machines, Cu-anodes(Cu $K\alpha_{1,2}$ -radiation with $\lambda = 0.15418$ nm) were used. The out-of-plane and in-plane measurement were usually carried out in the range of $2\theta = 4^\circ - 20^\circ$ at a scan step of 0.02° at 40kV and 40 mA with various counting times in this PhD study.

2.4 AFM

Atomic force microscopy (AFM) images the morphology of a sample surface with a three-dimensional (3D) detail. The resolution can be down to the nanometer scale. In this thesis, the AFM image was obtained by using an Asylum Research Atomic Force Microscope, MFP-3D BIO. The substrates were measured in air as received. The AFM was operated at 25°C in an isolated chamber in alternating current mode (AC mode). AFM cantilevers were purchased from Nano&more. NSC-18 AFM-HQ cantilevers with the following properties were used: nominal resonance frequency: 75 kHz; nominal spring constant: 3.5 N/m.

2.5 SEM

Scanning electron microscopy (SEM) is a powerful technique in the examination of materials and it is used widely in detecting the information about the surface morphology and to some extent, the composition of the sample. In this thesis, the morphology measurements are carried out in a FEI Philips XL 30 Field Emission Gun Environmental Scanning Electron Microscope (FEG-ESEM). To avoid charging, insulating materials have to be coated with a thin Gold/Palladium film. Then the specimen can be imaged under high vacuum conditions (10^{-5} Pa) using acceleration voltages between 5 and 20 kV.

2.6 Mass spectroscopy

Mass spectroscopy (MS) is a soft ionization technique that is typically used to determine the molecular weights of solid or liquid samples. This technique allows the sample to be nonvolatile or thermally unstable. This characteristic indicates that ionization of samples, such as organic and inorganic molecules, can be performed, but a molecule with a fairly large mass (normally over 100) is required. The other major disadvantage is that the sample should be well dispersed in a solution. The MS experiments are conducted by detecting the ratios of mass to charge of various peaks

in the spectrum. Initially, the ions in solution are ionized into small droplets. Subsequently, these droplets will be further desolvated into even smaller droplets to create molecules with attached protons. Finally, these ionized and desolvated molecular ions will be passed through the mass analyzer to the detector, and the mass of the sample can be determined. In this thesis, ESI-MS was acquired with a Bruker micro OTOF-Q II spectrometry. The scan range was m/z 50–1500 under dry gas-nitrogen at 120 °C.

2.7 Electrocatalytic OER

OER performances were tested on an electrochemical workstation (Ivium-n-Stat, Ivium Technologies) with a standard three-electrode electrochemical cell. A saturated Ag/AgCl was selected as the reference electrode and a platinum plate as the counter electrode. The working electrode is the SURMOF thin film sample with surface area of 1 cm^2 . All LSV curves were measured in the 1 M KOH aqueous solution with a scan rate of 5 mV s^{-1} .

2.8 UHV apparatus

2.8.1 THEO

THEO, manufactured by Prevac (Rogów, Poland), is a development of the UHV-IR apparatus designed at the Karlsruhe Institute of Technology, which is dedicated to the spectroscopic characterization of oxides, single crystals, MOFs as well as powders. The innovative design allows combining several surface-sensitive techniques in one apparatus. It is unprecedented that a UHV chamber can be inserted into the sample compartment of a conventional FTIR spectrometer (Bruker VERTEX 80v) to form a compact connection and thereby avoid the loss of beam intensity as little as possible. The construction of the new UHV-IR in Karlsruhe was benefit from Bochum's experience. Compared to Bochum machine, THEO has been equipped with a cryostat at the IR chamber enabling the sample to be cooled down to 60 K with liquid helium. Additionally, the spectrometer is equipped with a polarizer which makes it possible to measure with s- and p-polarized light. The metal oxide surfaces thus can be better examined in particular, as on these surfaces the surface selection rule, unlike metals, does not apply.

The UHV apparatus THEO (**Figure 2.10**) consists of two big UFO-shaped distribution chambers, which are connected together by a reorientation chamber, and multifunctional chambers, such as load-lock, preparation, infrared, magazine and analysis chamber, are also attached. Here we can carry out additional characterizations by using combined measurement techniques including LEED, XPS, ultraviolet photoelectron spectroscopy (UPS), Auger electron spectroscopy (AES), and thermal desorption spectroscopy (TDS).

The load-lock chamber is pumped by a turbomolecular pump (Leybold, TMP 150 and a rotary pump (TRIVAC), yielding a base vacuum of better than $1 \cdot 10^{-8}$ mbar after bakeout. This chamber is used to transfer samples from atmosphere into the UHV system without affecting the vacuum in the distribution or measurement chamber. The samples are first mounted on a sample holder and then inserted to the load-lock mechanism by using a special, dedicated gripper. The distribution chamber is evacuated by an ion getter pump (Gamma Vacuum 300 l/s) and a titanium sublimation pump, the base pressure amounts to $1 \cdot 10^{-10}$ mbar. Transferring the sample to the different UHV chambers attached to the distribution chamber is accomplished via a dedicated transfer mechanism, which comprises a rotary feed through allowing for a fast and reliable transport of sample holder between the different UHV chambers, each of them separated from the distribution chamber by a gate valve.

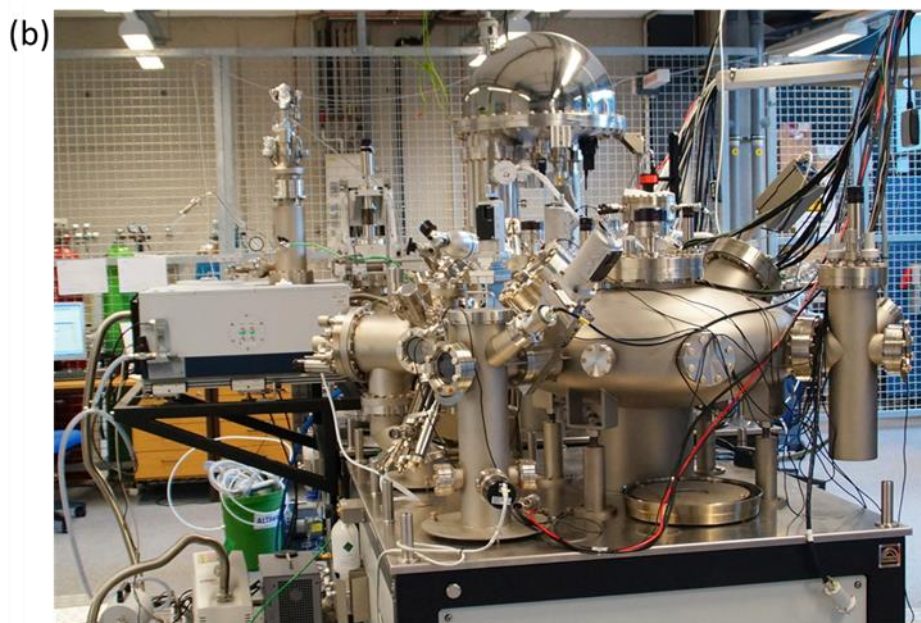
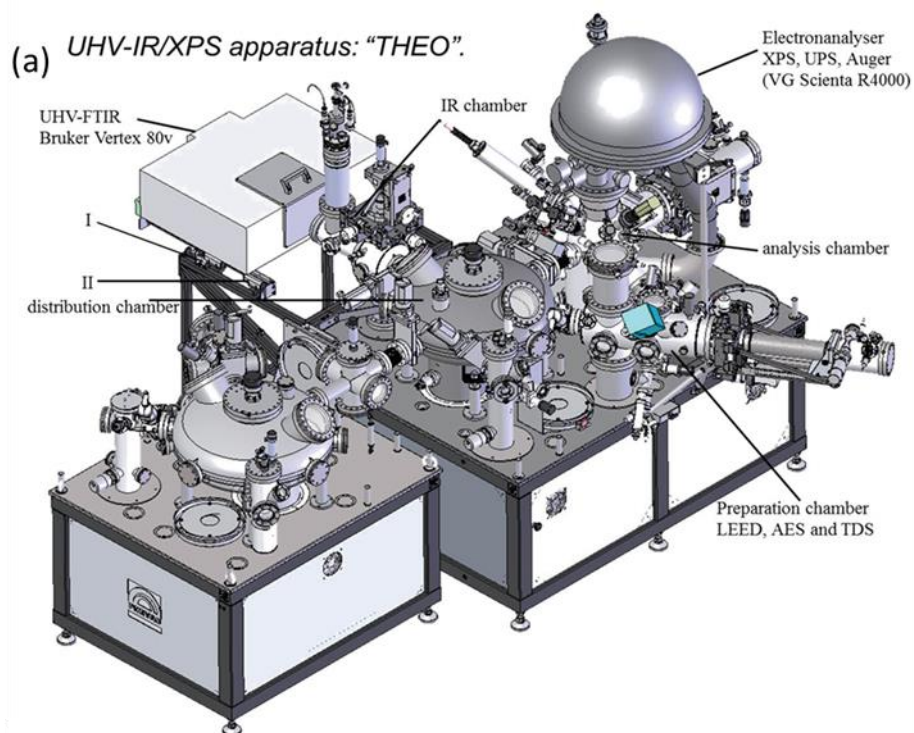


Figure 2.10 a) Technical drawing of UHV apparatus "THEO" at Karlsruhe Institute of Technology (KIT), Institute of Functional Interfaces (IFG), combining a state-of-the-art FTIR spectrometer (Bruker Vertex 80v) with a multi-chamber UHV system (Prevac). (1) Vacuum FTIR spectrometer. (2) IR chamber. (3) Electron analyzer (VG Scienta R4000). (4) Analysis chamber (XPS, UPS, and Auger). (5) Preparation chamber equipped with LEED, AES, and TDS. (6) Distribution chamber. (7) Load-lock. (8) Magazine. b) The side view of THEO.

Sample holders are used for transport of samples in UHV as well as for the heating and cooling treatments. **Figure 2.11** shows the PTS-H/K 1000 sample holder (PREVAC) that is specially designed for IR transmission measurements. This kind of sample holder provides electric resistance heating and is used for our FTIRS

measurements on oxide powder samples. The other sample holder (PREVAC, PTS-EB 1200) is equipped with a facility for electron-impact heating and is used for RAIRS experiments on oxide single-crystal and SURMOF surfaces. The samples mounted on this holder can be heated to 1500 K by electron bombardment. For IRRAS measurements, the IR beam is focused through KBr windows onto the sample at an incidence angle of 80° with respect to the surface normal. The reflected signal is collected by a focusing lens and detected by the liquid nitrogen cooled MCT detector.

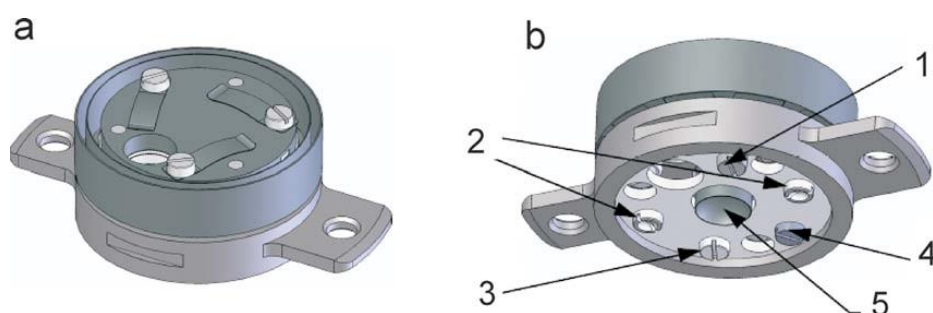


Figure 2.11 The specially designed sample holder (PREVAC, PTS-H/K 1000) for transmission measurements: (a) top view, (b) bottom view showing different contacts of: (1) potential/BIAS, (2) heating, (3) Ni thermocouple, (4) NiCr thermocouple, (5) cooling.

After the sample plate is fixed on the sample holder and all contacts are checked, the sample can be introduced into THEO. For this purpose, one of the two load-lock chambers should be vented first. The venting of load-lock chambers is within 15 minutes, and the pumping down to 10^{-7} mbar possibly needs 7 minutes. One of the load lock chambers is designed for the use of a special transport box, which allows samples to be transported to another system under UHV conditions. Transferring the sample to different UHV chambers attached to the distribution chamber is accomplished via a delicate transfer mechanism, which comprises a rotary feed through with a special gripper allowing for a fast and reliable transport of sample holders between different UHV chambers, each of them separated from the distribution chamber by a gate valve.

In the preparation chamber connected to the distribution chamber 2, the sample can be heated, cooled and sputtered. Vapor deposition of organic molecules and metals is also possible. There is a quartz crystal microbalance sample holder, with which the evaporation rate of substances can be determined. In the preparation chamber connected to the distribution chamber 1, it is possible to directly determine the surface

crystallinity and cleanness of single crystal samples by LEED and AES with a high resolution and sensitivity LEED/AES system (BDL800, OCI Vacuum Microengineering, Canada). With a quadrupole mass spectrometer 31(RGA 200) of Stanford Research Systems, adsorbate adsorption and reactions on surfaces can be monitored by TDS.

2.8.2 UHV-IRRAS

The heart of the UHV equipment is the IR chamber. The unique configuration enables UHV chamber to be directly coupled through differentially pumped KBr window flanges to an intact Bruker spectrometer VERTEX 80v, which has an actively aligned Ultra Scan interferometer, providing a spectral resolution of better than 0.2 cm^{-1} . Furthermore, the inner part of the spectrometer is evacuated to below 2 mbar. The differentially pumped windows between the UHV chamber and spectrometer sealed by Viton O-rings can be evacuated to a vacuum of better than 1×10^{-6} mbar. Thus, the entire optical path is kept in vacuum/UHV to avoid any absorption from atmospheric moisture and other gas species (e.g. CO_2).

The FTIRS experiments are conducted in the IR measurement chamber that is pumped by a TMP with large pumping speed (Leybold, TMP 361) and an oil-free fore-vacuum unit consisting of a TMP (TURBOVAC TW70) and a membrane pump. The base pressure in the main chamber amounts to 2×10^{-10} mbar. This chamber can also be used for sample preparation and is equipped with an ion gun for sample cleaning by Ar^+ sputtering and an atomic hydrogen source for exposing the samples to H atoms. The unique configuration of the measurement chamber enables us to directly insert this part of the UHV system into the modified sample chamber of the FTIR spectrometer for a compact connection see **Figure 2.12**. The UHV chamber is separated from the spectrometer through two KBr windows. For the space between them, we designed a compact connector sealed by Viton O-rings so that the enclosed space can be evacuated to a vacuum of better than 1×10^{-5} mbar. Thus, the entire optical path of the IR spectrometer is kept in vacuum/UHV to avoid the IR signals arising from gas phase absorption. In addition, the recording of spectra at grazing reflection of samples kept under UHV conditions is possible without introducing any new optical elements in the path of the IR light. The slightly modified beam path is realized by realigning one mirror inside the VERTEX 80v spectrometer. As shown in

Figure 2.12, the mirror M is movable to adjust the output beam direction. For reflection measurements, this mirror is tilted so that the IR beam can be focused on the sample surface at a grazing-incidence of 80° . The only new elements in the optical beam path are the two KBr windows for entering and leaving the UHV chamber and the substrate surface acting as a mirror. These two features, having an optical beam path evacuated to better than 1×10^{-5} mbar and having no additional optical elements, are considered to be crucial for the high-performance of this IR/UHV combination and guarantee high-quality IR data with high sensitivity and long-term stability, which are required to detect the very weak IR bands on single crystalline oxide surfaces.

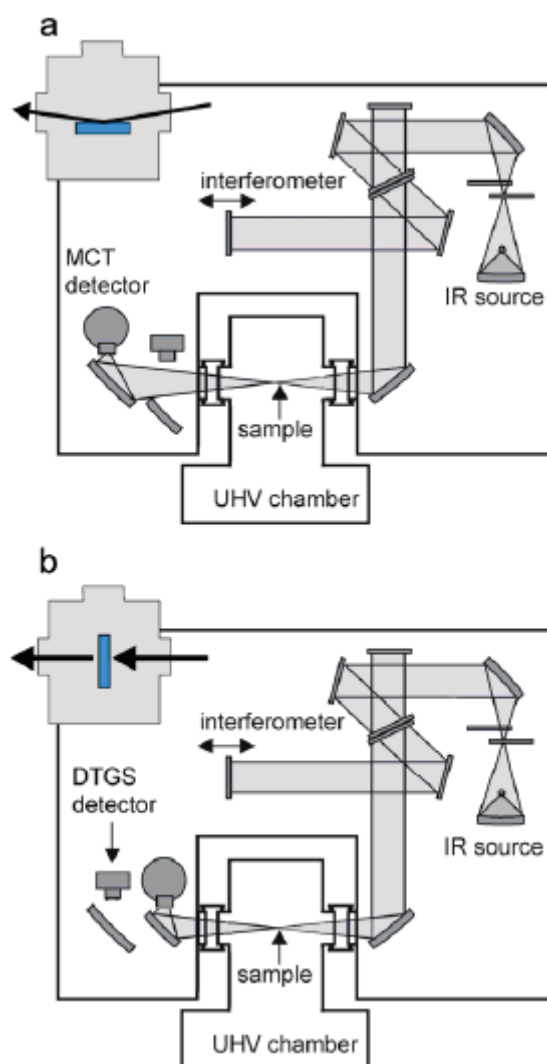


Figure 2.12 Schematic representation of different types of IR measurements: (a) reflection absorption at grazing incidence, (b) transmission.

The samples can be measured in both reflection and transmission modes. In order to measure in transmission mode (e.g. powder samples), the sample holder with a hole is used, and the sample is fixed to cover the hole. During measurements,

the sample holder is rotated by 90° , so that the beam after passing through the sample can be incident on the detector. The sample position is determined by a high precision 4-axis manipulator. The spectrometer is, in addition to the internal mid-infrared source (MIR), also equipped with a more powerful external light source. Another important component is the polarizer, with which one can measure using s- or p-polarized light and so it is possible to determine the molecule geometry on the surface. Time resolved step-scan and rapid-scan FTIR measurements can also be carried out in reflection and transmission modes, which can help in the investigation of kinetic processes. The detector chamber is equipped with two detectors to meet the particular research requirements: a liquid nitrogen cooled mercury cadmium telluride (MCT) detector and a room temperature operated deuterated triglycine sulfate (DTGS) detector. In order to better detect OH vibrations, an indium stibnite (InSb) detector is also occasionally employed, since it is more sensitive in the interesting wavelength range. The MCT detector is the most frequently used one due to its relatively high detectivity.

The measurement chamber hosts a high precision sample manipulator. **Figure 2.13** presents a schematic diagram showing the configuration of the manipulator capable of x, y, z translation and an R1 rotation. It is designed to allow precise placement of samples by operating the axes manually using micrometers x and y axes or handwheels z axis. A rotary drive is applied to provide rotation R1 around the x axis. All the translations and the rotation can also be operated automatically by stepper motors. A sample receiving station is mounted on the manipulator, which is equipped with electrical contacts for heating and temperature control thermocouple type K. The sample receiving station also contains pneumatically operated heating and cooling switches. Sample heating can be accomplished by making electrical connections to the sample holder at a pressure of 3 bar. When the pressure rises to about 6 bar, a sapphire ball is pressed against a counterpart made from copper and is thus thermally attached to the sample holder. In this way, the sample can be cooled down to temperatures of 100 K when using liquid nitrogen as the cryogenic liquid. The innovative design of the manipulator allows not only for grazing incidence reflection measurements on well-defined surfaces, but also for transmission measurements on oxide powder samples. For the latter type of experiments, a specially designed sample holder see discussion below is used. For this type of measurements, the manipulator is

rotated by 90°; together with a readjustment of the mirrors in the IR spectrometer, measurements in transmission can be performed.

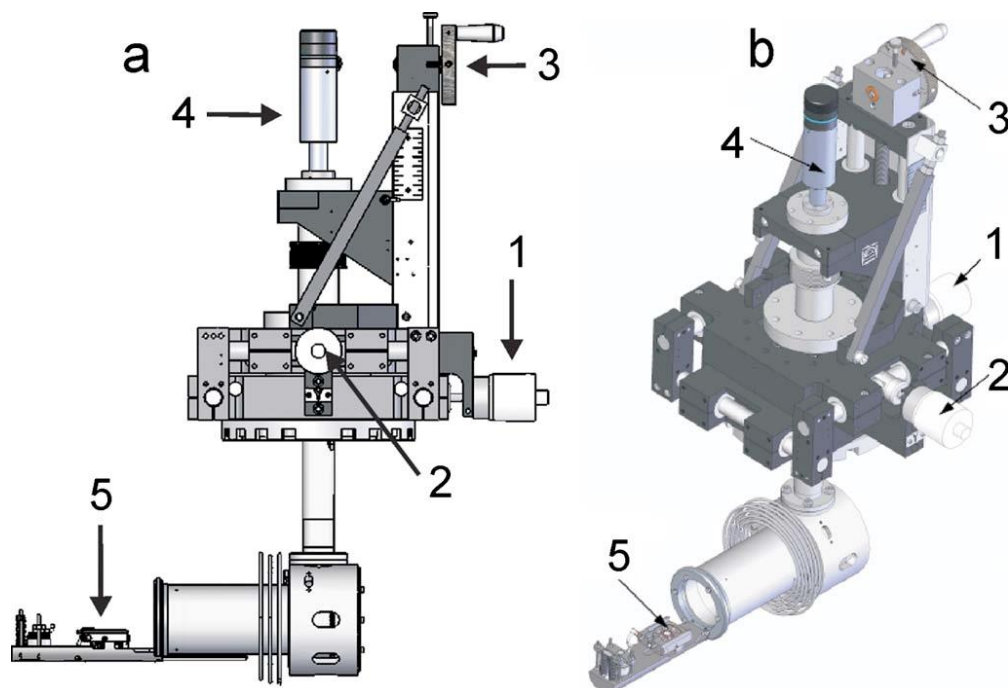


Figure 2.13 Schematic diagram of the high precision sample manipulator in (a) side view and (b) perspective view: (1) x axis micrometer, (2) y axis micrometer, (3) z axis handwheel, (4) R1 axis rotary feedthrough, (5) sample receiving station.

2.8.3 XPS

X-ray photoelectron spectroscopy (XPS), also referred to as electron spectroscopy for chemical analysis (ESCA), is the most widely used surface analysis technique for identifying chemical elements and their chemical states. XPS analysis is based on the photoelectric effect, where the photon source is X-rays of constant wavelength. Photons penetrate into material and excite electrons from the core levels to vacuum states. The kinetic energy distribution of the emitted photoelectrons (i.e. the number of emitted photoelectrons as a function of their kinetic energy) can be measured using an electron energy analyzer, and a photoelectron spectrum can thus be recorded.

The basic requirements for XPS experiments are (1) an X-ray source as a probe; (2) an electron energy analyzer, which can disperse the emitted electrons according to their kinetic energy, and thereby measure the flux of emitted electrons of a particular energy; (3) an ultrahigh vacuum (UHV) condition to enable the emitted

photoelectrons to be analyzed without interference from gas phase collisions. Such a system is illustrated schematically in **Figure 2.14**.

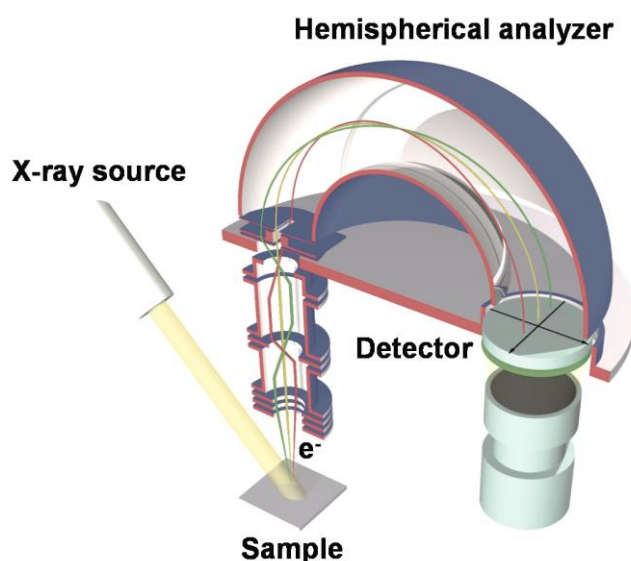


Figure 2.14 The components of X-ray photoelectron spectroscopy (XPS) experimental setup.

The most striking component of the analysis chamber is an electron energy hemispherical analyzer (Scienta R4000), which is used for various electron spectroscopy methods XPS, UPS and AES. A magnesium/aluminum anode acts as the X-ray source. An electrostatic charging of the sample can be reduced or avoided by bombardment with low-energy electrons (flood gun), so that even poor or non-conducting samples such as polymers and metal oxides can be examined with XPS. HeI or HeII radiation is used as a light source for UPS.

2.8.4 NEXAFS

Near-edge X-ray absorption fine structure (NEXAFS), which occasionally is also known as X-ray absorption near edge structure (XANES), is one of the most powerful techniques to explore the electronic and geometric structure of molecules adsorbed on solid surfaces by probing transitions from the innermost shell (K-shell) of an atomic species into unoccupied molecular orbitals. In a NEXAFS experiment, the incident energy of the photons is continuously varied over a certain energy range, and thus this technique clearly requires the availability of a high performance synchrotron source. The method has had its largest success when applied to low Z molecules (Z is the

atomic number), for which intense absorption edges are located in the soft X-ray region (100–700 eV).

The apparatus used to measure NEXAFS spectra is additionally equipped with complimentary surface analytical techniques, namely XPS/UPS, LEED and TDS. Especially for more complex systems the possibility to characterize samples by additional methods has been shown to be crucial for providing a unique and reliable interpretation of the experimental NEXAFS data. The scheme of such rather complex, multi-chamber UHV-system used by us is presented in **Figure 2.15**.

It consists of the analysis chamber (5) for NEXAFS/XPS measurements, the preparation chamber (2) equipped by evaporators (3), ion sputter guns and LEED system (4), a sample transfer system, including the distribution chamber (7) with the park-station (8) and two load lock chambers (1). This NEXAFS/XPS apparatus was designed and built by PREVAC (Poland) and is operated at the HESGM beamline of synchrotron facility BESSY II (Berlin, Germany). A photo of the setup is presented in **Figure 2.15b**.

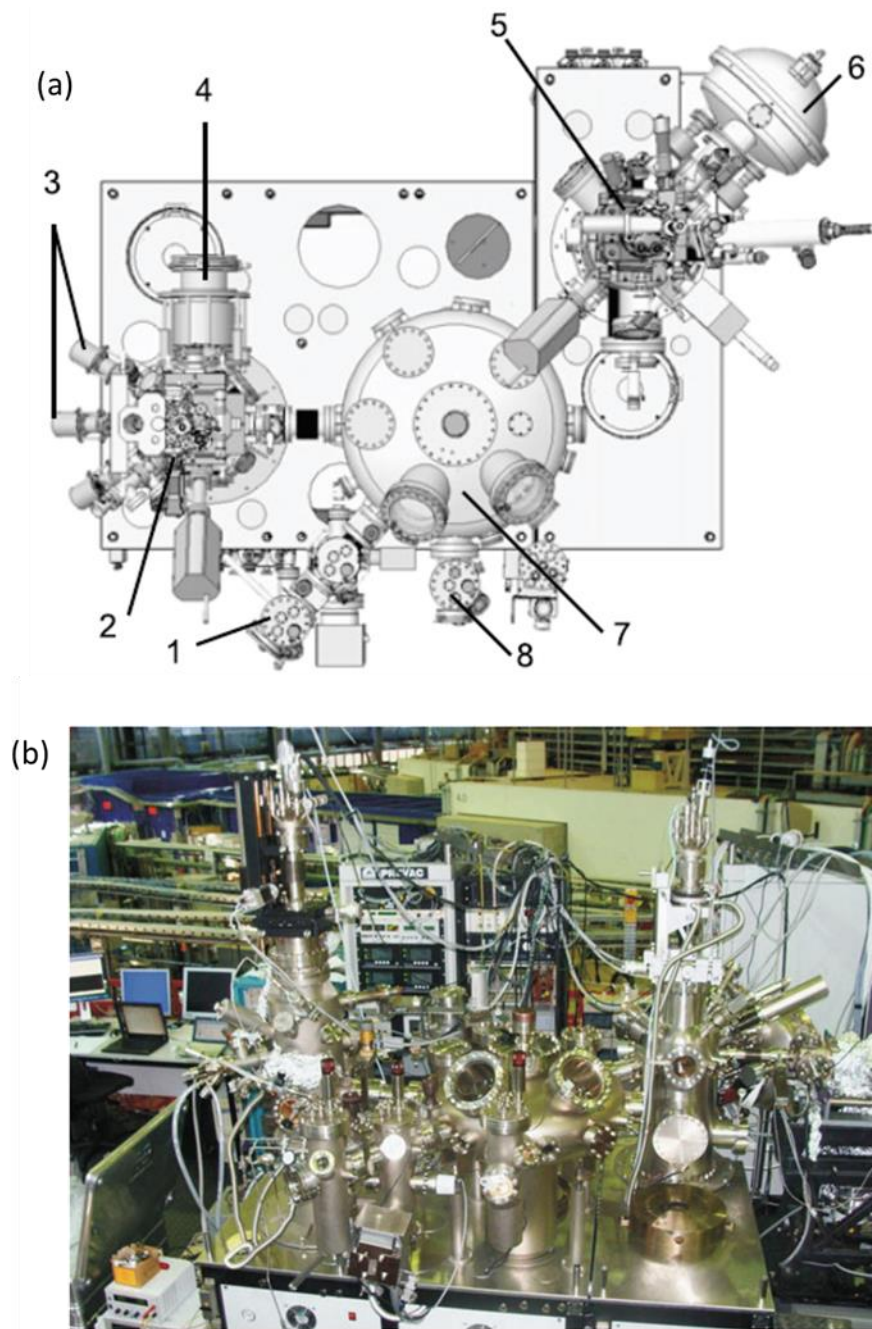
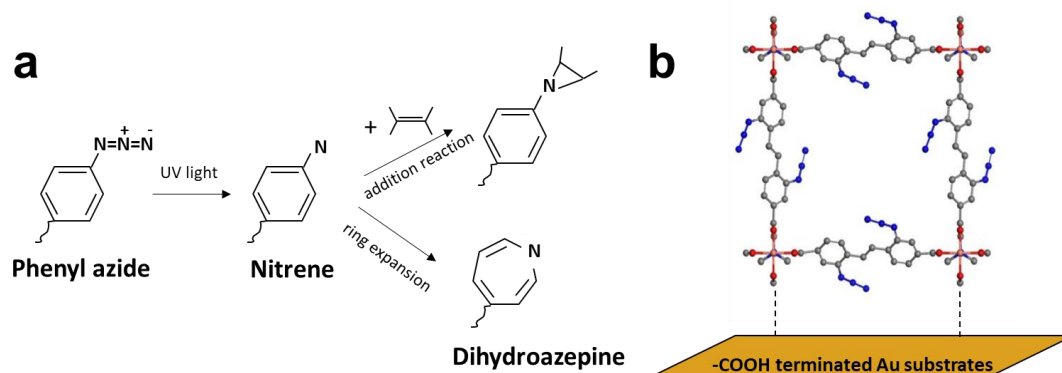


Figure 2.15 a) The drawing of XPS/NEXAFS system (top view). b) The view of XPS/NEXAFS end-station installed on HESGM beamline of synchrotron BESSY II in Berlin.

3 Photo-activation of Azide inside Cu-DA-SBDC SURMOF Matrices

3.1 Introduction

The huge potential of metal–organic frameworks (MOFs) results to vast applications as functional materials[3, 6, 157]. These crystalline, porous coordination polymers are assembled with ultra-high surface area, ordered porosity, and customizable organic functions. As a scaffold, it serves as a platform to loading functional groups. These functional groups are located at well-defined linker positions of a crystalline, porous lattice and are homogeneously dispersed within the MOF. MOFs thus provided a highly tunable platform to drive multicomponent organic photoreactions[158, 159]. For the catalytic photoreaction, photocatalytic [2+2] cyclizations of enones and Meerwein addition[160] and photocatalytic CO₂ reduction were reported[161]. Recently, construction of C-C bonds was achieved in the metal-organic-framework MFM-300(Cr) via photoreductive coupling of ketones and aldehydes groups[162]. In parallel to photocatalysis, photochemistry such as click chemistry was employed in the research field of porous organic polymers (POPs) and metal organic frameworks (MOFs). For example, Devic and coworkers were able to introduce the azide-alkyne 1,3-dipolar cycloaddition into MOFs field in 2007[163]. Using “click” chemistry, differently functionalized porous material with internal or external surfaces were fabricated[164]. However, there is still lack of understanding how these photoreactions evolved in MOFs. SURMOFs (surface mounted metal organic frameworks) growth on gold substrate showed high quality on crystallinity and morphology with very low defects, which are an excellent model system and quit suit for the surface characterization[14]. These MOF thin films offer great potentials for the investigation of organic reaction mechanism (**Scheme 3.1**).



Scheme 3.1 a) Possible pathways of the photoactivation of phenyl azide. b) Structure of SURMOF Cu-Da-SBDC.

As an intriguing element in click chemistry, organic azides also served as powerful precursors, which can be easily transformed into functional molecules such as amines, isocyanates and so on[165]. Other nitrogen containing heterocycles are also achievable origin from decomposition or addition reactions of azides. The other attracting point of the photolysis of phenyl azides lies in the commercial interest in making photoresists[63], the use of aryl azides in photoaffinity labeling. Under UV irradiation or heating, an azide group can be split into a super activated nitrene group and release a N_2 molecule in aryl azide compounds. The latter reaction paths based on nitrene group depend on the condition applied (**Scheme 3.1a**). Over the last decade, modern time - resolved spectroscopic techniques up to Femtosecond level and DFT calculations have been successfully applied and reveal the detailed description of azide photochemistry.

IR spectroscopy has been exploited as an effective method to observe the evolution of photolysis. In 1978, Chapman and LeRoux detected the formation of ketenimine using matrix isolation IR spectroscopy[166]. Irradiation of phenyl azide in an argon matrix at 8 K with light of $\lambda > 360$ nm (or $\lambda > 216$ nm) led to the formation of a product giving an intense IR band at 1895 cm^{-1} characteristic of a heterocumulene structure ($-\text{N}=\text{C}=\text{C}-$). Cyclic ketemimine has been detected by matrix IR spectroscopy and in solution by nanosecond/ microsecond time-resolved UV-vis and IR spectroscopy[167]. More recently, photochemical rearrangements with aryl nitrenes arises as a new area of research. Yet both the complexity of the possible products and the diverse applications makes this area of research of special interests. Conventionally, organics in reactions are observed in solvent. The solvent effect,

however, sometimes makes it even more complicated, thus hamper to understand the real paths way of mechanism learning. Additionally, in the presence of oxygen, photolysis of the dilute hydrocarbon solutions ($< 10^{-4}$ M) of simple derivatives of phenyl azides was reported to give the corresponding nitrosobenzenes[168].

In order to gain an atomic-level understanding of photoactivation of azides and the mechanism while eliminating the interference effect of solvent and atmosphere, an extensive experimental study has been carried out herein. By employing UHV-IRRAS, in situ XRD, MS and XPS, we have established a model system using the azide-SURMOFs to study the photoactivation of phenyl azide and its reaction pathways (**Scheme 3.1b**). Here, for the first time, we visualized the photoactivation reaction in situ.

3.2 Experimental

All chemicals were purchased from commercial sources and used without any further purification if not indicated differently. Copper acetate monohydrate was purchased from Merck; methanol was purchased from VWR Chemicals.

(1) Preparation of Cu-DA-SBDC SURMOFs

The Cu-DA-SBDC samples were grown on Au substrates (100-nm Au/5-nm Ti deposited on Si wafers) using a spray method[169]. Before the growth of samples, gold substrates were functionalized by self-assembled monolayers, SAMs, of 16-mercaptohexadecanoic acid (MHDA). These substrates were then mounted on a sample holder and subsequently sprayed with a 1 mM solution of copper acetate monohydrate in methanol and a methanolic solution 0.1 mM of DA-SBDC at room temperature. The number of spray cycles employed was set as 60. After synthesis all samples were characterized with X-ray diffraction (XRD).

(2) X-ray Diffraction (XRD).

Coplaner (out-plane) XRD was carried out on a Bruker D8 Advance in θ - θ geometry equipped with a Si-strip detector (PSD Lynxeye®). On the tube side, a variable divergence slit set to V12 (fixed slit with 12 mm opening) and on the receiving side a 2.5° Soller slit was used. In-situ Scans under UV illumination (@ 254 nm) ran from 4° to 6° 2 θ for the (100) Bragg-peak, 9 to 11°2 θ for (200) and from 15 to 17°2 θ for

(300) with a step width of $0.019^\circ 2\theta$ and 1 seconds per step, which resulted in a total step counting time of 84 seconds due to the specific PSD settings. Evaluation of data was done with Bruker evaluation software DIFFRAC.EVA 5.2 and TOPAS 6.0. After background correction, the peak positions were calibrated using from the Au-substrate the position of Au (111) peak which was measured in each run. For the non-coplanar (in-plane, IP) orientation a Bruker D8 Discover equipped with a quarter Eulerian cradle, tilt-stage, 2.3° Soller-slits on both sides, a Göbel-mirror, and a PSD Lynxeye® in θ - 2θ geometry, was applied. The XRD data was acquired over a 2θ range of 2 to $20^\circ 2\theta$, with 1 seconds per $0.02^\circ 2\theta$ -step. The peak positions were calibrated using from the Au-substrate the position of Au (220) peak. Both machines used Cu-anodes utilizing the Cu $K\alpha_{1,2}$ -radiation ($\lambda = 0.154018\text{nm}$)

(3) Infrared (IR) Spectroscopy.

The IRRA spectra were recorded on a Bruker VERTEX 80 FTIR spectrometer. Perdeuterated hexadecanethiol-SAMs on Au/Si were used for reference measurements.

(4) High Resolution Mass Spectrometry (MS and HRMS).

Mass spectra were recorded with a Finnigan MAT 95 (70 eV) spectrometer under electron impact (EI) conditions. The molecular fragments were quoted as the relation between mass and charge (m/z).

(5) UHV-IRRAS and IR experiments

The as received Cu-DA-SBDC SURMOF samples were transferred to the above-mentioned THEO UHV apparatus.

(6) Scanning Electron Microscopy (SEM)

The morphology measurements are carried out in a FEI Philips XL 30 Field Emission Gun Environmental Scanning Electron Microscope (FEG-ESEM). To avoid charging, insulating materials have to be coated with a thin Gold/Palladium film. Then the specimen can be imaged under high vacuum conditions (10^{-5} Pa) using acceleration voltages between 5 and 20 kV.

(7) Simulations

The simulations of XRD pattern and structure of the azide MOF were performed by using the SimStack and Material Studio softwares.

(8) Study of solvent effects

The as-synthesized azide-containing Cu-Da-SBDC SURMOF samples were placed into 5 mL of THF, ethanol, H₂O, cyclohexane, and heptane solutions, respectively. Then the samples were illuminated under 254 nm UV light in the different solutions for 50 minutes. The samples obtained after the illumination were characterized by the IRRAS.

3.3 Results and discussion

3.3.1 Pristine film characterization

Highly oriented and crystalline Cu-(Da-SBDC) SURMOFs with azide groups were prepared on -COOH functionalized gold surfaces via layer-by-layer deposition fashion. XRD results confirmed that the obtained structure of SURMOFs was highly crystalline and grown in (001) orientation[169].

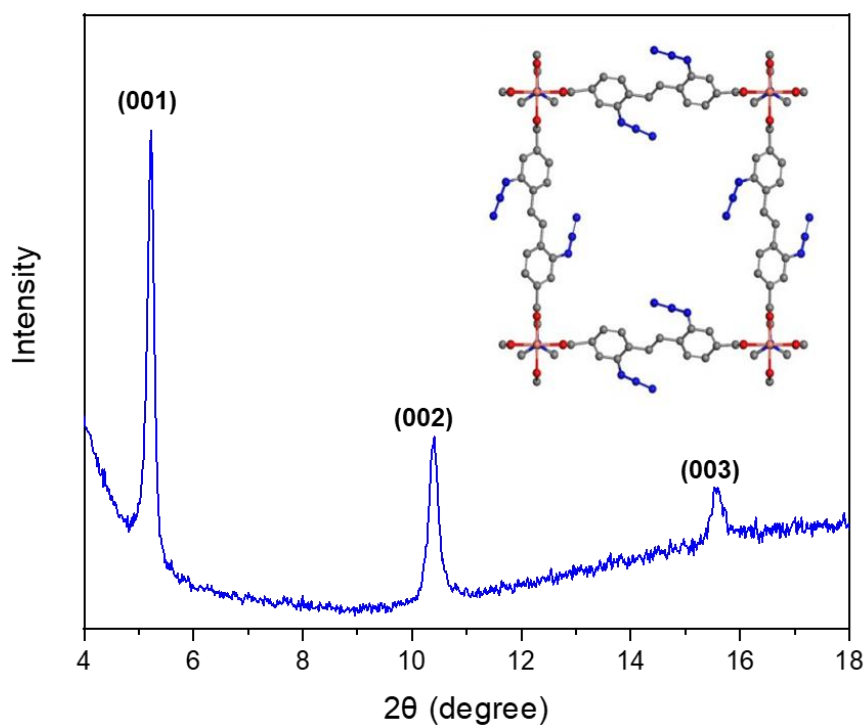


Figure 3.1 XRD data of Cu-DA-SBDC SURMOF before UV illumination.

With aid of IRRAS, characteristic vibrational band at 2127 cm^{-1} demonstrated the azide groups (**Figure 3.2**). Vibrational bands at 1602 and 1428 cm^{-1} could be ascribed to the $\text{C}=\text{O}$ vibrational band in the carboxylic acid group. The $\text{V}(\text{cc})$ ring vibration from the phenyl ring shows in 1558 cm^{-1} . SEM images presented flat and plane surface morphology of the thin film (**Figure 3.3**).

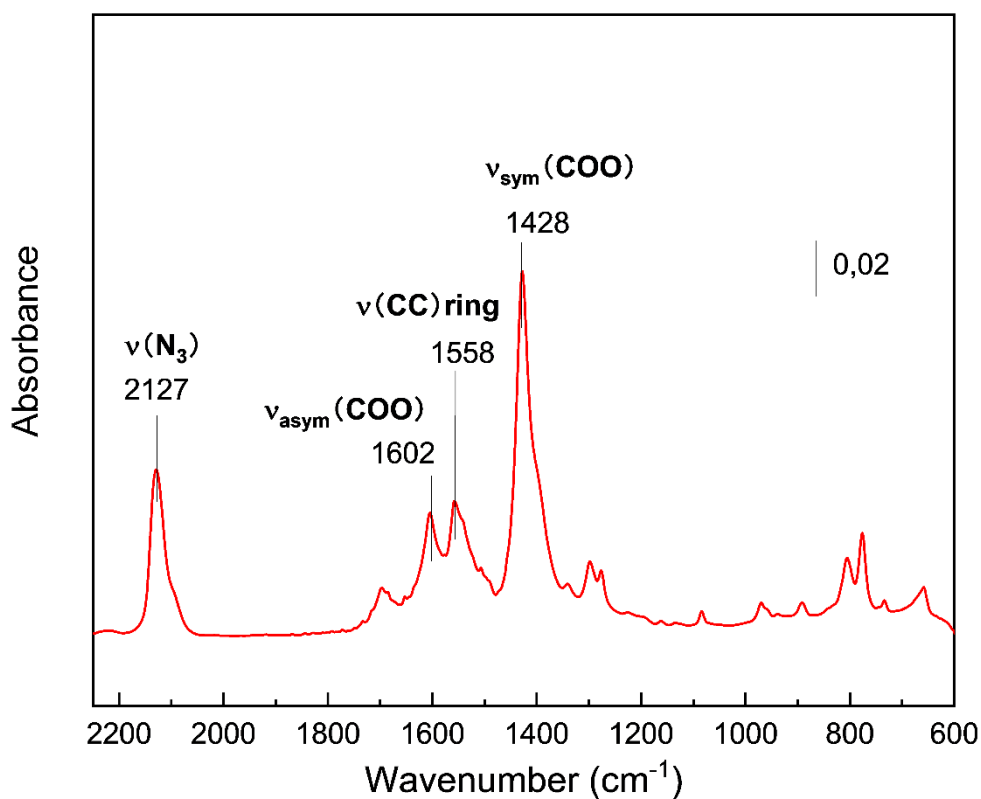


Figure 3.2 IRRAS spectra of Cu-DA-SBDC SURMOF before UV illumination.

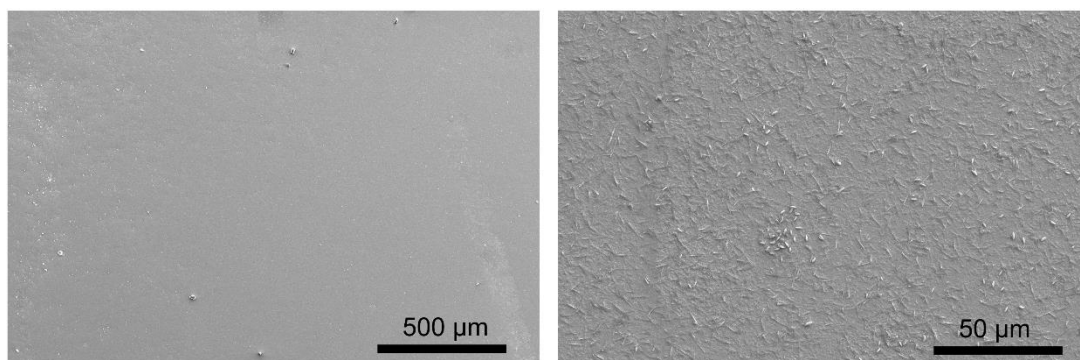


Figure 3.3 SEM images of Cu-DA-SBDC SURMOF before UV illumination.

3.3.2 In situ photoreaction under IRRAS observation

The photochemistry of azides was characterized in situ in a UHV chamber equipped with infrared reflection absorption spectroscopy (IRRAS) apparatus in THEO. As shown in **Figure 3.4a**, upon illumination with UV light on, the azide band ν_{N_3} at 2127 cm^{-1} started to decrease in intensity. Also, for the band at 3058 cm^{-1} , assigned to the vibration of C-H groups in HC=CH a reduction in intensity was observed (**Figure**

3.5). Notably, the benzene ring CH vibrations at 2927 cm^{-1} and 2856 cm^{-1} as well as the C-C vibrations at 1558 cm^{-1} remained unchanged in intensity. Importantly, illumination led to the occurrence a one new vibration band at 1250 cm^{-1} . We assign this peak tentatively to vibrations in C-N-H groups formed in the course of the photochemical reaction. This assignment is in accordance with previously observed in-plane deformation mode in NH at 1120 cm^{-1} [170].

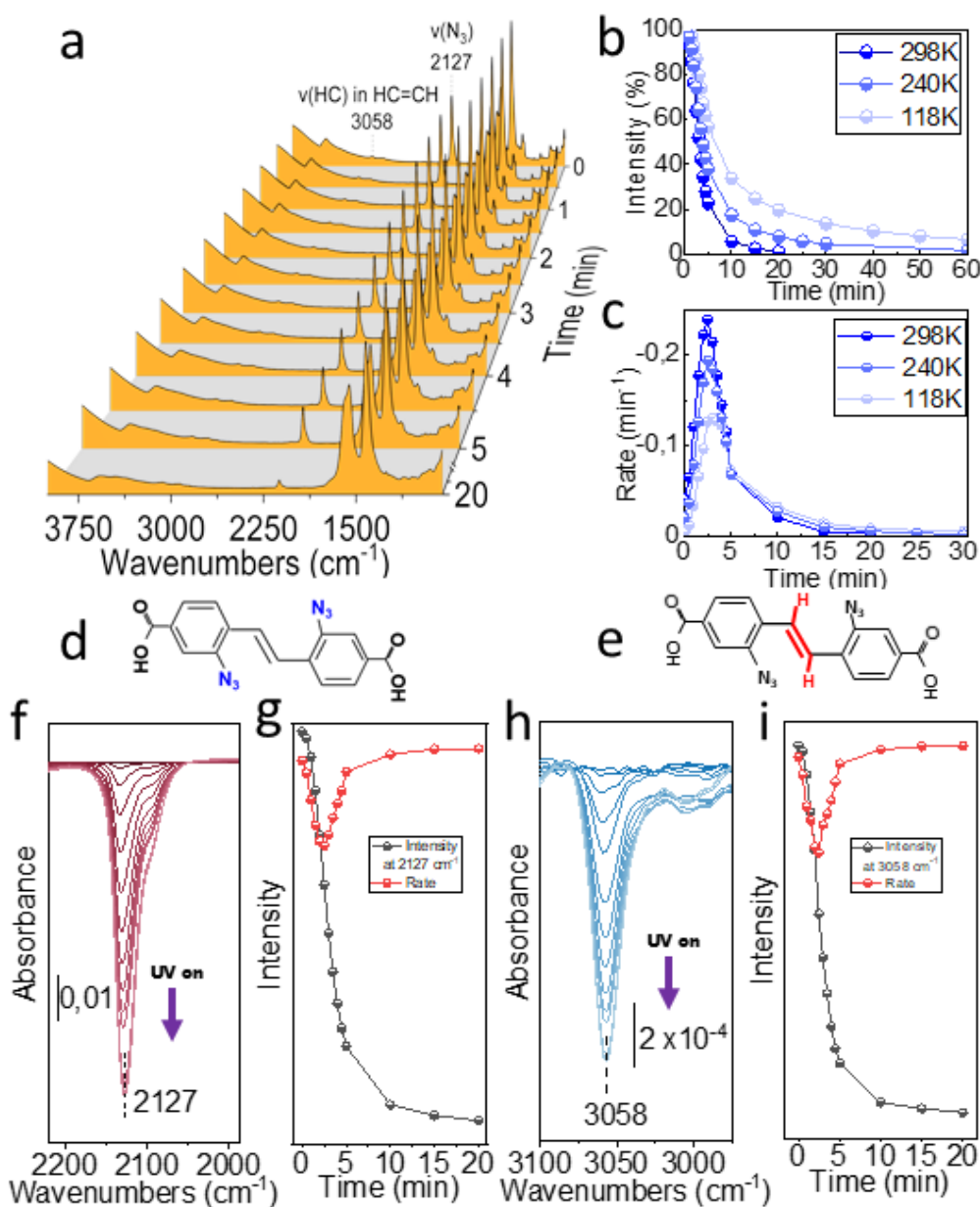


Figure 3.4 a) In situ UHV-IRRAS under UV illumination at 298K. b) Changes of peak intensity at 2127 cm^{-1} . c) Relative rate of consumption of peak intensity at 2127 cm^{-1} . d-e) Molecular structure and character bands of linker Da-SBDC. f) Detailed evolution of peak at 2127 cm^{-1} . g) Evolution of peak intensity and consumption rate at 2127 cm^{-1} . h) Detailed evolution of peak at 3058 cm^{-1} . i) Evolution of peak intensity and consumption rate at 3058 cm^{-1} .

The time dependence of the ν_{N_3} band intensity shown in **Figure 3.4b** reveals a continuous decrease, at 298 K the intensity almost completely disappeared after 20 min. At lower temperatures the decrease gets slower. The reaction rates are shown in **Figure 3.4c**, revealing an initial increase followed by a steep decrease. The highest reaction rates are observed for the highest temperature (298 K).

In **Figure 3.4f-i** the different vibrational bands are shown in more detail. The rates of intensity decreasing at bands 3058 cm^{-1} and increasing at 1496 cm^{-1} over time were taken into consideration. Coincidentally, the decreasing intensity at bands 3058 cm^{-1} showed a similar trend to the decreasing at bands 2127 cm^{-1} . The consuming rate of both increased in the first 2.5min, reaching their maximum, then decreased till the end. This finding indicated the addition reaction between two groups, ν_{CH} stretching in $-\text{HC}=\text{CH}-$ at 3058 cm^{-1} and vibration of ν_{N_3} at 2127 cm^{-1} .

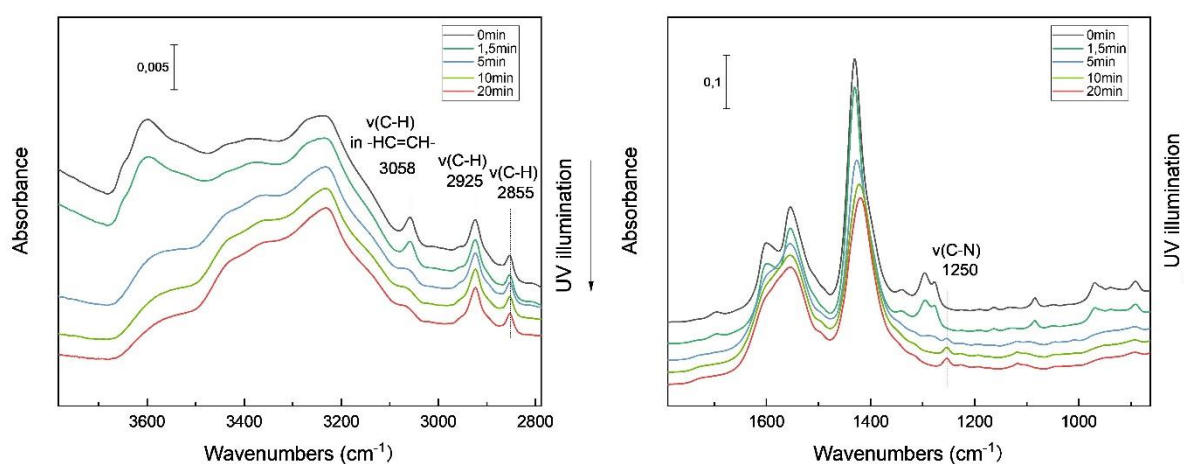


Figure 3.5 UHV-IRRAS spectra of Cu-DA-SBDC SURMOF under UV illumination, 298K.

Due to the dipole character of azides, they could undergo cycloadditions with alkenes. Meantime, the possibility that formation of dihydroazepine with the insertion of N atom into aryl ring could be ruled out. Dihydroazepine motif would bring very strong vibration peaks around 1891 cm^{-1} if existed. In our case, however, there was no obvious peaks present at 1891 cm^{-1} , nor the change in the 1558 cm^{-1} from the vibration of $\nu(\text{cc})$ ring. Therefore, rearrangement of aryl nitrenes did not happen here. Additionally, in the presence of water, alkenylaryl azide could provide access to substituted azepinones by ring expansion. While in a UHV chamber under $\sim 1 \times 10^{-10}$ mbar, the existence of water could be also eliminated.

Normally, loss of nitrogen from organic azides results in uncharged monovalent nitrenes intermediates, which have a short lifetime (only several microseconds) with the activation energies with nitrogen elimination on the order of -40 kcal/mol[171]. Under UV light, the photolysis of azide groups may result in an insertion of N atom into the phenyl ring motif, generating an azepine. The solution phase photochemistry of phenyl azide is reported to be temperature dependent[172]. Photolysis of phenyl azide in the presence of diethylamine at ambient temperature yields azepine. Lowering the temperature suppresses the yield of azepine and below 160 K, azobenzene, the product of triplet nitrene dimerization, is produced. In this case, a variety of experiments were conducted under 298K, 240K, 118K. It was found that testing under lower temperature leads to slower transformation (**Figure 3.4b**), but still same trend of evolution as shown in **Figure 3.6**. So, in our case it presents no obvious difference whenever tested under 298K, 240K, 118K.

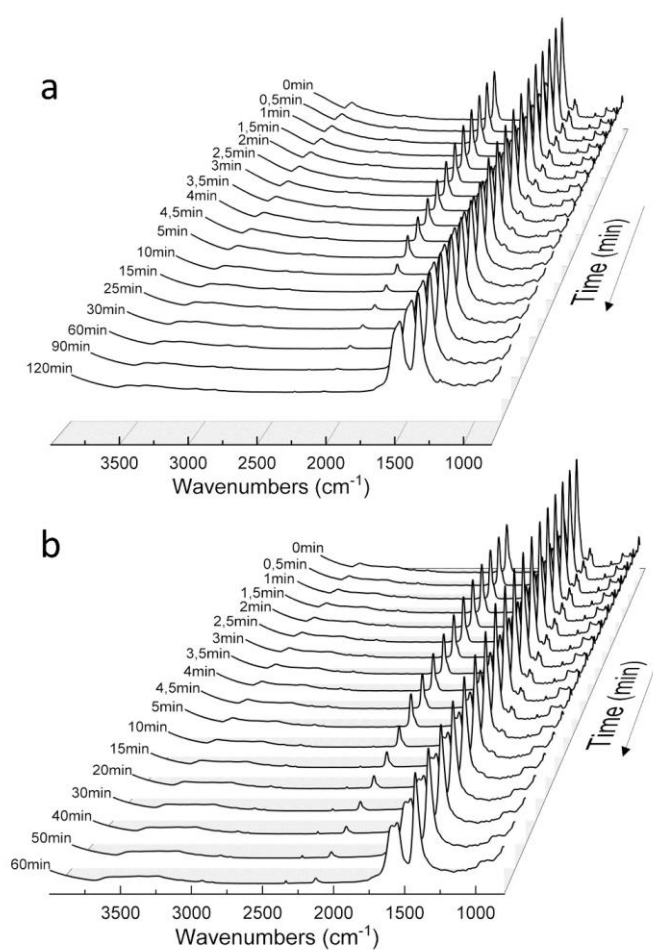


Figure 3.6 In situ UHV-IRRAS under UV illumination 254nm, at 240K a) and 118K b).

3.3.3 Chemical and structural changes during photoreaction

Further information on the photochemical reactions was provided by recording XPS spectra before and after UV illumination. **Figure 3.7** shows a doublet in the N 1s regions, with a peak at 403.6 eV attributed to the N species directly attached to the Phenyl ring and a second peak at 400.2 eV assigned to the two lateral nitrogen atoms[173]. The relative ratio of the two peak areas is close to 1:2, as expected[174]. The small peak at 298.9 eV is ascribed to a small fraction of decomposed azide. After UV illumination, the band at 403.6 eV was to be completely absent, indicating a complete transformation of azide groups. A quantitative analysis (see **Table 3.1**) yields a loss of about 40% of the nitrogen atoms, in agreement with the decomposition of the N₃ species into gaseous N₂ and a remaining N species.

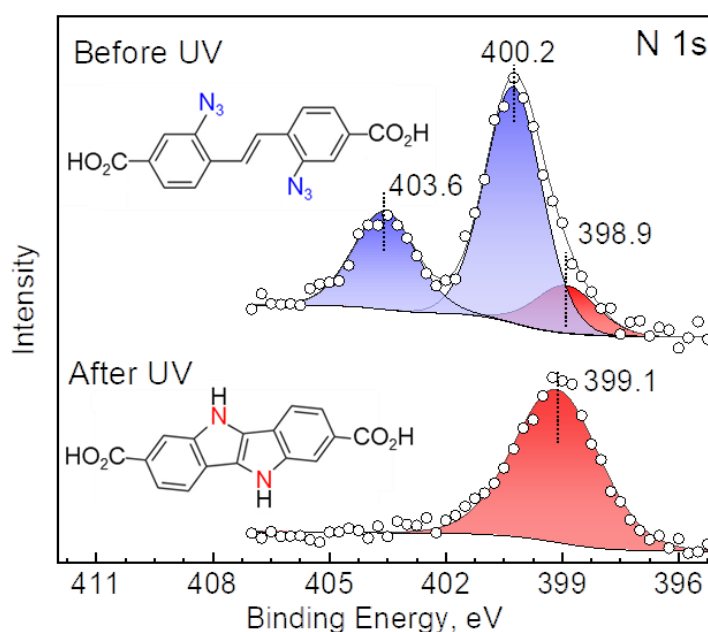


Figure 3.7 XPS N 1s spectra before and after UV illumination.

Table 3.1 Peak area in XPS before and after illumination.

	Before illumination		After illumination	
Peak position (eV)	403.6	400.2	398.9	399.1
Peak area	66702.7	156694.3	51536.8	161541.8
Total peak area	274933.8		161541.8	
Total peak area ratio^[a]	1: 0.59			

[a] Total peak area ratio before: after UV illumination.

A striking advantage of MOFs is their crystallinity. Comparison of XRD results recorded before and after UV illumination (see **Figure 3.8**) allowed to determine length changes of the azide linkers. Out-of-plane as well as in-plane XRD patterns revealed the presence of well-defined diffraction peaks, indicating that crystallinity is largely preserved during the photochemical reaction. Importantly, the XRD peak positions were observed to shift to higher angles, for the (001) peak from 5.1 to 5.8 degree. This observation directly implies a shortening of the linkers upon UV illumination. For the second and third order peaks (002) and (003), they almost disappeared, which was likely due to the shrinking of MOF linkers and contribution of strain. More strain would be imposed into the structure when cycloaddition reaction happened in MOFs under UV light[175]. The spectral evolution of the azide groups, C=C, and C-N vibrations could be related to the addition reaction between azide groups, C=C along with compress effect of strain. SEM images (**Figure 3.9**) showed no obvious variation, which also supported the structural stability.

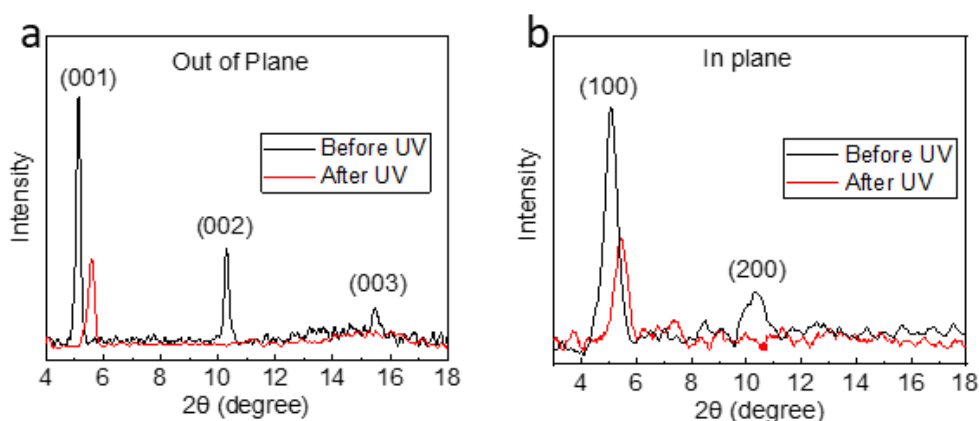


Figure 3.8 Out of plane a) and in plane XRD b) before and after UV illumination.

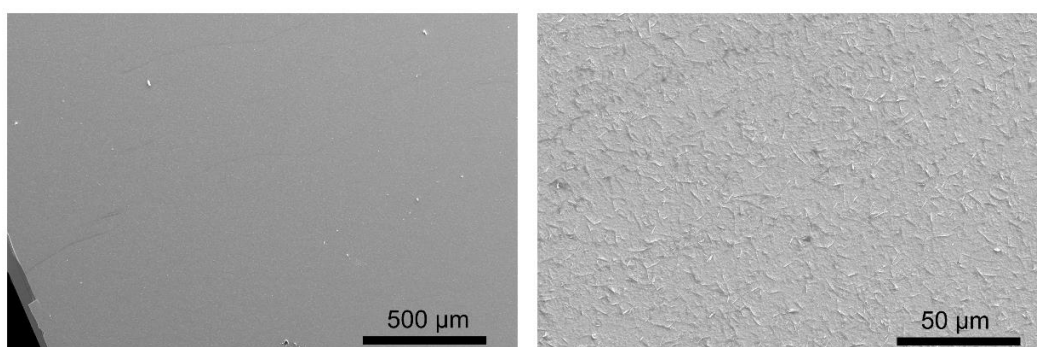


Figure 3.9 SEM images of Cu-DA-SBDC SURMOF after UV illumination.

In situ XRD tests were also performed to further investigate the time resolved evolution of the SURMOFs structure in **Figure 3.10**. Note, weaker intensity of UV

light was required to slow down the photoactivation thus enable viable collection of XRD patterns. For the (001) plane, the intensity of it decreased in the first 200 min. Then it maintained almost unchanged when azide groups were exhausted, consistent with the IRRAS in **Figure 3.4**.

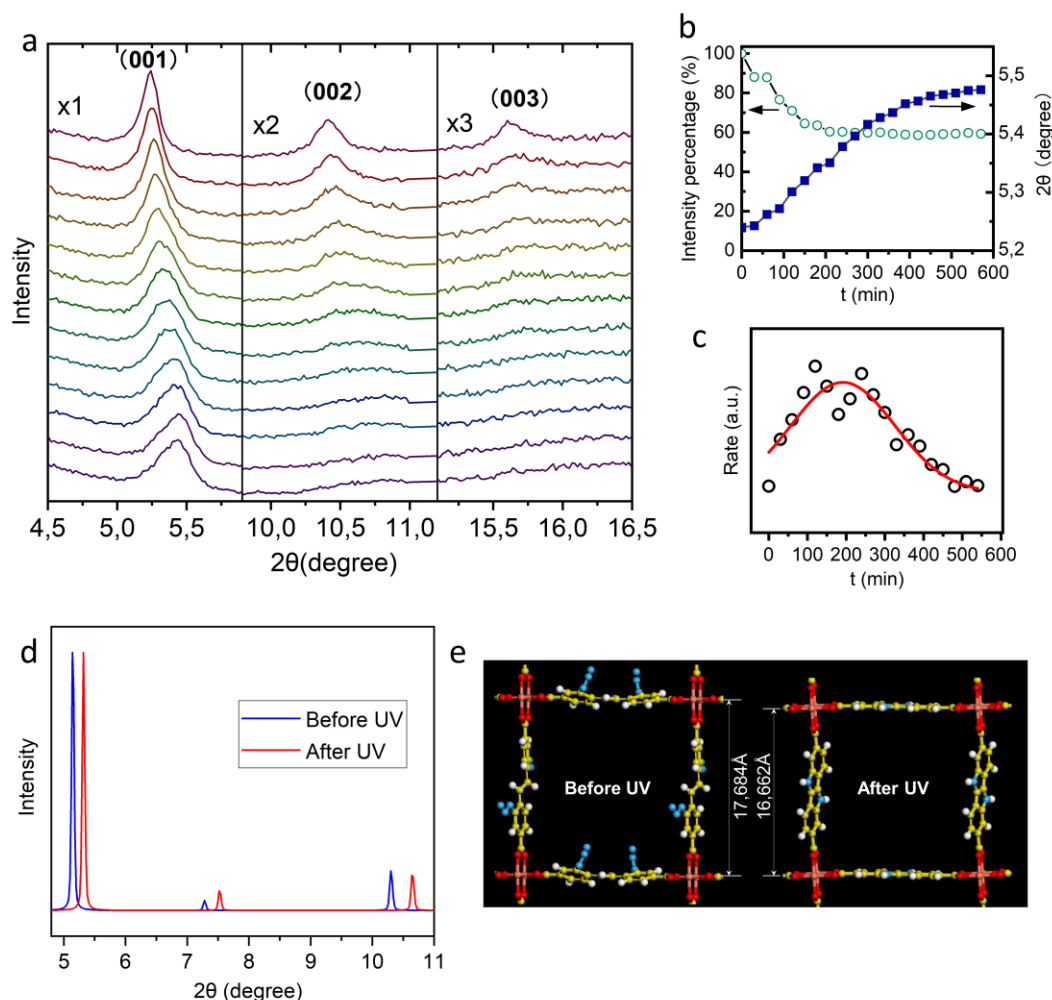


Figure 3.10 a) In situ XRD of SURMOFs Cu (Da-SBDC) under UV illumination. b) Evolution of intensity and position of 001 peak. c) Peak position shifting rate of 001 peak. d) Simulated XRD patterns before and after UV illumination via Material Studio.

As shown in **Figure 3.10b**, 60% of the intensity remained in the following 400 min, indicating the structural changes and proper stability. The diffraction peak location increased gradually from 5.2 to 5.5 degree in a 600 min in situ testing, which is agreed with ex situ XRD in **Figure 3.8**. Due to the shrinking of linkers, mechanical lattice strain increases rapidly in the beginning, leading to an increasing of reaction rate for azide. As a result, the 001 peak shifting rate followed a volcano curve (**Figure 3.10c**). The ring strain was proved to accelerate Azide-Alkyne Cycloaddition[176]. Upon one of the two azides group in the Da-SBDC linker forming a cyclization structure with C=C double bond, the other could be promoted to react with C=C

double bond. It was also consistent with the phenomenon observed in IRRAS. For consuming rate of V_{CH} stretching in $-HC=CH-$ at 3058 cm^{-1} and generation rate of V_{C-N} at 1724 cm^{-1} , they followed the same trend, firstly increases then decreases and extremum rates for each are all shown at 2,5 min. The lattice spacing decreased continuously from 17.161 \AA as UV illumination on to 16.434 \AA calculated from the first order peak. The simulated XRD data curve (**Figure 3.10d**) for these structures agreed well with the experimental findings for both samples before and after UV illumination. Simulated lattice spacing decreased from 17.684 \AA to 16.662 \AA (**Figure 3.10e**).

On the basis of these observations, it is thus proposed that a pyrrole compound was formed under UV illumination of SURMOF. As an important moiety in pharmaceuticals industry, pyrrole motifs were reported to be synthesized via irradiation of vinyl and aryl azides with visible light in the presence of Ru photocatalysts, or from dienyl azides at room temperature using catalytic amounts of ZnI_2 or $Rh_2(O_2CC_3F_7)_4$ [177]. Notably, these experiments were performed either in the organic solution CH_3Cl or CH_2Cl_2 . In our case, UV light is the only intriguing fact to boost the formation of pyrrole without catalysts. This reaction found several applications in the total synthesis of natural product, as for instance Murphy's synthesis of aspidospermidinevindoline, horsfiline, and coerulecine. Formal insertion into $C(sp^2)H$ bonds is a frequently used reaction, which in part also follows the cycloaddition principle. Thus indoles, carbazoles, and other heterocycles can be formed. Early mechanistic investigations showed that the nitrogen atom in the product originates from the probable nitrene precursor. The choice of the correct solvent, which also influences the thermolysis temperature, is pivotal for success. 2H-Azirines can otherwise occur as by-products. Dimerization can also give pyrazines. While here in our system, there is no solvent to be used. For the synthesis of pyrroles, the Hemetsberger reaction can also be used when dealing with α -unsaturated aldehydes[178]. As a type of pyrrole-containing heteroacene, indolo[3,2-b]indole (IDID)-based π -conjugated p-type semiconductors were widely used in organic light-emitting diodes (OLED), organic field-effect transistors (OFET), and organic photovoltaics (OPV)[179, 180].

Comparing the IRRAS spectra ambient atmosphere (**Figure 3.11**), there were no obvious difference except that there was much more noise in the later, which make it harder to interpret. This also indicates that the O₂ and moisture in ambient are not involved in the reaction pathway. The high dilution of solutions of phenyl azide is found to suppress polymer formation and azobenzene forms instead[173]. Using linkers as the isolated functional group present an inner molecular reaction, this also avoids inter-molecular side reactions.

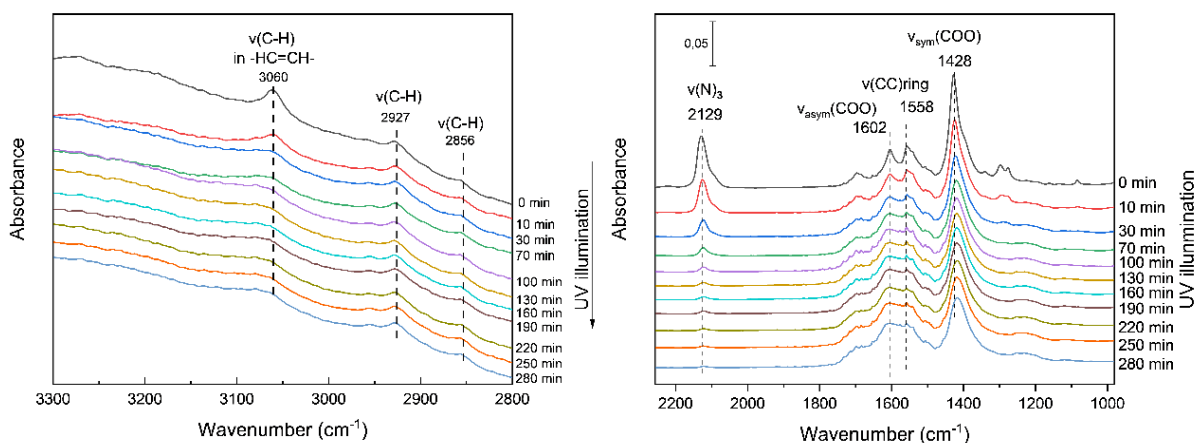


Figure 3.11 IRRAS spectra of Cu-DA-SBDC SURMOF under UV illumination at ambient atmosphere, 298K.

A mechanism thus proposed here. For the first step, immediately happened photo splitting of azide and formation of nitrene under UV illumination. Followed in the second step, addition reaction between nitrene and C=C, resulting in the newly formed C-N bonds. To verify this hypothesis, MS spectra patterns were obtained to further study the transformation of linkers as illustrated in **Figure 3.12**. SURMOF samples on gold were dissolved in a 10% acetic/ethanol solution for 30 min before MS characterization. As the results shown, compounds with the m.w. of 349 dominated before UV illumination while compounds with the m.w. of 293 increased significantly after UV illumination. This proved the formation of indolo[3,2-b] indole in the photoreaction process.

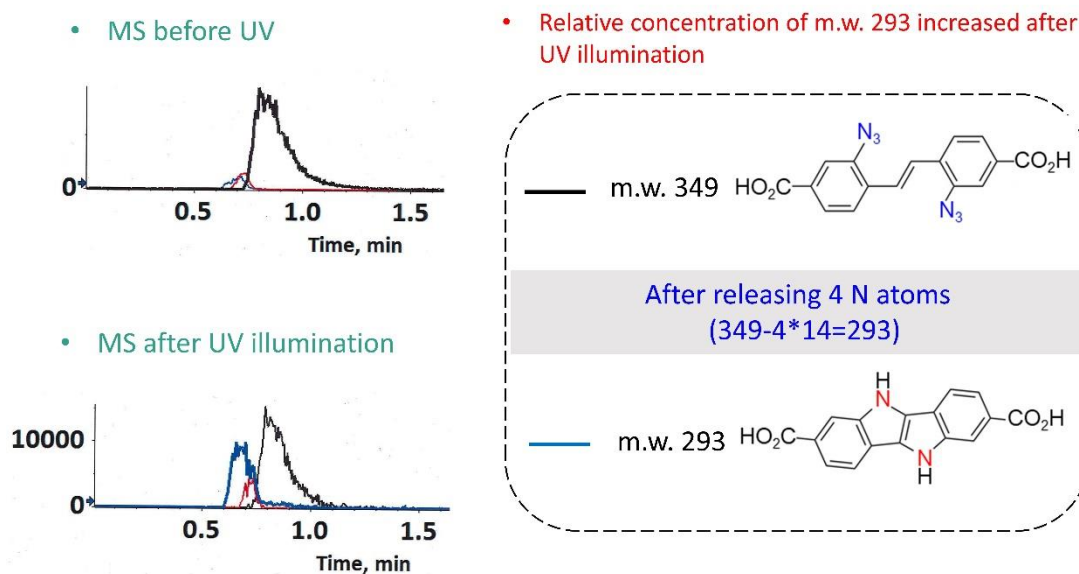


Figure 3.12 MS spectra of Cu-DA-SBDC SURMOF before and after UV illumination, 298K.

3.3.4 Study of solvent effects

Formal insertion into C(sp²)-H bonds is a frequently used reaction that partly follows the cycloaddition principle. Thus indoles, carbazoles and other heterocycles can be formed. Again, here in our systems, the photochemical reactions of azide occur in activated SURMOFs, in which the solvent effects and any side reactions are avoided. To illustrate this important point, the impact of diverse solvents on the photolysis of azides in SURMOFs has been investigated (see **Figure 3.13**).

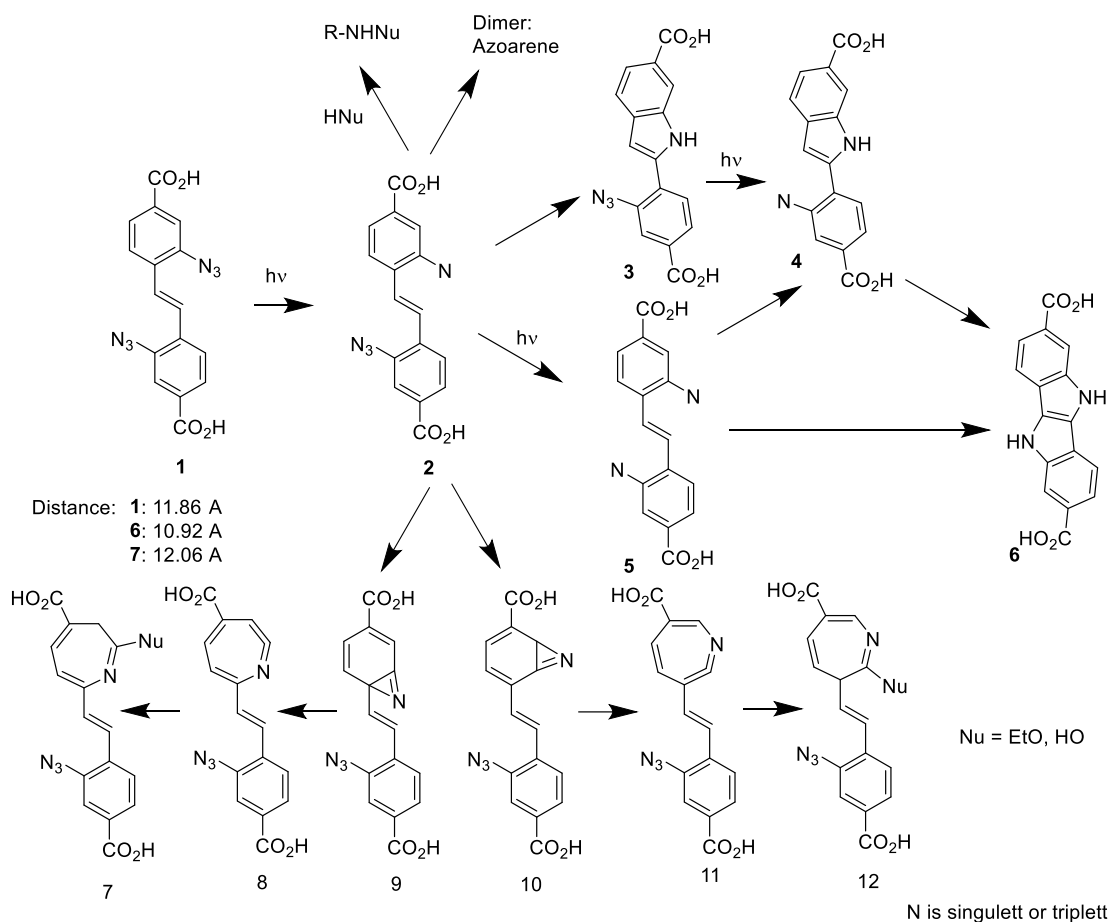


Figure 3.13 Rationale for the irradiation of azide 1 – the metal nodes were omitted for clarity.

After the reactions for each solvent different new sets of IR bands were observed (**Figure 3.14**). However, the effect of the solvent is not limited to yielding different products originating from the reaction of the intermediate nitrene with different molecules, but also the initial photolysis of azide to form nitrene is affected. This is evidenced by the inset in Figure 4, which shows that the intensity decreases of the azide band at 2129 cm^{-1} is much slower in heptane and cyclohexane than in UHV (and the other solvents). The origin of the decrease is currently unclear, it might be a combination of light absorption effects and van der Waals effects between the solvent and the nonpolar azide moiety. Certainly, the products are different, e.g. inter- and intramolecular CH activation or ring expansion to yield azepinones.

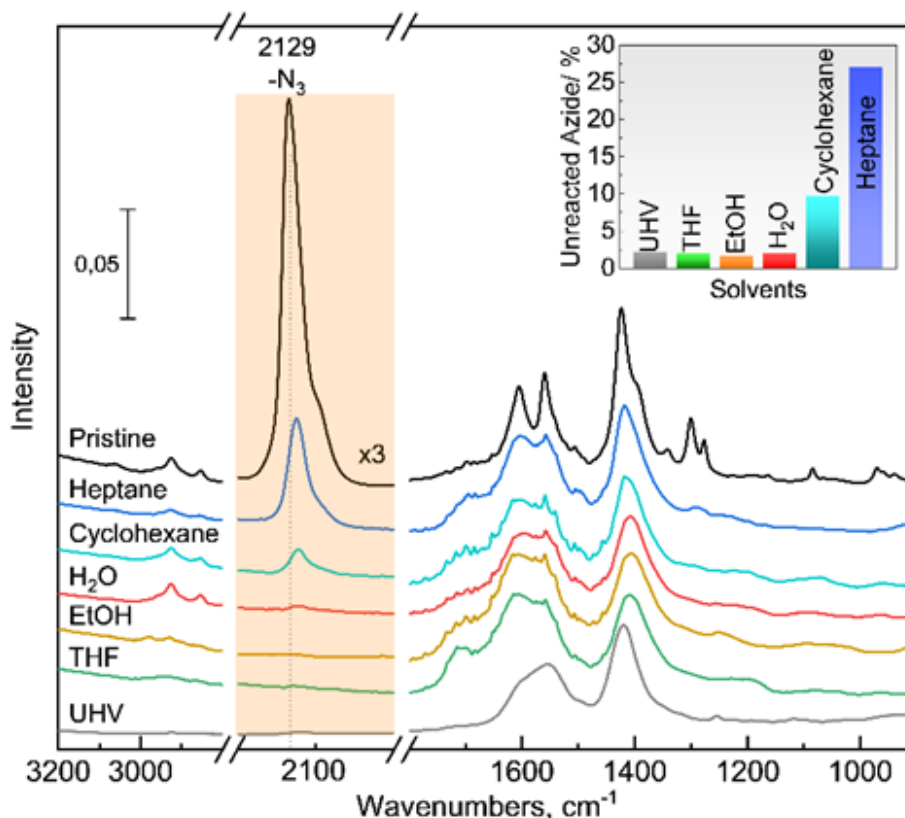


Figure 3.14 Comparison of azide photolysis in UHV and solvents. IRRAS data of azide-SURMOFs after UV illumination (254 nm) at 298 K for 50 min in UHV and various solvents including H₂O, tetrahydrofuran (THF), ethanol (EtOH), cyclohexane, and heptane. The inset shows the concentration of remaining azide based on a quantitative analysis of the azide (N₃) band intensity at 2129 cm⁻¹.

3.4 Conclusions

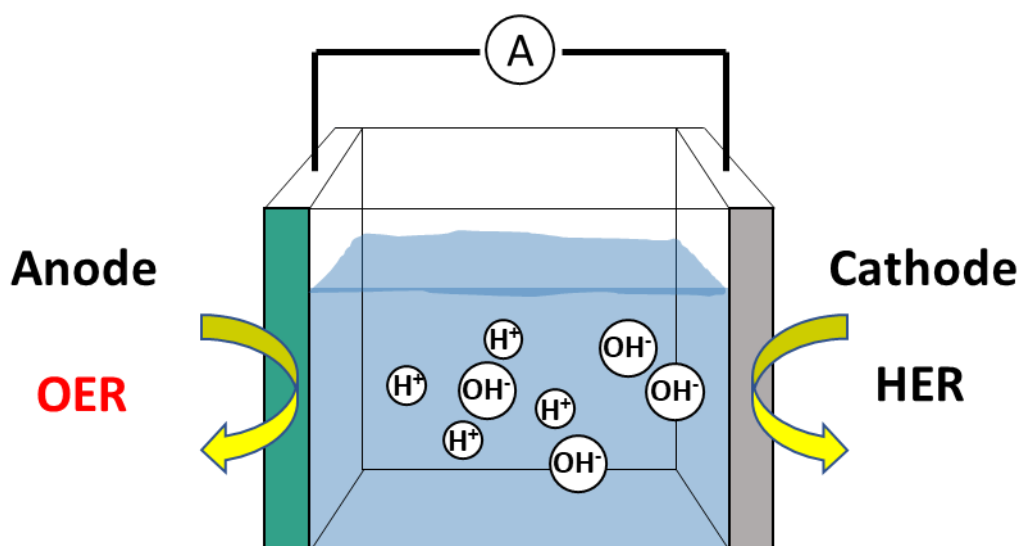
In summary, we have established a solvent-free model system using a porous, crystalline surface-mounted MOF thin film (SURMOF) as an ideal matrix. The crystalline structure could work as scaffold where photoactivation happens, in which linkers of the MOF are targeted as the probe molecule. After the formation of radical nitrene under UV light, addition reaction occurs between the nitrene and C=C double bonds, instead of ring expansion between nitrene and phenyl ring. During this reaction, O₂ and moisture are not involved whenever testing in a.t. or UHV. The mechanism is proposed between the reaction of azide and C=C. It was further evidenced by in situ XRD, XPS and MS. As a result of interplay between addition reaction and lattice strains, the photoactivation reaction proceeds gradually fast then

slowing down. Compared to the traditional methods in solvents or in inert cryogenic solid matrices, the highly ordered and crystalline nature of SURMOFs allows for a thorough study on organic reaction mechanisms. The comprehensive results acquired using a multi-technique approach including in-situ IRRAS, XPD, XPS and mass spectrometer, reveal that the initial photo-mediated formation of highly active nitrene intermediate is followed by an intramolecular amination yielding an indoloindole derivative while eliminating any unwanted solvent effects. This work not only provides a novel strategy for precisely studying azide-related thermal and photoreactions using porous and crystalline MOFs as an ideal matrix but also open up the path for potential applications of MOF-based materials in controllable sensors, adsorption, and separation through azide photolysis-induced pore modifications.

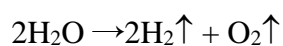
4 MOF-on-MOF Epitaxial Growth of ZIF-67 SURMOF for Electrocatalytic Water Oxidation (OER)

4.1 Introduction

Energy and environment issues are among the most urgent concerns in this era. Searching and applying renewable clean energy, for example hydrogen energy, has been an appealing and promising approach for energy conversion and storage. Electrochemical water splitting provides an efficient way for obtaining hydrogen (Scheme 4.1). In actual practice, water splitting occurs at a much higher potential than the theoretical potential value (1.23 V). This excess potential, referred to as the overpotential, can be minimized by employing the proper electrocatalyst to accelerate reaction kinetics at both electrodes. As one of the half-reaction in water splitting, the oxygen evolution reaction, also known as water oxidation reaction, has been paid special focus. The OER a sluggish process due to the transfer of four protons and electrons, when comparing to the other counterpart reaction HER, or so-called hydrogen evolution reaction. Thus, it is of great importance to develop efficient OER catalysts to overcome the slow kinetic of the OER.



Scheme 4.1 Schematic of the electrochemical water splitting.



In alkaline solutions: OER ($4\text{OH}^- \rightarrow \text{O}_2 + 2\text{H}_2\text{O} + 4\text{e}^-$)

Catalytic OER follows a 4-step process on surface metal sites (M) under alkaline conditions (**Figure 4.1**). Initially, the first 1-electron oxidation of hydroxide anions adsorbed on the active site forms M–OH. Then, M–OH evolves into M–O after a couple of proton and electron removals. Thereafter, M–O converts into M–OOH after a hydroxyl anion gets coupled under 1-electron oxidation and then starts another proton-coupled electron transfer process, generating O₂ and the initial active sites.[181, 182]

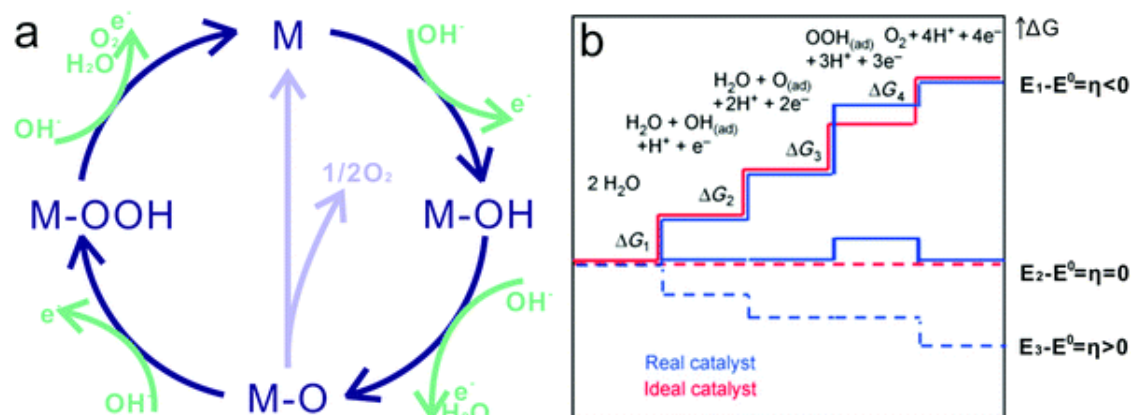


Figure 4.1 (a) The catalytic reaction mechanism of OER under alkaline conditions. (b) Gibbs free energy of reactive species and intermediates in each step of the OER mechanism.

In OER, the performance of Ir and Ru oxides catalysts are excellent, yet these noble metals are far too expensive. To find a replacement, one would not overlook the great potentials of MOF. With high surface area, diverse composition, and well-defined metal sites and even promoter sites, the porous metal organic frameworks and their derivatives have been widely employed as OER electrocatalysts. The poor stability of most MOF hindered their application in OER. While an unusual case is the cobalt-based Zeolitic imidazolate framework (ZIF-67). It belongs to the imidazole zeolite framework family, also a classic metal organic frameworks.

Zeolitic imidazolate frameworks (ZIFs) are a new subclass of porous metal-organic frameworks (MOFs), often with an extended zeolite topology.[183] ZIF-67 resembles structures of zeolites, wherein Co²⁺ ions replace the position of silicon and 2-methylimidazole substitute oxygen. Metal sites Co²⁺ and linkers 2-methylimidazole connected through the N atoms in the linkers, forming a tetrahedral structure, with the angle of M–Im–M around 145°. The resulting cubic crystal symmetry shows unit cell parameters a ¹/₄ b ¹/₄ c ¹/₄ 16.9589 Å. ZIF-8 is similar to ZIF-67, in which the Co²⁺ ion

is replaced with Zn^{2+} . Also, the cell parameters changed slightly from 16.9589 Å to 16.9910 Å.

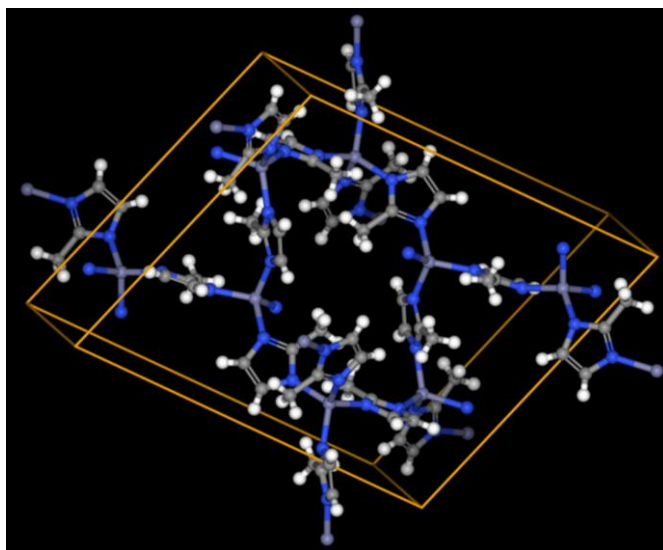


Figure 4.2 Structure of ZIF-67 (purple: Co, white: hydrogen, gray: carbon, blue: nitrogen).

Powder ZIFs have been studied vastly, while the thin films of ZIFs are relatively new area. Elvia was the first one who successfully synthesized the ZIF-8 SURMOF using a lbl fashion.[65] While, to the best of our knowledge, there has been no report of ZIF-67 SURMOF. The heterogeneous catalysis, OER, takes place on the interface between the surface of catalysts and electrolytes. Considering the similar structure characteristic of ZIF-8 and ZIF-67, it is possible to grow ZIF-67 epitaxially on ZIF-8. The typical epitaxial growth process is depositing a crystalline material on the specific crystal face of a crystalline substrate with the same orientation and similar lattice spacings.[184] To date, epitaxial growth has been one of the most widely applied strategy for the synthesis of MOF-on-MOF hybrids. It was also verified from the core-shell ZIF-8@ZIF-67 structure[185]. Here, for the first time, we have fabricated the ZIF-67 SURMOF via a simple MOF-on-MOF epitaxial method.

4.2 Experimental

4.2.1 Synthesis of ZIF-67 SURMOF

- 1) Prepare of SAMs on gold substrates.

The 11-mercapto-1-undecanol (MUD, 99%, Aldrich) solution was prepared by dissolving MUD in ethanol (VWR) to reach the desired concentration of 1 mM. A

clean gold substrate was placed in this solution for 24 h and then rinsed with the pure solvent and gently dried under nitrogen flux.

2) Prepare of ZIF-8 SURMOF.

Using a dipping robot operating at ambient temperature and pressure, the gold substrate was sequentially immersed in the methanolic and rinsing solutions in the following order for given circles:

1. Metal source: 10 mM zinc dinitrate hexahydrate 98% (Alfa Aesar) solution for 300 s
2. Rinsing step: pure methanol (Merck seccosolv) for 100 s
3. Linker source: 20 mM 2-methyl-1H-imidazole (Merck) for 300 s
4. Rinsing step: pure methanol (Merck seccosolv) for 100 s

3) Prepare of ZIF-67 SURMOF.

The preparation of ZIF-67 SURMOF follows a similar method to ZIF-8 SURMOF, but with the ZIF-8 SURMOF as the substrate.

1. Metal source: 10 mM cobalt dinitrate hexahydrate 98% (Alfa Aesar) solution for 300 s
2. Rinsing step: pure methanol (Merck seccosolv) for 100 s
3. Linker source: 20 mM 2-methyl-1H-imidazole (Merck) for 300 s
4. Rinsing step: pure methanol (Merck seccosolv) for 100 s

4) Doping B and Ni in ZIF-67 SURMOF.

ZIF-67 SURMOF is immersed in a 0.1M Ni (NO₃)₂·6H₂O solution. The pH then adjusted to 8 using the 0.1M KOH solution. 0.1M NaBH₄ solution is added afterwards.

4.2.2 Catalytic performance tests

The as received ZIF-67 SURMOF was cut in proper form for the tests of OER. A three-electrodes cell (**Figure 4.3**) was applied for the water splitting, with Pt foil as

the counter electrode, Ag/AgCl as the reference electrode and SURMOF as the working electrode. The water splitting reaction was then performed under atmosphere in a 1M KOH aqueous solution, with pH=14. An Ivium potentialstat was connected to these three electrodes for detecting current and voltage. Potential recorded against these RE are converted to RHE by using a simplified form of the Nernst equation (eq):

$$E_{\text{RHE}} = E_{\text{Obs}} + E_{\text{RE}}^0 + (0.0592 \times \text{pH})$$

where E_{RHE} , E_{Obs} , and E_{RE}^0 are potential recorded against RHE, observed potential against RE, and standard electrode potential of the RE.

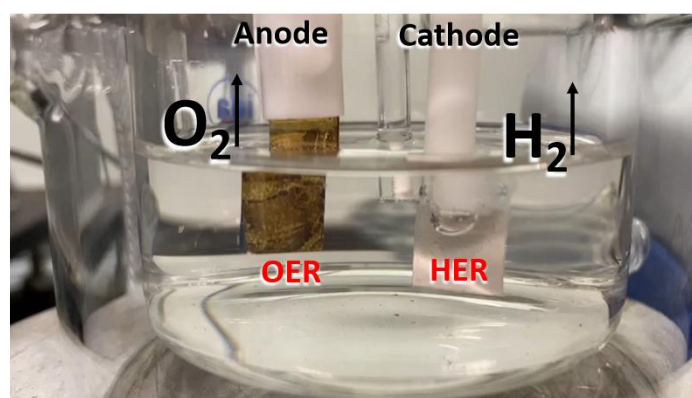


Figure 4.3 Electrochemical cell for OER performance tests.

4.3 Results and discussion

4.3.1 ZIF-67 SURMOF before OER

The ZIF-67 SURMOF shows a sharp peak at 7.8° in the XRD pattern (**Figure 4.4**). The simulated curves according to material studio software also confirms the successful synthesis of ZIF-67. Yet there are some differences. As the SURMOF is oriented, it only shows obvious diffraction peak in the first order. Unlike the MOF powders, in which multiple diffraction peaks are contributed from different orientations, it is hard to collect signals from all facets. For the other facets in the thin film, the signals are too weak to detect. It is similar with the ZIF-8 SURMOF deposited on an Au-coated Al_2O_3 substrate.[65]

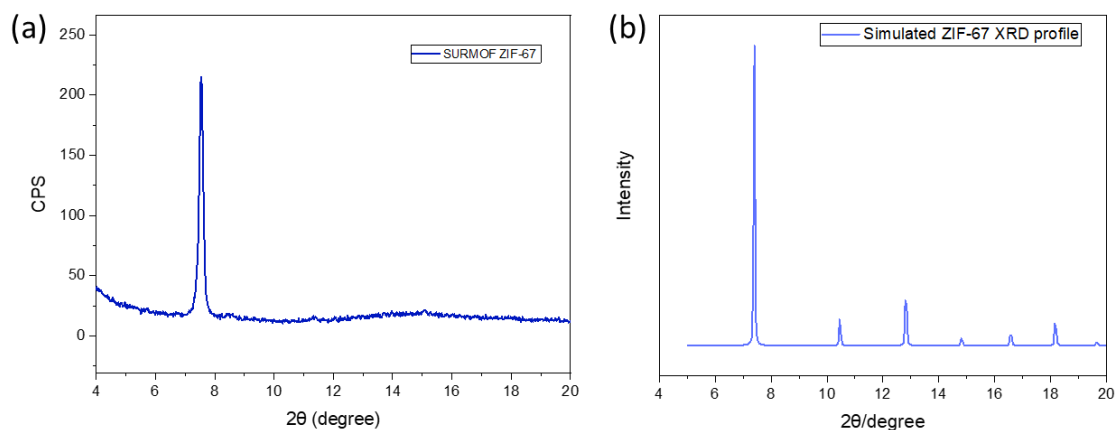


Figure 4.4 a) XRD patterns of SURMOF ZIF-67. b) Simulated XRD patterns of ZIF-67 powders.

The Raman spectra further verifies the exists of ZIF-67 (**Figure 4.5**). Raman shift at around $150\text{-}200\text{ cm}^{-1}$ presents the vibration of N-Co-N bonding.[186] This is the characteristic vibration of ZIF-67. Vibrations from the organic linkers are shown at around $250\text{-}300\text{ cm}^{-1}$ and $650\text{-}700\text{ cm}^{-1}$ as the C-CH₃ vibrations.[186] The inserted figure is the picture shot from the Raman microscopy. It shows a similar pink color according to the macroscopic image we describe above. Representative three points, labelled A, B and C, are tested though the Raman apparatus. As is shown, all 3 curves are similar which hints the homogeneous dispersion.

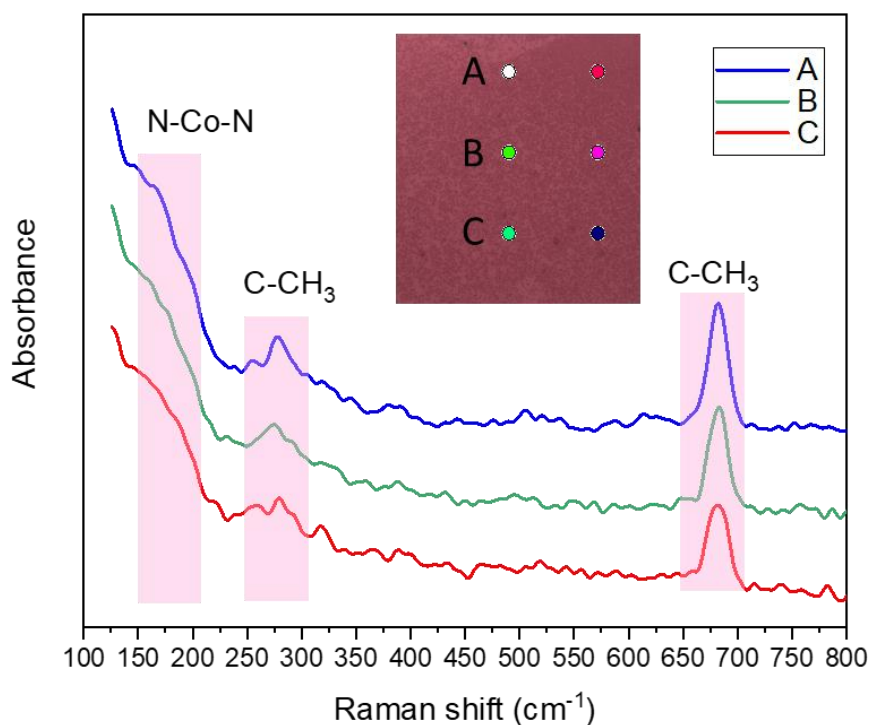


Figure 4.5 Raman spectra of SURMOF ZIF-67.

Besides, high resolution IRRAS spectra provides detailed structure information (**Figure 4.6**). The IRRAS is operated under a UHV chamber at 118K. The IR spectra of ZIF-67 SURMOF is similar to reported ZIF-67 powders.[186] Higher wavenumbers at 3134 cm^{-1} shows the $=\text{C-H}$ stretching. C-H symmetric stretching from a sp^3 orbital is located at $2927\text{-}3000 \text{ cm}^{-1}$. Lower wavenumbers area contain more information. C=N stretching and C=C stretching lead to vibrations at 1585 cm^{-1} and 1463 cm^{-1} , respectively. CH_2 , CH_3 antisymmetric bend appear at 1423 cm^{-1} and 1384 cm^{-1} . At 1313 cm^{-1} shows the CH_2 wagging. For the $=\text{C-H}$ in plane deformations, 1147 cm^{-1} and 1184 cm^{-1} are presented. Due to the imidazole ring, C-N vibration inside shows at 1055 cm^{-1} and $=\text{C-H}$ in plane bends at 995 cm^{-1} .

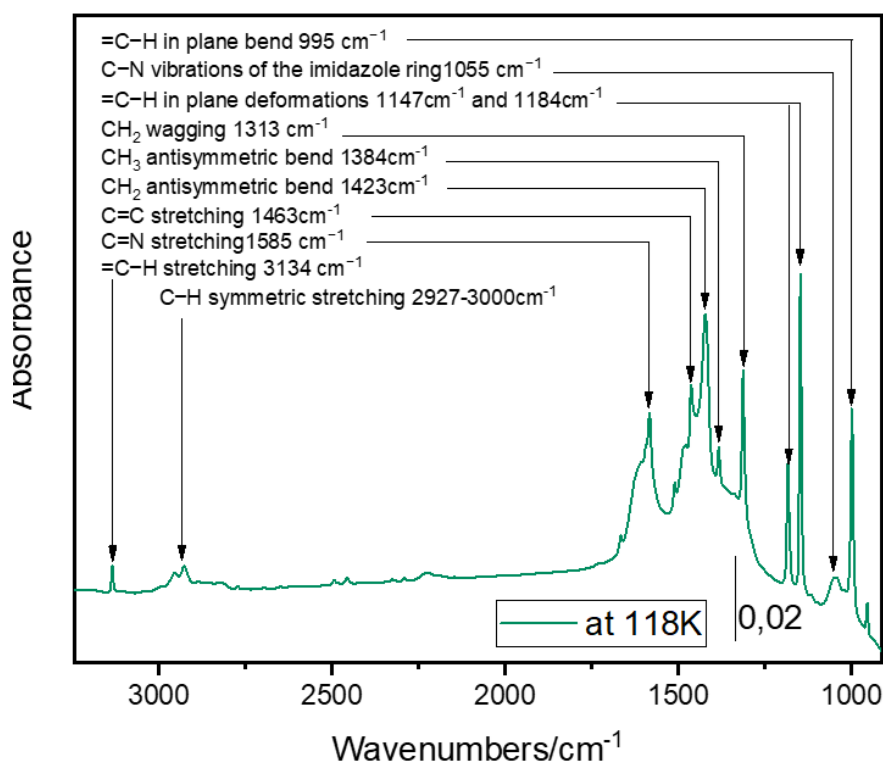


Figure 4.6 UHV-IRRAS of SURMOF ZIF-67.

During the synthesis and subsequent treatments, it is often that MOF is born with defects inside the structure, missing of linkers or metal sites. In this regard, CO probe molecular is dosed to the ZIF-67 surface (**Figure 4.7**). It turns out that no detectable CO vibration is present in the IRRAS. This means not adequate Co²⁺ sites available in the ZIF-67 SURMOF. It hints that this is a high-quality MOF thin film with low density of defects.

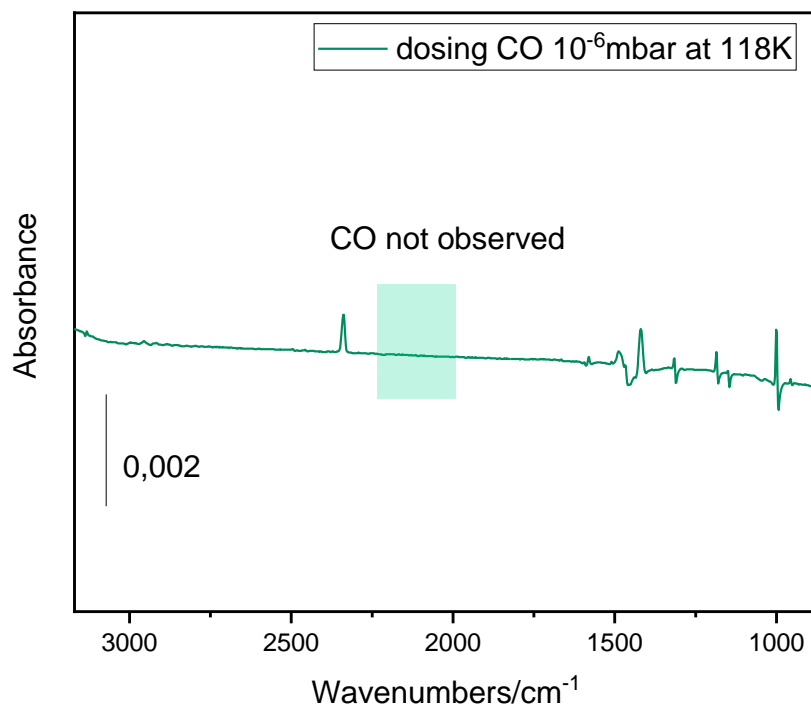


Figure 4.7 UHV-IRRAS of CO probing on SURMOF ZIF-67.

To investigate the morphology AFM images are obtained. As is shown in **Figure 4.8**, the ZIF-67 SURMOF presents uniform planar surface. To gain information of the thickness, the thin film was scratched carefully with cotton sticks then observed with the AFM. The mean thickness of the ZIF-67 thin film is around 100 nm. The thin film consists of 100 cycles ZIF-8 and another 100 cycles ZIF-67, which makes 200 cycles. ZIF-8 and ZIF-67 share with the similar crystal parameters. Provided in each cycle growth one single layer of ZIF-8 or ZIF-67, every layer is as thick as around 0.5 nm.

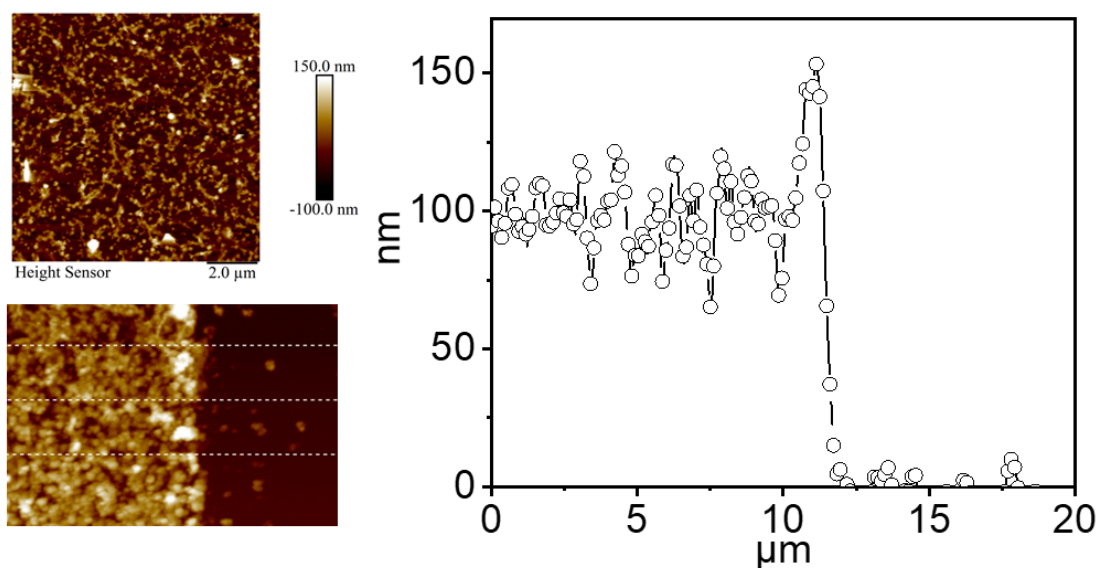


Figure 4.8 AFM images of SURMOF ZIF-67.

Chemical states of each elements of ZIF-67 SURMOF were also revealed by the XPS (**Figure 4.9**). For Co 2p orbitals, 2p $\frac{1}{2}$ and 2p $\frac{3}{2}$ are shown at 797.2 eV and 781.3 eV, with a 15.9 eV difference.[187, 188] Strong satellite peaks at 803.1 eV and 785.9 eV are shown.[187] This implies Co^{2+} is the main state of cobalt elements in ZIF-67 SURMOF.

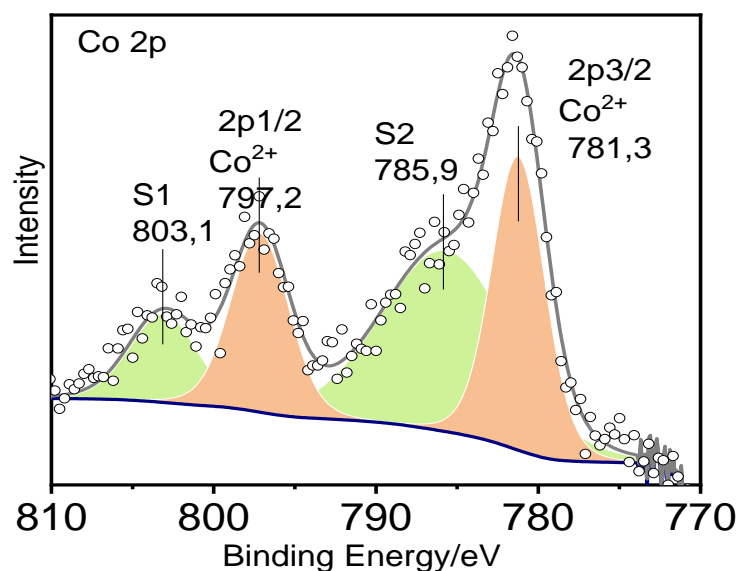


Figure 4.9 XPS Co 2p orbitals of SURMOF ZIF-67.

4.3.2 Evolution of active sites during OER

Working electrode ZIF-67 SURMOF was set as the anode to test the OER performance in electrical water splitting reaction. As is shown in the LSV results (**Figure 4.10**), the ZIF-67 shows an onset voltage at 1.5V. Its overpotential at 10 mA/cm² reaches 468mV. This is comparable to most powder ZIF-67 catalysts. For comparison, a bare gold substrate was tested. The gold shows inert performance in catalyzing the OER. Its onset voltage reaches 2.1V, accompanied with its overpotential at 10 mA/cm² reaches 1063mV.

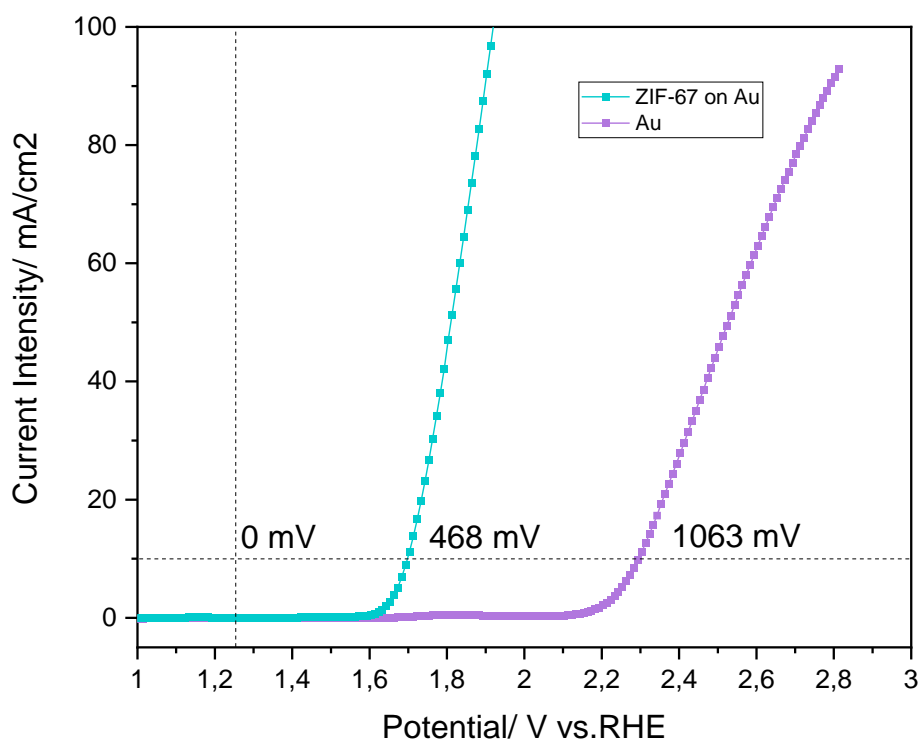


Figure 4.10 LSV of SURMOF ZIF-67.

After OER tests, there are structural changes taken place inside the ZIF-67. According to the AFM images (**Figure 4.11**), it is noticed that the thickness has been decreased from 100 nm to 20nm, while its homogeneous and planar morphology maintained.

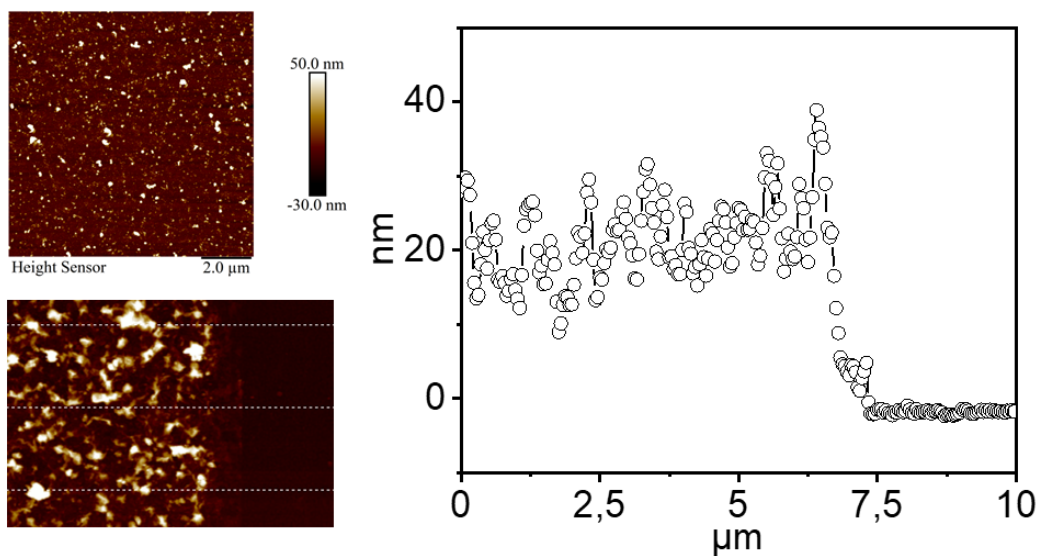


Figure 4.11 AFM images of SURMOF ZIF-67 after OER measurements.

From the Raman spectra, sharp different curves appear (**Figure 4.12**). The N-Co-N vibration at $150\text{-}200\text{ cm}^{-1}$, as well as the C-CH₃ vibrations at $250\text{-}300\text{ cm}^{-1}$ and $650\text{-}700\text{ cm}^{-1}$ disappeared. Instead, the other cobalt species exist. At 504 cm^{-1} and 635 cm^{-1} show the beta Co(OH)₂ and alfa Co(OH)₂. [187] These cobalt hydroxides are reported as active site in OER. Looking at the inserted photo, the color of it changed from a pink one to a black one. Also, it is observed that the minor pinholes exist, which may generate as a result of O₂ bubble.

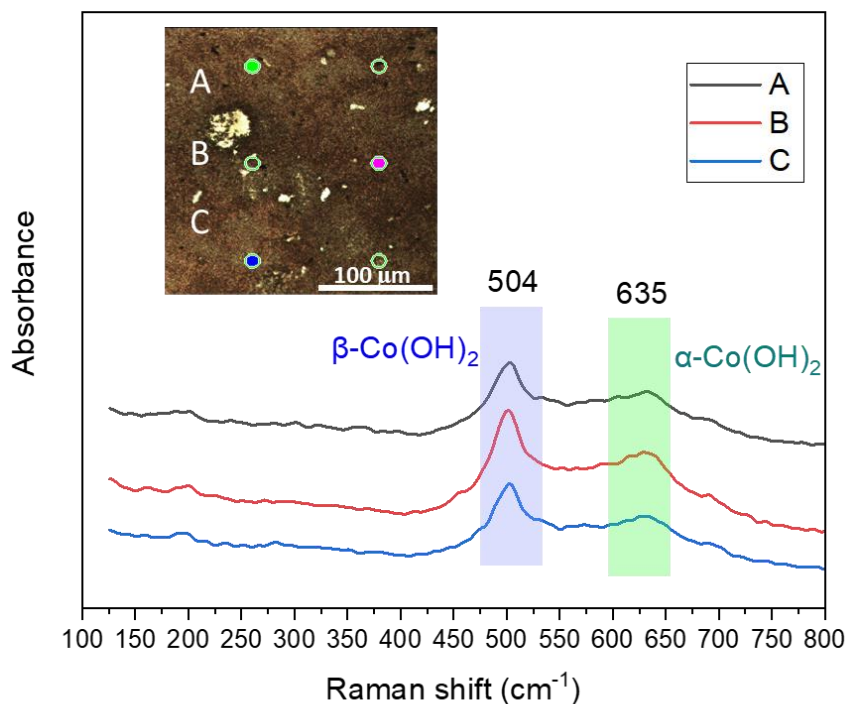


Figure 4.12 Raman spectra of SURMOF ZIF-67 after OER measurements.

Enlarged LSV(**Figure 4.13**) provides supporting information concerning the evolution of active sites. There are two minor peaks before the OER reaction taking place. The first one at around 1.15 V can be explained by the oxidation of Co^{2+} to Co^{3+} . The second one at around 1.45 V can be regarded as the further oxidation of Co^{2+} . The second peak shows an antisymmetric shape. It is a consequence of contribution of the onset OER current. This also hints that the onset potential is around 1.5 V.

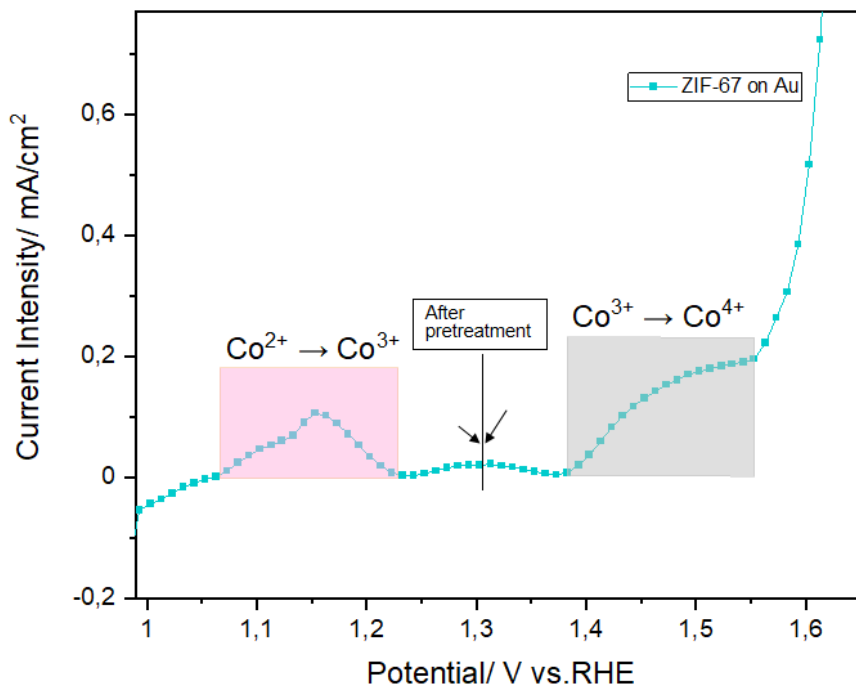


Figure 4.13 Enlarged LSV of SURMOF ZIF-67.

Stopped at 1.3 V during OER test, labelled as after pretreatment, the sample was tested for the XPS. Different from the pristine ZIF-67 SURMOF, the Co 2p orbitals can be decoupled into 3 peaks with an additional Co^{3+} one (**Figure 4.14b**). The Co^{3+} with 2p $\frac{1}{2}$ at 794.8 eV and 2p $\frac{3}{2}$ at 779.5eV is lower in the binding energy than the Co^{2+} .^[187] Satellite peaks of Co 2p becomes weaker, which implies the decrease of Co^{2+} proportion. The O1s orbital has also witnessed its change (**Figure 4.14e**). The O1s peak of the pristine sample is located at 531.4eV. After treated with the 1.3V current, the O 1s orbital decreased its main peak to 530.7eV with a small peak at 528.7eV. The peak at 528.7eV comes from the oxyhydroxides oxygen species. With even higher voltage at 2.2 V when OER goes on with heavily bubbles, the XPS was also collected. To this end, further more Co^{3+} proportion in Co 2p was observed (**Figure 4.14c**). Also, new O 1s species at 528.5 eV strengthened its percentage (**Figure 4.14f**). Noteworthy, the XRD pattern of the SURMOF ZIF-67 (**Figure 4.15**) shows no diffraction peaks after the OER performance tests. This indicates Co^{2+} metal sites in the ZIF-67 SURMOF evolved into amorphous CoOOH species (**Figure 4.16**).^[187, 189]

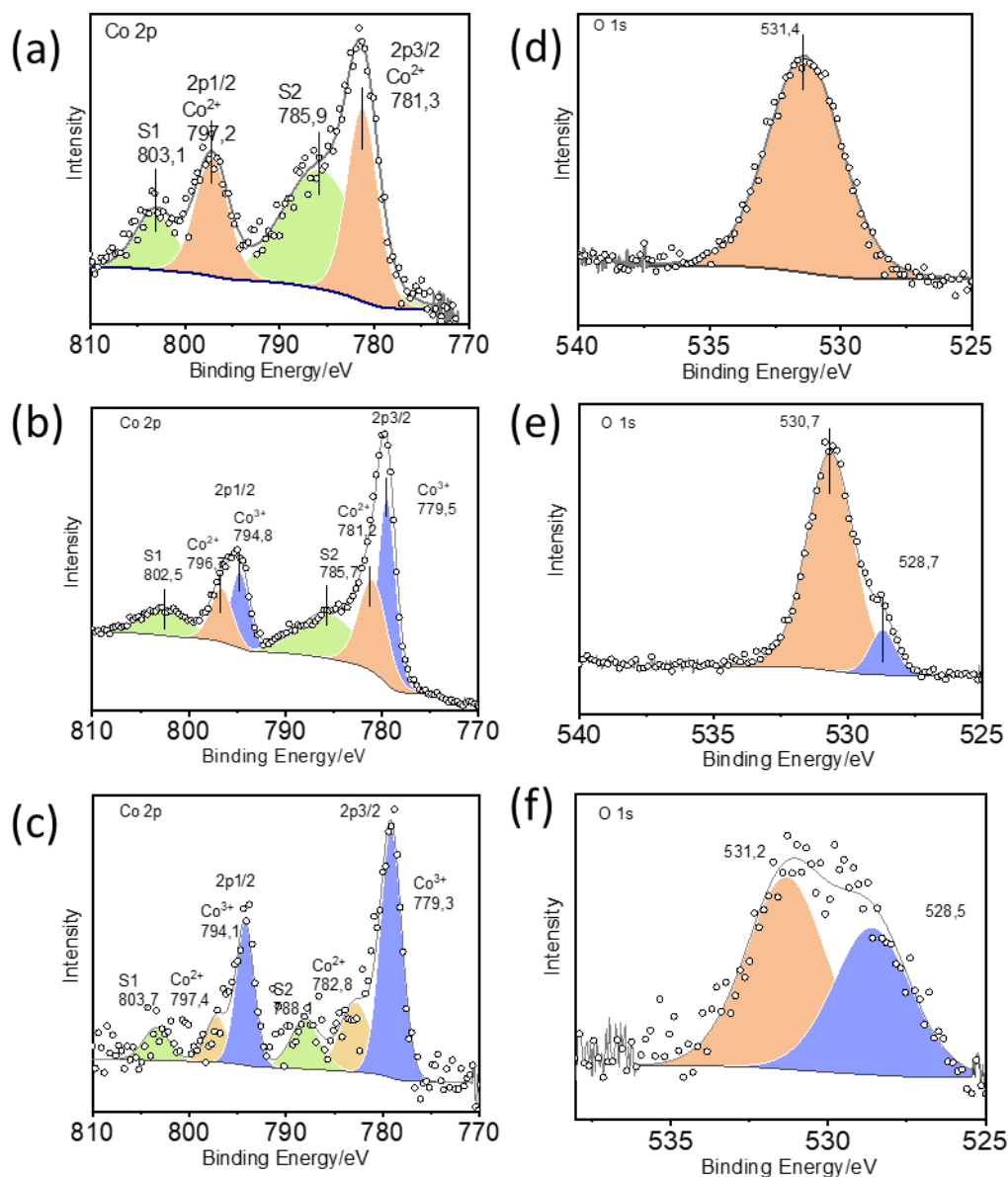


Figure 4.14 a) Co 2p orbital of pristine SURMOF ZIF-67. b) Co 2p orbital of SURMOF ZIF-67 treated with 1.3V. c) Co 2p orbital of SURMOF ZIF-67 after OER measurements. d) O 1s orbital of pristine SURMOF ZIF-67. e) O 1s orbital of SURMOF ZIF-67 treated with 1.3V. f) O 1s orbital of SURMOF ZIF-67 after OER measurements.

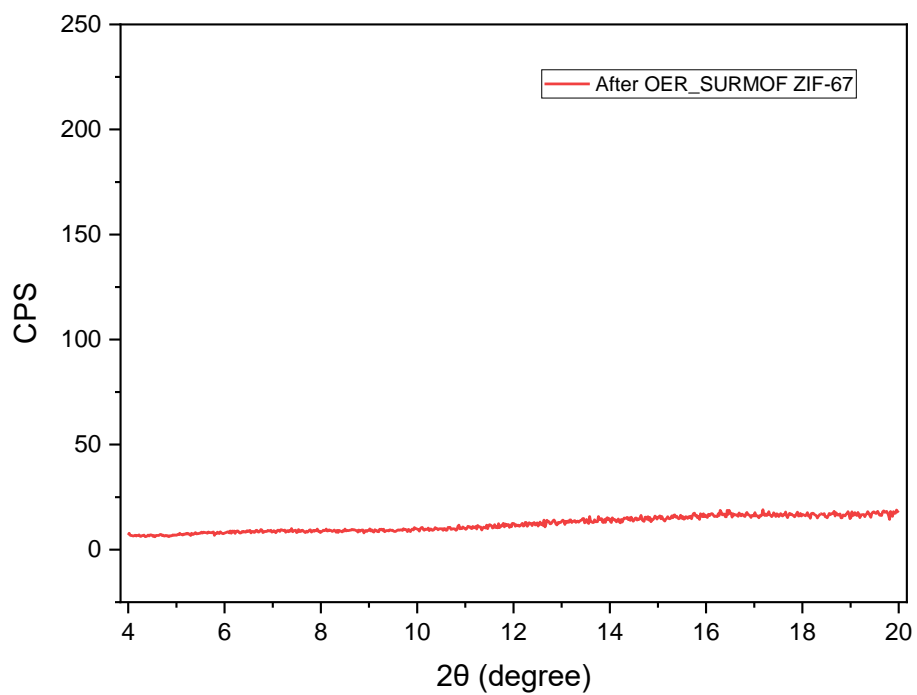


Figure 4.15 XRD patterns of SURMOF ZIF-67 after OER performance tests.

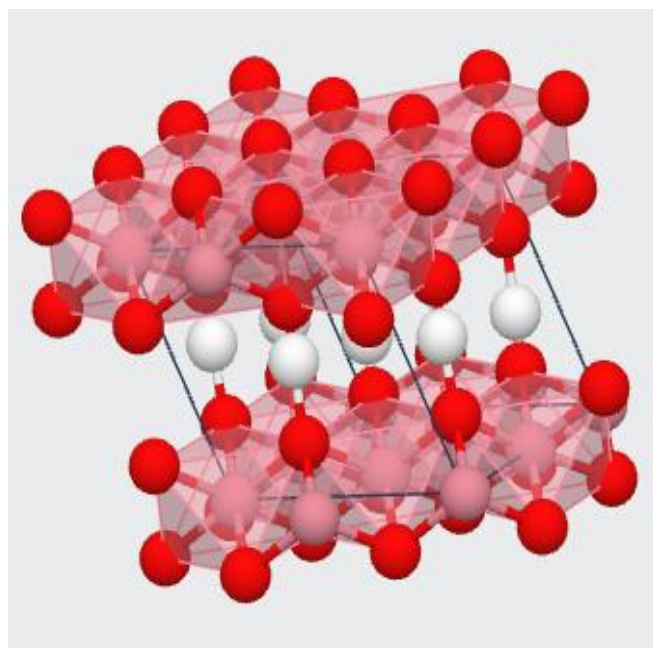


Figure 4.16 Structure of CoOOH species. (red: Cobalt, white: hydrogen, gray: oxygen).

4.3.3 Doping strategy for improving catalytic performance

Doping is a conventional strategy for optimizing the OER performance in cobalt based catalysts.[190] There are anion and cation doping solutions. Anionic regulation adjusts the electronic structure of the cationic active site through the anion environment of the transition metal compound. The modified electronic interaction between the cation and newly introduced anion can effectively improve the catalytic activity. In cationic modification, via doping with various metal ions the electronic structure and the adsorption of intermediates can be optimized herein.

Ni was doped into the ZIF-67 SURMOF via a precipitation-deposition method. Through the LSV (**Figure 4.17**), the OER performance remains almost unchanged after the Ni doping. Boron as the cation additive was introduced via treating the ZIF-67 SURMOF with NaBH_4 . The overpotential reduced to 430mV after the boron incorporation. While combining both boron and Ni, a synergetic phenomenon was appearing. A drastic reduction of overpotential was observed. The overpotential was reduced to 375mV, ~100mV lower than the unmodified ZIF-67 SURMOF. This result verifies that the conventional methods for enhancing OER performance in powder MOFs can be also transformed into the SURMOF system.

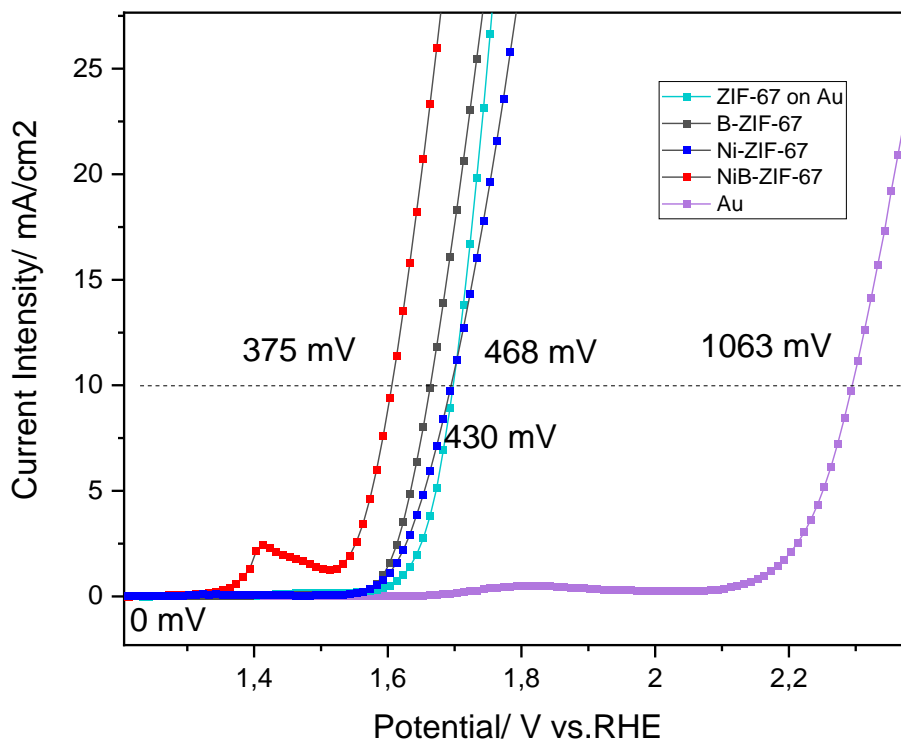


Figure 4.17 LSV of SURMOF ZIF-67 after doping with B and Ni.

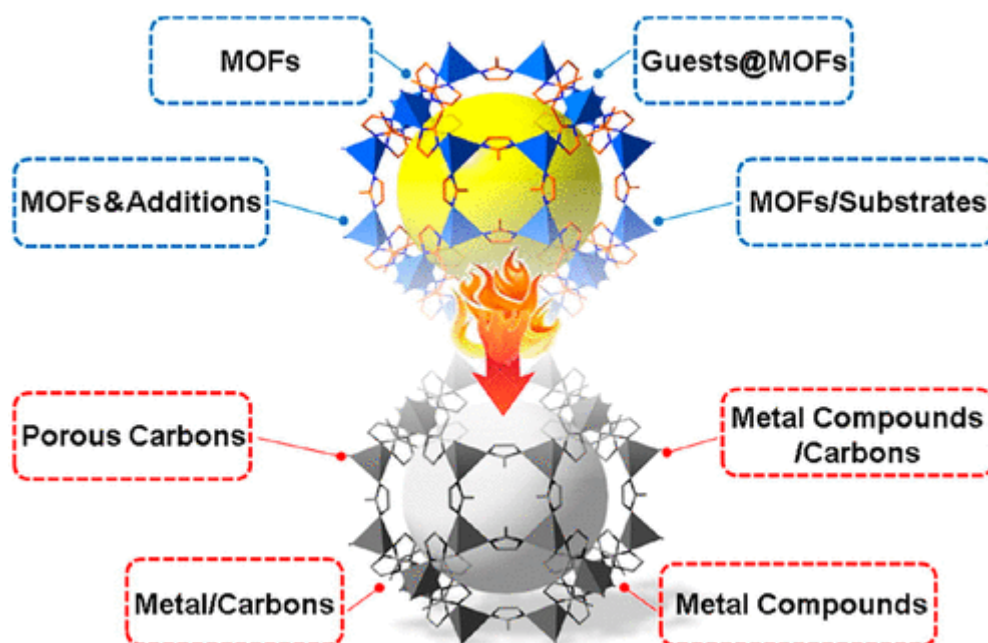
4.4 Conclusions

In conclusion, high quality ZIF-67 SURMOF was fabricated via a liquid phase layer-by-layer fashion and employed in OER for the first time. An overpotential of 468 mV at 10 mA/cm² was reached when using ZIF-67 SURMOF as OER catalysts. The structural and electronic evolution of Co species and active sites were revealed. During the OER test, the structure of ZIF-67 SURMOF was evolved into CoOOH species, whereas the organic linkers in the pristine ZIF-67 SURMOF was destroyed. Further, Ni and B doping was applied to optimize the OER performance. With Ni and B additives, the overpotential decreased to 375 mV.

5 Thermolysis of ZIF-67 SURMOF

5.1 Introduction

Aside from the catalytic applications in the last chapter, MOFs are also commonly used as precursors to prepare carbon- or metal-based or composite nanomaterials for energy and environmental applications.[191] The pyrolysis of MOF-nanoparticle composites forms highly porous, N- or P-doped, graphitized MOF-derived nanomaterials, which are increasingly used as efficient catalysts, especially in electrocatalysis and photocatalysis (**Scheme 5.1**).[192] ZIF-67 as a thermal stable MOF shows promising application in catalysis, adsorption, sensors and separations. After a high temperature pyrolysis treatment, Co-NC based carbon materials are generated from the ZIF-67, which achieved vast application in electrocatalysis such as HER, ORR and CO₂RR. Thus, it's important to understand how the structure and species evolution.



Scheme 5.1 Fabrication of Numerous Porous Materials from MOFs and MOF-Based Composites through Pyrolysis. Copy from Ref [193].

Xu et al., studied the thermolysis of ZIF-8 and ZIF-67 powders in air, and found that ZIF-8 experiences deformation around 300 °C, and it slowly collapses from 350 to 550 °C.[194] ZIF-67 rapidly collapses at 300 °C. And in their work, ZIF-67 was transformed into Co₃O₄ instead of Co-NC materials. More frequently, ZIFs were heated under inert gas flow to generate carbon framework materials. Using surface science techniques. Lauren Benz et al., studied the CO₂ and H₂O Adsorption on

ZIF-8 Films.[193] They revealed the difference between a molecule (H_2O) that adsorbs to the outer nanoparticle surfaces and a molecule (CO_2) which diffuses into the pores of ZIF-8 films and quantify uptake of CO_2 by the film.

Thermolysis of a MOF is a complicated process, which needs a more suitable platform to investigate the mechanism. The surface mounted metal organic frameworks, a monolithic MOF thin films with low defect density, are ideally suitable for surface science research like the single crystal. We have proved the successful synthesis of ZIF-67 SURMOF on gold substrates via an epitaxial growth fashion in liquid phase in the last chapter. Combined with surface science technics such as quasi in situ XPS, NEXAFS and UHV-IR, we are able to show here the structural transition of pristine ZIF-67 to Co-NC materials under thermal treatment. Benefited from UHV environment, the chance that reaction between ZIF-67 and O_2 or H_2O are eliminated. So, we can have a clearer view of point. These results reveal the gradually dehydrogenation of linker imidazole, followed by the reconstruction of Co metal ions and changing of its coordination environment.

5.2 Experimental

The synthesis of ZIF-67 SURMOF samples are same to Chapter 4. For the pyrolysis experiments, the ZIF-67 samples are heated in the UHV-IRRAS chamber as described in Chapter 2. Before the pyrolysis of samples, IR backgrounds at different temperatures were collected using perdeuterated hexadecanethiol-SAMs on Au/Si as reference measurements. The details of XPS and NEXAFS measurements can be also found in Chapter 2.

5.3 Results and discussion

5.3.1 In situ pyrolysis of ZIF-67 and its IRRAS

The ZIF-67 SURMOF was heated within a UHV chamber from 300K to 900K. At the same time, IRRAS was recording during the whole pyrolysis. With increasing temperature, several vibration peaks start to vanish as shown in **Figure 5.1**. Characteristic peaks are $=\text{C}-\text{H}$ at 3135 cm^{-1} , $\text{C}-\text{H}$ at $2927-3000\text{ cm}^{-1}$, $\text{C}=\text{N}$ at 1585 cm^{-1} and $\text{C}-\text{N}$ at 1055 cm^{-1} . [194] For $=\text{C}-\text{H}$ at 3135 cm^{-1} , its intensity remains almost unchanged till 400K (**Figure 5.2a**). And it maintains above 80% intensity at 500K. Then it decreases drastically. When it comes to 850K, it's totally disappeared. A

similar trend was observed for C=N at 1585 cm^{-1} (**Figure 5.2b**). The intensity starts to decrease fast from 500K till 850K and reaches zero intensity. For C-N at 1055 cm^{-1} , there is a different trend (**Figure 5.3**). It decreases to 40% intensity from 300K to 600K, while at higher temperature an obvious new and giant peak shows up. Till 900K, its intensity reaches 20 times that of 300K. The peak was changing during the pyrolysis. From 300 to 500K, it shifts from 1055 cm^{-1} to 1065 cm^{-1} . It maintains the peak position from 500K to 750K, then it goes to 1074 cm^{-1} at 900K. The changes in intensity and peak position indicate that there is a change of C-N bond.

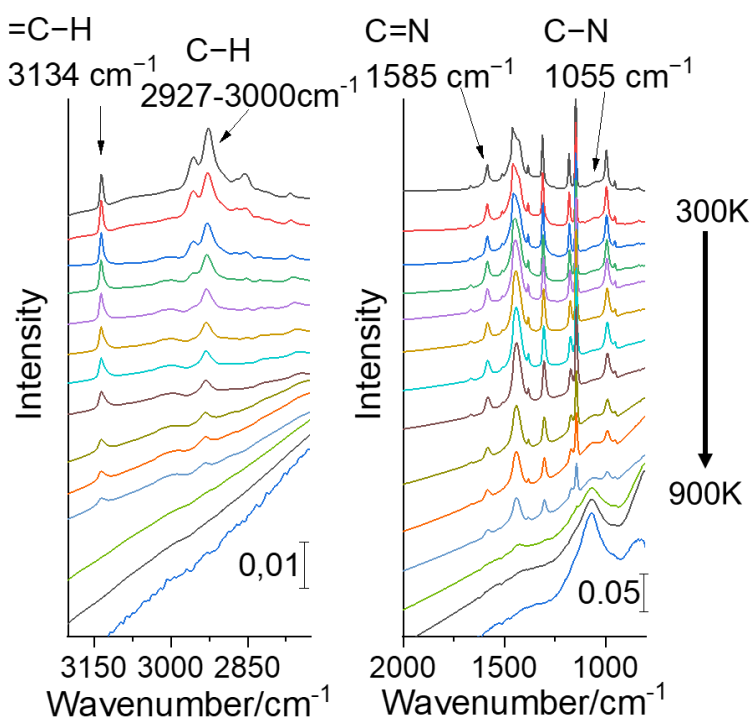


Figure 5.1 In situ IRRAS of SURMOF ZIF-67 thin films under pyrolysis from 300K to 900K in a UHV chamber.

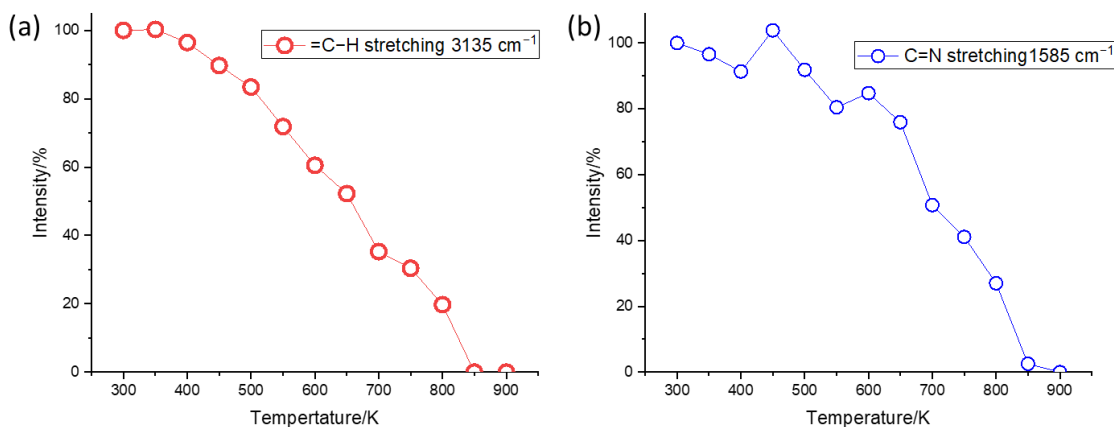


Figure 5.2 Intensity change of a) =C-H at 3135 cm^{-1} and b) C=N at 1585 cm^{-1} .

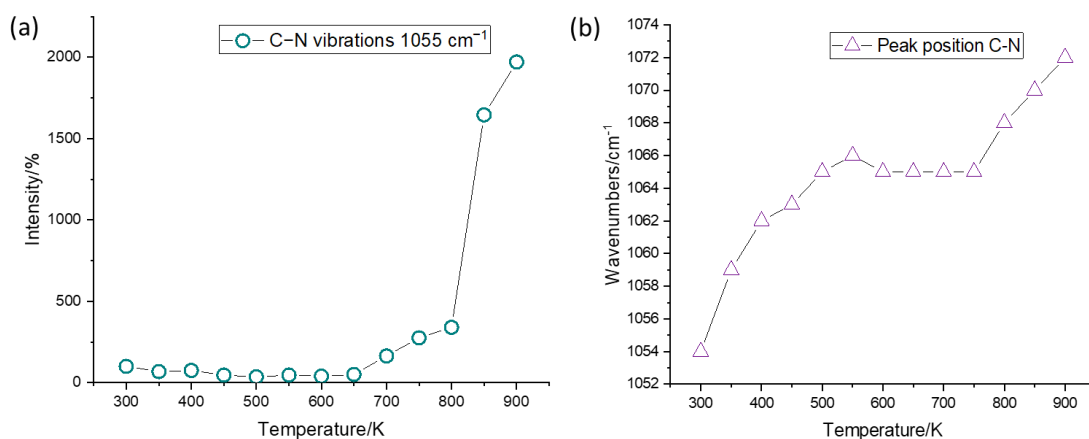


Figure 5.3 a) Intensity change of C-N at 1055 cm^{-1} and b) Wavenumbers change C-N at 1055 cm^{-1} .

5.3.2 Chemical species evolution

The chemical states of ZIF-67 SURMOF during pyrolysis were revealed by quasi in situ XPS. For the pristine ZIF-67 SURMOF, XPS Co 2p spectra were illustrated in chapter 4.3.1. N 1s shows one peak located at 399.4 eV, which shows its pyridinic feature. C 1s shows two main peaks, in which 285.3 eV represents the C atom from the conjugated linker ring and 282.4 eV could come from the surface contamination.

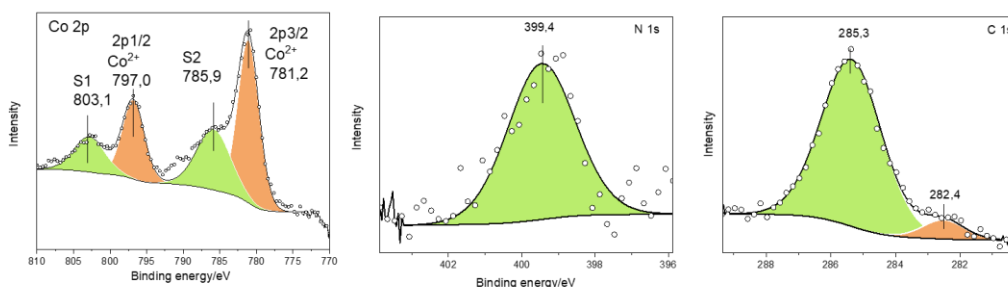


Figure 5.4 Co 2p, N 1s, and C 1s orbitals of pristine ZIF-67 SURMOF at 300K.

When heated to 900K, the sample shows totally different (**Figure 5.5**). For the Co 2p orbitals, the intensity of satellite peaks was decreased. This hints that the Co^{2+} chemical state was changed. An additional individual peak was found at lower binding energy. Considering the pyrolysis was conducted under UHV conditions, the new peak was ascribed to the Co^0 . N 1s was shifted to 398.3 eV and C 1s was shifted to 284.4 eV. This indicates the change of Co, C and N species, which is in accordance to the IR spectra. The above XPS results, confirm that the ZIF-67 SURMOF have been successfully converted into Co- and N-doped graphitic carbons[195].

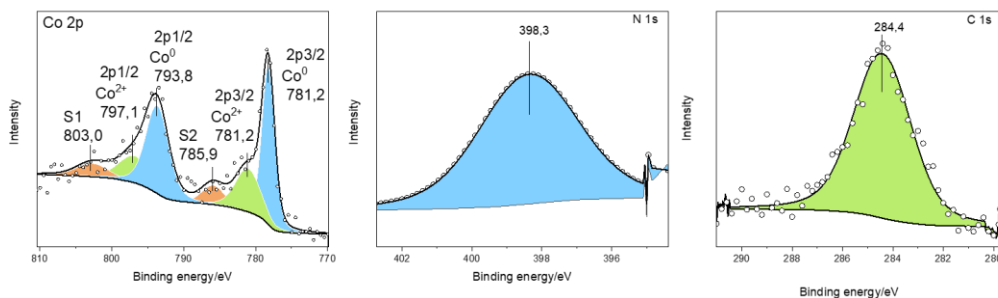


Figure 5.5 Co 2p, N 1s, and C 1s orbitals of pristine ZIF-67 SURMOF after pyrolysis at 900K.

The detailed Co 2p data of the quasi *in situ* XPS is presented in **Figure 5.6**. X-ray grazing angle of 0 degree (**Figure 5.6a**) and 70 degree (**Figure 5.6b**) were applied for the in situ characterization. The results from 0 degree and 70 degree show the similar features. Once the temperature ramped from 300K to 600K, new peaks of Co⁰ at 793.8 and 778.6 eV appear. Then the ratio of Co²⁺/(Co²⁺+Co⁰) decreases as increasing the temperature continuously (**Figure 5.6c**), reaching 30% for both 0 degree and 70 degree observations. This hints that the Co elements have the similar chemical states in both surface and bulk position. Knowing that the thickness of the thin film is about 100 nm, the SURMOF provides an ideal platform for the homogeneous transformation and pyrolysis of ZIF-67. For the powder ZIF-67, the particle size are varied and sometimes reaches μm scales, which hinders the in-depth study of the structure.

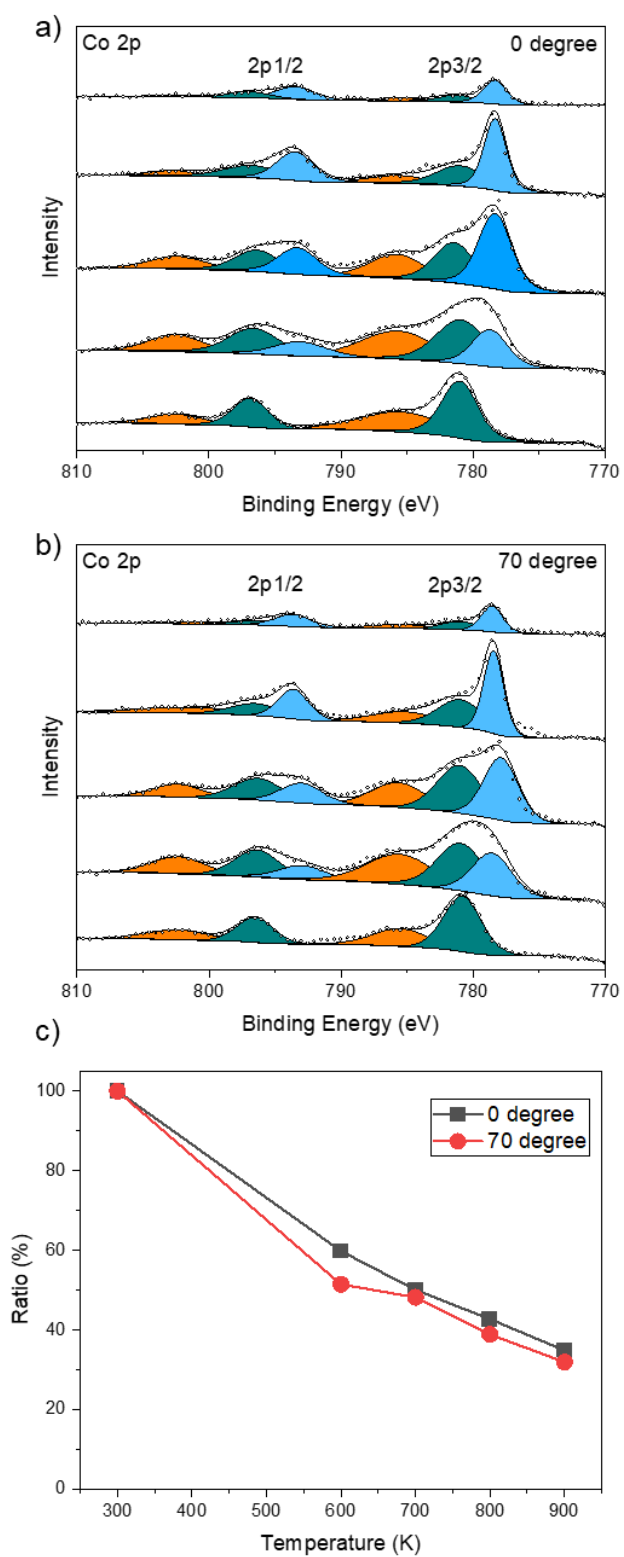


Figure 5.6 Quasi in situ XPS Co 2p data of SURMOF ZIF-67 thin films under pyrolysis from 300K to 900K in a UHV chamber. a) tilt angle 0 degree; b) tilt angle 70 degree; c) Ratio of $\text{Co}^{2+}/(\text{Co}^{2+}+\text{Co}^0)$

NEXAFS spectra of C k-edge and N k-edge were collected to further analysis the evolution of the structure (**Figure 5.7**). For the C K-edge spectrum of fresh SURMOF ZIF-67, the peaks located at 285.1 and 292.5 eV assign to aromatic π^* carbon species and sp^3 hybridized σ^* band, respectively.[196] The resonance shoulder peak at around 287.4 eV originate from the Co-N-C bond.[197] The three peaks at 399.2, 403.3, and 408.9 eV in the N K-edge spectrum of fresh SURMOF ZIF-67 correspond to pyridinic N, graphitic N, and the σ^* C-N bond, respectively. The peak at 390 eV origins from the cobalt. After pyrolysis at 900K, quite different spectra were shown demonstrating a structure change. It is also different when comparing the images before and after the pyrolysis (**Figure 5.8**). For the C K-edge spectrum of SURMOF ZIF-67 after pyrolysis at 900K, it is noticeable that the proportion of σ^* peak gets larger. The N K-edge spectrum shows the decreasing of pyridinic N while the increasing of graphitic N and σ^* C-N. This is agreed with the UHV-IRRAS results, that the C=N double bonds could be destroyed, leaving with σ^* C-N single bonds. The mechanism is illustrated in **Scheme 5.1**.

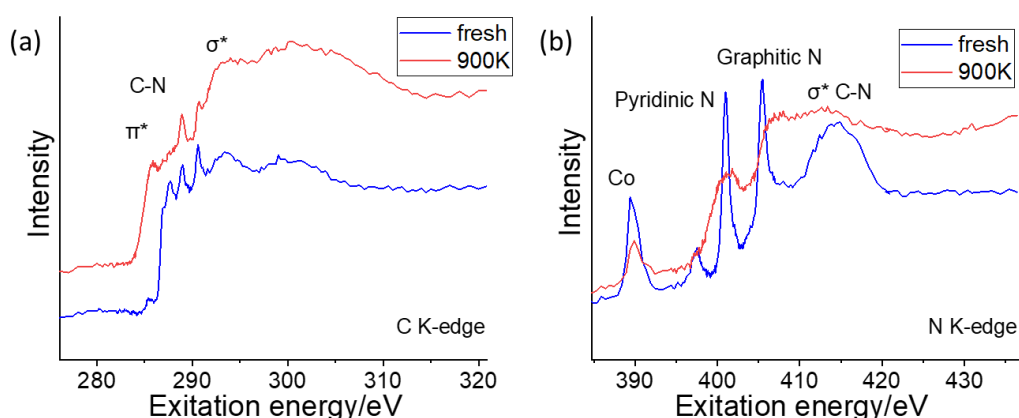


Figure 5.7 NEXAFS spectra of C k-edge and N k-edge of ZIF-67 SURMOF at 300K and after heat treatment at 900K.

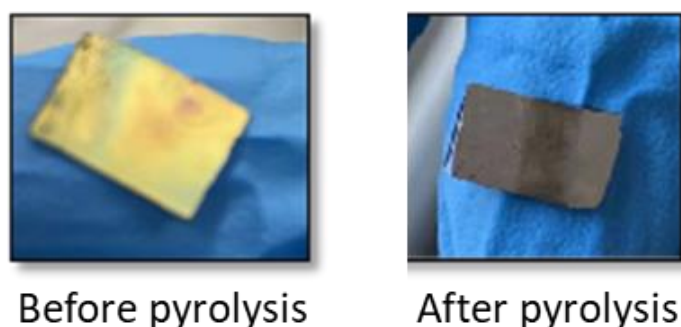
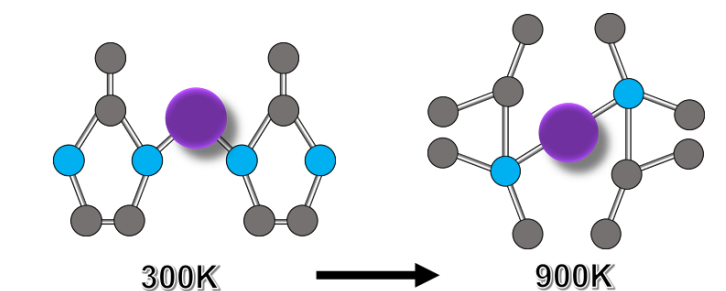


Figure 5.8 Images of SURMOF ZIF-67 samples before and after pyrolysis.



Scheme 5.1 Schematic illustration of SURMOF ZIF-67 after. Blue: nitrogen; Gray: carbon; Purple: cobalt.

5.3 Conclusion

Surface mounted metal organic frameworks thin film (SURMOF) ZIF-67 were fabricated via liquid phase layer-by-layer fashion. In situ IRRAS and XPS were applied to reveal the structural transitions of ZIF-67 to carbon materials with N elements. NEXAFS data shows a final graphitic structure of the carbon materials after pyrolysis at 900 K. Prepared through thermolysis, MOF derived catalysts with metal loaded on carbon materials are promising in energy catalysis, such as OER, HER and ORR. This project could help understand the mechanism during the synthesis of catalysts, thus improve the performance.

6 Summary

In this thesis, SURMOF thin films were studied using surface science technics. The object was to understand the structure and reactivity of SURMOF when served as model platform.

In section 3, we have provided direct evidence for the structural and chemical changes during photoreactions of azide in crystal-stable Cu(Da-SBDC) SURMOFs by applying UHV-IRRAS. The crystalline structure acts as a scaffold where photochemical reactions occur, an addition reaction occurs between the nitrene and adjacent C=C double supported by in situ XRD, XPS, and MS. As a result of the interplay between addition reaction and lattice strains, the photoreaction proceeds gradually faster than slowing down. This work provides a strategy to understand in-depth organic reaction mechanisms without any solvent effect.

In section 4, for the first time, the high quality ZIF-67 SURMOF and its application in OER were reported. The catalytic oxygen evolution reaction (OER), a vital half reaction in the water splitting, is a key process for renewable energy storage and transformation. RuO₂ and IrO₂ are typical OER electrocatalysts, efficient but rather rare and expensive. Non-noble catalysts with high activity, long durability and scalability remains a major challenge. ZIF-67 with non-noble Cobalt ion inside the framework shows promising application in OER. Moreover, the large surface area, tailorable geometry and evenly dispersed active sites of SURMOF ZIF-67 provide enormous potentials. the evolution of Co species and active sites were also preliminarily revealed.

In section 5, the SURMOF ZIF-67 was further studied under elevated temperatures. Through a pyrolysis treatment, ZIF-67 derived materials are very promising catalysts in the energy conversion related reactions. However, the evolution of ZIF-67 in the pyrolysis process remains still unclear. Annealing in UHV chambers, in situ IRRAS, XPS and NEXAFS were applied to uncover the temperature dependent evolution of ZIF-67 from 300K to 900K.

Publication

Jimin Song, Dr. Xiaojuan Yu, Dr. Alexei Nefedov, Dr. Peter G. Weidler, Dr. Sylvian Grosjean, Prof. Dr. Stefan Bräse, Dr. Yuemin Wang, Prof. Dr. Christof Wöll. "Metal-Organic Framework Thin Films as Ideal Matrices for Azide Photolysis in Vacuum." **Angewandte Chemie International Edition** (2023): e202306155.

Conference

1. **Jimin Song**, Xiaojuan Yu, Shuang Chen, Yi Luo, Manuel Tsotsalas, Peter Weidler, Alexei Nefedov, Stefan Heissler, Yuemin Wang, Christof Wöll. Crystal engineering of metal–organic frameworks via topo-photochemical reactions. **ACS Spring 2023, Indianapolis** (oral)
2. **Jimin Song**, Xiaojuan Yu, Manuel Tsotsalas, Shuang Chen, Alexei Nefedov, Stefan Heißler, Yuemin Wang, Christof Wöll. **Bunsen-Tagung 2023, Berlin** (oral)
3. **Jimin Song**, Alexei Nefedov, Stefan Heissler, Christof Wöll, Yuemin Wang. SURMOF ZIF-67 Thin Films for Catalytic Water Oxidation Reaction. **DPG conference 2023, Dresden** (poster)
4. **Jimin Song**, Xiaojuan Yu, Manuel Tsotsalas, Alexander Knebel, Alexei Nefedov, Stefan Heissler, Yuemin Wang, and Christof Wöll. Photoactivation of Azide in SURMOFs. **DPG conference 2022, Regensburg** (oral)

Abbreviation List

UHV	ultra-high vacuum
FTIR	Fourier transform infrared spectroscopy
IRRAS	infrared reflection absorption spectroscopy
XPS	X-ray photoemission spectroscopy
ESCA	electron spectroscopy for chemical analysis
LEED	low energy electron diffraction
HREELS	high resolution electron energy loss spectroscopy
XRD	X-ray diffraction
SXRD	surface X-ray diffraction
TEM	transmission electron microscopy
SEM	scanning electron microscope
STM	scanning tunneling microscopy
TDS	thermal desorption spectroscopy
TPD	thermal programmed desorption
AES	Auger electron spectroscopy
UPS	ultraviolet photoelectron spectroscopy
HAS	He-atom scattering
DFT	density functional theory
MCT	mercury cadmium telluride
InSb	indium stibnite
NIR	near-infrared
MIR	mid-infrared
FIR	far-infrared
TDM	transition dipole moment
SNR	signal-to-noise ratio
KE	kinetic energy
BE	binding energy
NEXAFS	Near-edge X-ray absorption fine structure
UV	ultra-violet

Acknowledgements

Traveling more than 8000 km from China to Germany for my PhD study, now this journey comes to an end as I write here. I would like to express my heartfelt gratitude to the many people who have provided help and support for my doctoral study and this dissertation. My PhD journey wouldn't have been half as meaningful, or possible at all, without these people.

First and foremost, I would like to express my sincere gratitude to Prof. Wöll, for offering me the opportunity working in his group. He is a great role model for the type of leader and scientist I aspire to be. Without his supervision and kind help, technically and intellectually, I could not finish my PhD thesis. He ever told me, "There is still a life after PhD". I am convinced that his school of thoughts has left a remarkable trail on my career path yet to develop.

I am extremely indebted to Dr. Yuemin Wang for his fruitful advice, discussions, and comments on my experiments, manuscripts, and thesis. His expertise about surface science is invaluable. I really admire his rigor and reverence to science. Also in daily life, his love provides me homely warmth.

I want to thank Dr. Alexei Nefedov for his excellent supervision and guidance, great help and thoughtful discussion. With calmness, patience and tolerance, he fixed every problems and created us a wonderful UHV lab. It is quite enjoying for me playing with the "big toy", "THEO" apparatus.

Furthermore, I would like to give my special thanks to the THEO colleagues: Dr. Xiaojuan Yu, Dr. Shuang Chen, Dr. Eric Sauter, Stefan Heißler, Prof. Hicham Idriss and Nils Schewe, who helped me in conducting the lab works, taught me all the details of working on the ultra-high vacuum apparatus and assisted me overcome many technical problems. Thanks to the new THEO members Lachlan Caufield and Zairan Yu for your kindly help.

A sincere thanks also goes to my colleagues of the Institute of Functional Interfaces (IFG) : Dr. Peter Weidler, Dr. Hartmut Gliemann, Dr. Tawheed Hashem, Dr. Manuel Tsotsalas, Dr. Alexander Knebel, Dr. Ritesh Haldar, Dr. Matthias Schwotzer, Dr. Salih Okur, Frank Kirschhöfer, Michael Nusser, Dr. Xiaojing Liu, Dr. Yi Luo, Dr.

Donghui Chen, Peng Qin, Dr. Zejun Zhang, Dr. Chun Li, Yunzhe Jiang, Zhiyun Xu, Yidong Liu, Dr. Abhinav Chandresh, Kuo Zhan, Lena Pilz, Dr. Angela Weiss, Astrid Biedermann, and other members of COOI department, for their energetic willingness to help and invaluable suggestions, and for contributing to such a professional, friendly and pleasant working atmosphere.

Words cannot express my deepest gratitude towards my parents for their endless love and spiritual support throughout the years. I would like to give the fullest credit to my family members, without whose love and support I would not have been able to accomplish so much. Many thanks also to my friends for supporting and helping me in different phases of my life. The hope and encouragement from all of you make up all of my momentum.

Finally, I gratefully acknowledge the China Scholarship Council (CSC) for providing the financial support during my PhD study.

References

- [1] S. Kitagawa, Metal–organic frameworks (MOFs), *Chemical Society Reviews*, 43 (2014) 5415-5418.
- [2] O.M. Yaghi, G. Li, H. Li, Selective binding and removal of guests in a microporous metal–organic framework, *Nature*, 378 (1995) 703-706.
- [3] H.-C. Zhou, J.R. Long, O.M. Yaghi, *Introduction to metal–organic frameworks*, ACS Publications, 2012, pp. 673-674.
- [4] O.M. Yaghi, M. O’Keeffe, N.W. Ockwig, H.K. Chae, M. Eddaoudi, J. Kim, Reticular synthesis and the design of new materials, *Nature*, 423 (2003) 705-714.
- [5] S. Kitagawa, R. Kitaura, S.i. Noro, Functional porous coordination polymers, *Angewandte Chemie International Edition*, 43 (2004) 2334-2375.
- [6] H. Furukawa, K.E. Cordova, M. O’Keeffe, O.M. Yaghi, The chemistry and applications of metal-organic frameworks, *Science*, 341 (2013) 1230444.
- [7] D.J. Tranchemontagne, J.L. Mendoza-Cortés, M. O’keeffe, O.M. Yaghi, Secondary building units, nets and bonding in the chemistry of metal–organic frameworks, *Chemical Society Reviews*, 38 (2009) 1257-1283.
- [8] M. Eddaoudi, D.B. Moler, H. Li, B. Chen, T.M. Reineke, M. O’keeffe, O.M. Yaghi, Modular chemistry: secondary building units as a basis for the design of highly porous and robust metal– organic carboxylate frameworks, *Accounts of chemical research*, 34 (2001) 319-330.
- [9] S.S. Kaye, A. Dailly, O.M. Yaghi, J.R. Long, Impact of preparation and handling on the hydrogen storage properties of Zn₄O (1, 4-benzenedicarboxylate) ₃ (MOF-5), *Journal of the American Chemical Society*, 129 (2007) 14176-14177.
- [10] M.J. Kalmutzki, N. Hanikel, O.M. Yaghi, Secondary building units as the turning point in the development of the reticular chemistry of MOFs, *Science advances*, 4 (2018) eaat9180.
- [11] N. Stock, S. Biswas, Synthesis of metal-organic frameworks (MOFs): routes to various MOF topologies, morphologies, and composites, *Chemical reviews*, 112 (2012) 933-969.
- [12] Y. Luo, S. Bag, O. Zaremba, A. Cierpka, J. Andreo, S. Wuttke, P. Friederich, M. Tsotsalas, MOF synthesis prediction enabled by automatic data mining and machine learning, *Angewandte Chemie International Edition*, 61 (2022) e202200242.

- [13] O. Shekhah, J. Liu, R. Fischer, C. Wöll, MOF thin films: existing and future applications, *Chemical Society Reviews*, 40 (2011) 1081-1106.
- [14] J. Liu, C. Wöll, Surface-supported metal–organic framework thin films: fabrication methods, applications, and challenges, *Chemical Society Reviews*, 46 (2017) 5730-5770.
- [15] K.B. Blodgett, I. Langmuir, Built-up films of barium stearate and their optical properties, *Physical Review*, 51 (1937) 964.
- [16] O. Shekhah, H. Wang, S. Kowarik, F. Schreiber, M. Paulus, M. Tolan, C. Sternemann, F. Evers, D. Zacher, R.A. Fischer, Step-by-step route for the synthesis of metal–organic frameworks, *Journal of the American Chemical Society*, 129 (2007) 15118-15119.
- [17] O. Shekhah, H. Wang, M. Paradinas, C. Ocal, B. Schüpbach, A. Terfort, D. Zacher, R.A. Fischer, C. Wöll, Controlling interpenetration in metal–organic frameworks by liquid-phase epitaxy, *Nature Materials*, 8 (2009) 481-484.
- [18] O. Shekhah, Layer-by-layer method for the synthesis and growth of surface mounted metal-organic frameworks (SURMOFs), *Materials*, 3 (2010) 1302-1315.
- [19] O. Zybalyo, O. Shekhah, H. Wang, M. Tafipolsky, R. Schmid, D. Johannsmann, C. Wöll, A novel method to measure diffusion coefficients in porous metal–organic frameworks, *Physical Chemistry Chemical Physics*, 12 (2010) 8093-8098.
- [20] H.K. Arslan, O. Shekhah, J. Wohlgemuth, M. Franzreb, R.A. Fischer, C. Wöll, High-Throughput Fabrication of Uniform and Homogenous MOF Coatings, *Advanced functional materials*, 21 (2011) 4228-4231.
- [21] P. St. Petkov, G.N. Vayssilov, J. Liu, O. Shekhah, Y. Wang, C. Wöll, T. Heine, Defects in MOFs: a thorough characterization, *ChemPhysChem*, 13 (2012) 2025-2029.
- [22] E. Redel, Z. Wang, S. Walheim, J. Liu, H. Gliemann, C. Wöll, On the dielectric and optical properties of surface-anchored metal-organic frameworks: A study on epitaxially grown thin films, *Applied Physics Letters*, 103 (2013) 091903.
- [23] T. Ladnorg, A. Welle, S. Heißler, C. Wöll, H. Gliemann, Site-selective growth of surface-anchored metal-organic frameworks on self-assembled monolayer patterns prepared by AFM nanografting, *Beilstein Journal of Nanotechnology*, 4 (2013) 638-648.

- [24] M. Tu, R.A. Fischer, Heteroepitaxial growth of surface mounted metal–organic framework thin films with hybrid adsorption functionality, *Journal of Materials Chemistry A*, 2 (2014) 2018-2022.
- [25] W. Guo, J. Liu, P.G. Weidler, J. Liu, T. Neumann, D. Danilov, W. Wenzel, C. Feldmann, C. Wöll, Loading of ionic compounds into metal–organic frameworks: a joint theoretical and experimental study for the case of La³⁺, *Physical Chemistry Chemical Physics*, 16 (2014) 17918-17923.
- [26] J.P. Best, J. Michler, J. Liu, Z. Wang, M. Tsotsalas, X. Maeder, S. Röse, V. Oberst, J. Liu, S. Walheim, Nanomechanical investigation of thin-film electroceramic/metal-organic framework multilayers, *Applied Physics Letters*, 107 (2015) 101902.
- [27] J. Liu, E. Redel, S. Walheim, Z. Wang, V. Oberst, J. Liu, S. Heissler, A. Welle, M. Moosmann, T. Scherer, Monolithic high performance surface anchored metal–organic framework Bragg reflector for optical sensing, *Chemistry of Materials*, 27 (2015) 1991-1996.
- [28] Z.-G. Gu, A. Pfriem, S. Hamsch, H. Breitwieser, J. Wohlgemuth, L. Heinke, H. Gliemann, C. Wöll, Transparent films of metal-organic frameworks for optical applications, *Microporous and Mesoporous Materials*, 211 (2015) 82-87.
- [29] J. Liu, T. Wächter, A. Irmeler, P.G. Weidler, H. Gliemann, F. Pauly, V. Mugnaini, M. Zharnikov, C. Wöll, Electric transport properties of surface-anchored metal–organic frameworks and the effect of ferrocene loading, *ACS applied materials & interfaces*, 7 (2015) 9824-9830.
- [30] Z. Wang, P.G. Weidler, C. Azucena, L. Heinke, C. Wöll, Negative, anisotropic thermal expansion in monolithic thin films of crystalline metal-organic frameworks, *Microporous and Mesoporous Materials*, 222 (2016) 241-246.
- [31] Z. Wang, D. Nminibapiel, P. Shrestha, J. Liu, W. Guo, P.G. Weidler, H. Baumgart, C. Wöll, E. Redel, Resistive switching nanodevices based on metal–organic frameworks, *ChemNanoMat*, 2 (2016) 67-73.
- [32] W. Guo, Z. Chen, C. Yang, T. Neumann, C. Kübel, W. Wenzel, A. Welle, W. Pflöging, O. Shekhah, C. Wöll, Bi₂O₃ nanoparticles encapsulated in surface mounted metal–organic framework thin films, *Nanoscale*, 8 (2016) 6468-6472.
- [33] Z.-G. Gu, S.-C. Chen, W.-Q. Fu, Q. Zheng, J. Zhang, Epitaxial growth of MOF thin film for modifying the dielectric layer in organic field-effect transistors, *ACS Applied Materials & Interfaces*, 9 (2017) 7259-7264.

- [34] Z.-G. Gu, D.-X. Zhang, W.-Q. Fu, Z.-H. Fu, M.I. Vohra, L. Zhang, C. Wöll, J. Zhang, Facile Synthesis of Metal-Loaded Porous Carbon Thin Films via Carbonization of Surface-Mounted Metal–Organic Frameworks, *Inorganic Chemistry*, 56 (2017) 3526-3531.
- [35] K. Müller, J. Wadhwa, J.S. Malhi, L. Schöttner, A. Welle, H. Schwartz, D. Hermann, U. Ruschewitz, L. Heinke, Photoswitchable nanoporous films by loading azobenzene in metal–organic frameworks of type HKUST-1, *Chemical Communications*, 53 (2017) 8070-8073.
- [36] X. Chen, Z. Wang, Z.M. Hassan, P. Lin, K. Zhang, H. Baumgart, E. Redel, Seebeck Coefficient Measurements of Polycrystalline and Highly Ordered Metal–Organic Framework Thin Films, *ECS Journal of Solid State Science and Technology*, 6 (2017) P150.
- [37] Z.-G. Gu, W.-Q. Fu, M. Liu, J. Zhang, Surface-mounted MOF templated fabrication of homochiral polymer thin film for enantioselective adsorption of drugs, *Chemical Communications*, 53 (2017) 1470-1473.
- [38] B.H. Bowser, L.J. Brower, M.L. Ohnsorg, L.K. Gentry, C.K. Beaudoin, M.E. Anderson, Comparison of surface-bound and free-standing variations of HKUST-1 MOFs: Effect of activation and ammonia exposure on morphology, crystallinity, and composition, *Nanomaterials*, 8 (2018) 650.
- [39] G. Delen, Z. Ristanović, L.D. Mandemaker, B.M. Weckhuysen, Mechanistic Insights into Growth of Surface-Mounted Metal–Organic Framework Films Resolved by Infrared (Nano-) Spectroscopy, *Chemistry–A European Journal*, 24 (2018) 187-195.
- [40] Q. Zhao, Y. Fan, Y. Zhang, J. Liu, W. Li, Y. Weng, Copper-based SURMOFs for nitric oxide generation: hemocompatibility, vascular cell growth, and tissue response, *ACS applied materials & interfaces*, 11 (2019) 7872-7883.
- [41] A.B. Kanj, R. Verma, M. Liu, J. Helfferich, W. Wenzel, L. Heinke, Bunching and immobilization of ionic liquids in nanoporous metal–organic framework, *Nano Letters*, 19 (2019) 2114-2120.
- [42] T.P. Vello, M. Strauss, C.A.R. Costa, C.C. Corrêa, C.C.B. Bufon, Deterministic control of surface mounted metal–organic framework growth orientation on metallic and insulating surfaces, *Physical Chemistry Chemical Physics*, 22 (2020) 5839-5846.

- [43] X.-J. Yu, H. Zhong, Y.-M. Xian, Z.-P. Wang, S. Schneider, J. Scherr, T. Abu-Husein, Z. Zhang, A. Terfort, Highly oriented and polyoxometalate-incorporating surface-attached metal–organic frameworks for efficient dye adsorption and water oxidation, *Dalton Transactions*, 49 (2020) 16627-16632.
- [44] L.G. Albano, T.P. Vello, D.H. de Camargo, R.M. da Silva, A.C. Padilha, A. Fazio, C.C. Bufon, Ambipolar resistive switching in an ultrathin surface-supported metal–organic framework vertical heterojunction, *Nano Letters*, 20 (2020) 1080-1088.
- [45] H. Ohara, S. Yamamoto, D. Kuzuhara, T. Koganezawa, H. Oikawa, M. Mitsuishi, Layer-by-layer growth control of metal–organic framework thin films assembled on polymer films, *ACS Applied Materials & Interfaces*, 12 (2020) 50784-50792.
- [46] L.D. Mandemaker, M. Rivera-Torrente, R. Geitner, C.M. Vis, B.M. Weckhuysen, In Situ Spectroscopy of Calcium Fluoride Anchored Metal–Organic Framework Thin Films during Gas Sorption, *Angewandte Chemie International Edition*, 59 (2020) 19545-19552.
- [47] Z. Wang, S. Henke, M. Paulus, A. Welle, Z. Fan, K. Rodewald, B. Rieger, R.A. Fischer, Defect Creation in Surface-Mounted Metal–Organic Framework Thin Films, *ACS applied materials & interfaces*, 12 (2019) 2655-2661.
- [48] G. Delen, M. Monai, F. Meirer, B.M. Weckhuysen, In situ Nanoscale Infrared Spectroscopy of Water Adsorption on Nanoislands of Surface-Anchored Metal-Organic Frameworks, *Angewandte Chemie International Edition*, 60 (2021) 1620-1624.
- [49] O. Lugier, N. Thakur, L. Wu, M. Vockenhuber, Y. Ekinici, S. Castellanos, Bottom-Up Nanofabrication with Extreme-Ultraviolet Light: Metal–Organic Frameworks on Patterned Monolayers, *ACS Applied Materials & Interfaces*, 13 (2021) 43777-43786.
- [50] A. Oliveira, J. Ribeiro, D. Vasconcelos, P. Weidler, W. Vasconcelos, Room temperature and ambient pressure deposition of Cu-BTC MOF on SBA-15 functionalized silica supports by simple spray layer-by-layer method, *Materials Today Communications*, 27 (2021) 102388.
- [51] R.M. da Silva, L.G. Albano, T.P. Vello, W.W. de Araújo, D.H. de Camargo, L.D. Palermo, C.C. Corrêa, C. Wöll, C.C. Bufon, Surface-Supported Metal-Organic Framework as Low-Dielectric-Constant Thin Films for Novel Hybrid Electronics, *Advanced Electronic Materials*, 8 (2022) 2200175.

- [52] X. Chen, K. Zhang, Z.M. Hassan, E. Redel, H. Baumgart, Charge transport, conductivity and Seebeck coefficient in pristine and TCNQ loaded preferentially grown metal-organic framework films, *Journal of Physics: Condensed Matter*, 34 (2022) 404001.
- [53] Z. Li, J. Liu, L. Feng, Y. Pan, J. Tang, H. Li, G. Cheng, Z. Li, J. Shi, Y. Xu, Monolithic MOF-Based Metal–Insulator–Metal Resonator for Filtering and Sensing, *Nano Letters*, (2023).
- [54] B. Liu, O. Shekhah, H.K. Arslan, J. Liu, C. Wöll, R.A. Fischer, Enantiopure metal–organic framework thin films: oriented SURMOF growth and enantioselective adsorption, *Angewandte Chemie International Edition*, 51 (2012) 807-810.
- [55] J. Liu, O. Shekhah, X. Stammer, H.K. Arslan, B. Liu, B. Schüpbach, A. Terfort, C. Wöll, Deposition of metal-organic frameworks by liquid-phase epitaxy: The influence of substrate functional group density on film orientation, *Materials*, 5 (2012) 1581-1592.
- [56] L. Heinke, C. Wöll, Adsorption and diffusion in thin films of nanoporous metal–organic frameworks: ferrocene in SURMOF Cu₂(ndc)₂(dabco), *Physical Chemistry Chemical Physics*, 15 (2013) 9295-9299.
- [57] B. Liu, M. Tu, D. Zacher, R.A. Fischer, Multi variant surface mounted metal–organic frameworks, *Advanced Functional Materials*, 23 (2013) 3790-3798.
- [58] M. Tu, S. Wannapaiboon, R.A. Fischer, Programmed functionalization of SURMOFs via liquid phase heteroepitaxial growth and post-synthetic modification, *Dalton Transactions*, 42 (2013) 16029-16035.
- [59] L. Heinke, M. Cakici, M. Dommaschk, S. Grosjean, R. Herges, S. Bräse, C. Wöll, Photoswitching in two-component surface-mounted metal–organic frameworks: optically triggered release from a molecular container, *ACS nano*, 8 (2014) 1463-1467.
- [60] Z.G. Gu, J. Bürck, A. Bihlmeier, J. Liu, O. Shekhah, P.G. Weidler, C. Azucena, Z. Wang, S. Heissler, H. Gliemann, Oriented Circular Dichroism Analysis of Chiral Surface-Anchored Metal–Organic Frameworks Grown by Liquid-Phase Epitaxy and upon Loading with Chiral Guest Compounds, *Chemistry–A European Journal*, 20 (2014) 9879-9882.
- [61] S. Wannapaiboon, M. Tu, R.A. Fischer, Liquid Phase Heteroepitaxial Growth of Moisture-Tolerant MOF-5 Isotype Thin Films and Assessment of the Sorption

Properties by Quartz Crystal Microbalance, *Advanced Functional Materials*, 24 (2014) 2696-2705.

[62] J.-L. Zhuang, M. Kind, C.M. Grytz, F. Farr, M. Diefenbach, S. Tussupbayev, M.C. Holthausen, A. Terfort, Insight into the oriented growth of surface-attached metal–organic frameworks: surface functionality, deposition temperature, and first layer order, *Journal of the American Chemical Society*, 137 (2015) 8237-8243.

[63] Z. Wang, J. Liu, S. Grosjean, D. Wagner, W. Guo, Z. Gu, L. Heinke, H. Gliemann, S. Bräse, C. Wöll, Monolithic, crystalline MOF Coating: An excellent patterning and photoresist material, *ChemNanoMat*, 1 (2015) 338-345.

[64] W. Guo, M. Zha, Z. Wang, E. Redel, Z. Xu, C. Wöll, Improving the Loading Capacity of Metal–Organic Framework Thin Films Using Optimized Linkers, *ACS Applied Materials & Interfaces*, 8 (2016) 24699-24702.

[65] E.P. Valadez Sánchez, H. Gliemann, K. Haas-Santo, C. Wöll, R. Dittmeyer, ZIF-8 SURMOF Membranes Synthesized by Au-Assisted Liquid Phase Epitaxy for Application in Gas Separation, *Chemie Ingenieur Technik*, 88 (2016) 1798-1805.

[66] L. Ye, J. Liu, Y. Gao, C. Gong, M. Addicoat, T. Heine, C. Wöll, L. Sun, Highly oriented MOF thin film-based electrocatalytic device for the reduction of CO₂ to CO exhibiting high faradaic efficiency, *Journal of Materials Chemistry A*, 4 (2016) 15320-15326.

[67] S. Ahmad, J. Liu, C. Gong, J. Zhao, L. Sun, Photon up-conversion via epitaxial surface-supported metal–organic framework thin films with enhanced photocurrent, *ACS Applied Energy Materials*, 1 (2018) 249-253.

[68] W. Zhou, S. Begum, Z. Wang, P. Krolla, D. Wagner, S. Bräse, C. Wöll, M. Tsotsalas, High antimicrobial activity of metal–organic framework-templated porphyrin polymer thin films, *ACS applied materials & interfaces*, 10 (2018) 1528-1533.

[69] S. Schmitt, S. Diring, P.G. Weidler, S. Begum, S. Heißler, S. Kitagawa, C. Wöll, S. Furukawa, M. Tsotsalas, Localized Conversion of Metal–Organic Frameworks into Polymer Gels via Light-Induced Click Chemistry, *Chemistry of Materials*, 29 (2017) 5982-5989.

[70] Y.Y. Wang, S.M. Chen, R. Haldar, C. Wöll, Z.G. Gu, J. Zhang, van der Waals Epitaxial Growth of 2D Metal–Porphyrin Framework Derived Thin Films for Dye-Sensitized Solar Cells, *Advanced Materials Interfaces*, 5 (2018) 1800985.

- [71] R. Haldar, S. Diring, P.K. Samanta, M. Muth, W. Clancy, A. Mazel, S. Schlabach, F. Kirschhöfer, G. Brenner-Weiß, S.K. Pati, Enhancing selectivity and kinetics in oxidative photocyclization by supramolecular control, *Angewandte Chemie International Edition*, 57 (2018) 13662-13665.
- [72] R. Haldar, B. Sen, S. Hurrle, T. Kitao, R. Sankhla, B. Köhl, A. Welle, S. Heissler, G. Brenner-Weiß, P. Thissen, Oxidative polymerization of terthiophene and a substituted thiophene monomer in metal-organic framework thin films, *European Polymer Journal*, 109 (2018) 162-168.
- [73] C. Gu, H. Zhang, P. You, Q. Zhang, G. Luo, Q. Shen, Z. Wang, J. Hu, Giant and multistage nonlinear optical response in porphyrin-based surface-supported metal-organic framework nanofilms, *Nano Letters*, 19 (2019) 9095-9101.
- [74] D.H. Chen, R. Haldar, B.L. Neumeier, Z.H. Fu, C. Feldmann, C. Wöll, E. Redel, Tunable Emission in Heteroepitaxial Ln-SURMOFs, *Advanced Functional Materials*, 29 (2019) 1903086.
- [75] W. Li, S. Watzele, H.A. El-Sayed, Y. Liang, G. Kieslich, A.S. Bandarenka, K. Rodewald, B. Rieger, R.A. Fischer, Unprecedented high oxygen evolution activity of electrocatalysts derived from surface-mounted metal-organic frameworks, *Journal of the American Chemical Society*, 141 (2019) 5926-5933.
- [76] A.L. Semrau, S. Wannapaiboon, S.P. Pujari, P. Vervoorts, B. Albada, H. Zuilhof, R.A. Fischer, Highly Porous Nanocrystalline UiO-66 Thin Films via Coordination Modulation Controlled Step-by-Step Liquid-Phase Growth, *Crystal Growth & Design*, 19 (2018) 1738-1747.
- [77] B.D. McCarthy, T. Liseev, A.M. Beiler, K.L. Materna, S. Ott, Facile Orientational Control of M2L2P SURMOFs on(100) Silicon Substrates and Growth Mechanism Insights for Defective MOFs, *ACS applied materials & interfaces*, 11 (2019) 38294-38302.
- [78] X.-J. Yu, Y.-M. Xian, C. Wang, H.-L. Mao, M. Kind, T. Abu-Husein, Z. Chen, S.-B. Zhu, B. Ren, A. Terfort, Liquid-phase epitaxial growth of highly oriented and multivariate surface-attached metal-organic frameworks, *Journal of the American Chemical Society*, 141 (2019) 18984-18993.
- [79] R. Haldar, K. Batra, S.M. Marschner, A.B. Kuc, S. Zahn, R.A. Fischer, S. Bräse, T. Heine, C. Wöll, Bridging the green gap: metal-organic framework heteromultilayers assembled from porphyrinic linkers identified by using computational screening, *Chemistry—A European Journal*, 25 (2019) 7847-7851.

- [80] S.-M. Chen, L.-M. Chang, X.-K. Yang, T. Luo, H. Xu, Z.-G. Gu, J. Zhang, Liquid-phase epitaxial growth of azapyrene-based chiral metal–organic framework thin films for circularly polarized luminescence, *ACS applied materials & interfaces*, 11 (2019) 31421-31426.
- [81] A.B. Kanj, J. Bürck, S. Grosjean, S. Bräse, L. Heinke, Switching the enantioselectivity of nanoporous host materials by light, *Chemical communications*, 55 (2019) 8776-8779.
- [82] A.B. Kanj, A. Chandresh, A. Gerwien, S. Grosjean, S. Bräse, Y. Wang, H. Dube, L. Heinke, Proton-conduction photomodulation in spiropyran-functionalized MOFs with large on–off ratio, *Chemical Science*, 11 (2020) 1404-1410.
- [83] O. Lugier, U. Pokharel, S. Castellanos, Impact of synthetic conditions on the morphology and crystallinity of FDMOF-1 (Cu) thin films, *Crystal Growth & Design*, 20 (2020) 5302-5309.
- [84] S. Klyatskaya, A.B. Kanj, C.n. Molina-Jirón, S. Heidrich, L. Velasco, C. Natzeck, H. Gliemann, S. Heissler, P. Weidler, W. Wenzel, Conductive metal–organic framework thin film hybrids by electropolymerization of monosubstituted acetylenes, *ACS applied materials & interfaces*, 12 (2020) 30972-30979.
- [85] R. Haldar, M. Jakoby, M. Kozłowska, M. Rahman Khan, H. Chen, Y. Pramudya, B.S. Richards, L. Heinke, W. Wenzel, F. Odobel, Tuning Optical Properties by Controlled Aggregation: Electroluminescence Assisted by Thermally-Activated Delayed Fluorescence from Thin Films of Crystalline Chromophores, *Chemistry–A European Journal*, 26 (2020) 17016-17020.
- [86] A. Chandresh, X. Liu, C. Wöll, L. Heinke, Programmed molecular assembly of abrupt crystalline organic/organic heterointerfaces yielding metal-organic framework diodes with large on-off ratios, *Advanced science*, 8 (2021) 2001884.
- [87] J. Liu, S. Heidrich, J. Liu, B. Guo, M. Zharnikov, U. Simon, W. Wenzel, C. Wöll, Encapsulation of Au₅₅ Clusters within Surface-Supported Metal–Organic Frameworks for Catalytic Reduction of 4-Nitrophenol, *ACS Applied Nano Materials*, 4 (2020) 522-528.
- [88] S. Lei, L.-M. Chang, Z.-G. Gu, J. Zhang, A metal-porphyrinic framework film as an efficient optical limiting layer in an electro-optical switchable device, *Chemical Communications*, 57 (2021) 10166-10169.
- [89] Y. Lin, W.H. Li, Y. Wen, G.E. Wang, X.L. Ye, G. Xu, Layer-by-Layer growth of preferred-oriented MOF thin film on nanowire array for high-performance

chemiresistive sensing, *Angewandte Chemie International Edition*, 60 (2021) 25758-25761.

[90] X. Liu, A. Mazel, S. Marschner, Z. Fu, M. Muth, F. Kirschhöfer, G. Brenner-Weiss, S. Bräse, S. Diring, F. Odobel, Photoinduced Delamination of Metal–Organic Framework Thin Films by Spatioselective Generation of Reactive Oxygen Species, *ACS Applied Materials & Interfaces*, 13 (2021) 57768-57773.

[91] Z.M. Hassan, P.G. Weidler, A. Nefedov, Y. Luo, S. Heißler, M. Tsotsalas, R. Haldar, C. Wöll, Spectroscopic Investigation of Bianthryl-Based Metal–Organic Framework Thin Films and Their Photoinduced Topotactic Transformation, *Advanced Materials Interfaces*, 9 (2022) 2102441.

[92] R. Zheng, Z.H. Fu, W.H. Deng, Y. Wen, A.Q. Wu, X.L. Ye, G. Xu, The Growth Mechanism of a Conductive MOF Thin Film in Spray-based Layer-by-layer Liquid Phase Epitaxy, *Angewandte Chemie International Edition*, 61 (2022) e202212797.

[93] B.H. Monjezi, S. Okur, R. Limbach, A. Chandresh, K. Sen, T. Hashem, M. Schwotzer, L. Wondraczek, C. Wöll, A. Knebel, Fast dynamic synthesis of MIL-68 (In) thin films in high optical quality for optical cavity sensing, *ACS nano*, (2022).

[94] Z.-G. Gu, J. Zhang, Epitaxial growth and applications of oriented metal–organic framework thin films, *Coordination Chemistry Reviews*, 378 (2019) 513-532.

[95] M. Kind, C. Wöll, Organic surfaces exposed by self-assembled organothiols monolayers: Preparation, characterization, and application, *Progress in Surface Science*, 84 (2009) 230-278.

[96] A. Betard, R.A. Fischer, Metal–organic framework thin films: from fundamentals to applications, *Chemical reviews*, 112 (2012) 1055-1083.

[97] J.L. Zhuang, D. Ar, X.J. Yu, J.X. Liu, A. Terfort, Patterned deposition of metal-organic frameworks onto plastic, paper, and textile substrates by inkjet printing of a precursor solution, *Advanced materials*, 25 (2013) 4631-4635.

[98] H.K. Arslan, O. Shekhah, D.F. Wieland, M. Paulus, C. Sternemann, M.A. Schroer, S. Tiemeyer, M. Tolan, R.A. Fischer, C. Wöll, Intercalation in layered metal–organic frameworks: reversible inclusion of an extended π -system, *Journal of the American Chemical Society*, 133 (2011) 8158-8161.

[99] X. Zhang, Z. Chen, X. Liu, S.L. Hanna, X. Wang, R. Taheri-Ledari, A. Maleki, P. Li, O.K. Farha, A historical overview of the activation and porosity of metal–organic frameworks, *Chemical Society Reviews*, 49 (2020) 7406-7427.

- [100] W.-Q. Fu, M. Liu, Z.-G. Gu, S.-M. Chen, J. Zhang, Liquid phase epitaxial growth and optical properties of photochromic guest-encapsulated MOF thin film, *Crystal Growth & Design*, 16 (2016) 5487-5492.
- [101] Z. Wang, C. Wöll, Fabrication of Metal–Organic Framework Thin Films Using Programmed Layer-by-Layer Assembly Techniques, *Advanced Materials Technologies*, 4 (2019) 1800413.
- [102] O. Shekhah, H. Wang, T. Strunskus, P. Cyganik, D. Zacher, R. Fischer, C. Wöll, Layer-by-layer growth of oriented metal organic polymers on a functionalized organic surface, *Langmuir*, 23 (2007) 7440-7442.
- [103] H. Noei, S. Amirjalayer, M. Müller, X. Zhang, R. Schmid, M. Muhler, R.A. Fischer, Y. Wang, Low-Temperature CO Oxidation over Cu-Based Metal–Organic Frameworks Monitored by using FTIR Spectroscopy, *ChemCatChem*, 4 (2012) 755-759.
- [104] W. Wang, D.I. Sharapa, A. Chandresh, A. Nefedov, S. Heißler, L. Heinke, F. Studt, Y. Wang, C. Wöll, Interplay of Electronic and Steric Effects to Yield Low-Temperature CO Oxidation at Metal Single Sites in Defect-Engineered HKUST-1, *Angewandte Chemie International Edition*, 59 (2020) 10514-10518.
- [105] J. Phair, S. Badwal, Materials for separation membranes in hydrogen and oxygen production and future power generation, *Science and technology of advanced materials*, 7 (2006) 792.
- [106] Z. Wang, A. Knebel, S. Grosjean, D. Wagner, S. Bräse, C. Wöll, J. Caro, L. Heinke, Tunable molecular separation by nanoporous membranes, *Nature communications*, 7 (2016) 13872.
- [107] A.A. Talin, A. Centrone, A.C. Ford, M.E. Foster, V. Stavila, P. Haney, R.A. Kinney, V. Szalai, F. El Gabaly, H.P. Yoon, Tunable electrical conductivity in metal-organic framework thin-film devices, *Science*, 343 (2014) 66-69.
- [108] K.J. Erickson, F. Léonard, V. Stavila, M.E. Foster, C.D. Spataru, R.E. Jones, B.M. Foley, P.E. Hopkins, M.D. Allendorf, A.A. Talin, Thin film thermoelectric metal–organic framework with high Seebeck coefficient and low thermal conductivity, *Advanced Materials*, 27 (2015) 3453-3459.
- [109] S. Friedländer, J. Liu, M. Addicoat, P. Petkov, N. Vankova, R. Rüger, A. Kuc, W. Guo, W. Zhou, B. Lukose, Linear chains of magnetic ions stacked with variable distance: ferromagnetic ordering with a Curie temperature above 20 K, *Angewandte Chemie International Edition*, 55 (2016) 12683-12687.

- [110] A.-Q. Wu, W.-Q. Wang, H.-B. Zhan, L.-A. Cao, X.-L. Ye, J.-J. Zheng, P.N. Kumar, K. Chiranjeevulu, W.-H. Deng, G.-E. Wang, Layer-by-layer assembled dual-ligand conductive MOF nano-films with modulated chemiresistive sensitivity and selectivity, *Nano Research*, 14 (2021) 438-443.
- [111] L.G. Albano, D.H. de Camargo, G.R. Schleder, S.G. Deeke, T.P. Vello, L.D. Palermo, C.C. Corrêa, A. Fazzio, C. Wöll, C.C. Bufon, Room-Temperature Negative Differential Resistance in Surface-Supported Metal-Organic Framework Vertical Heterojunctions, *Small*, 17 (2021) 2101475.
- [112] M. Vazquez, M. Liu, Z. Zhang, A. Chandresh, A.B. Kanj, W. Wenzel, L. Heinke, Structural and dynamic insights into the conduction of lithium-ionic-liquid mixtures in nanoporous metal–organic frameworks as solid-state electrolytes, *ACS Applied Materials & Interfaces*, 13 (2021) 21166-21174.
- [113] D. Britt, C. Lee, F.J. Uribe-Romo, H. Furukawa, O.M. Yaghi, Ring-opening reactions within porous metal–organic frameworks, *Inorganic chemistry*, 49 (2010) 6387-6389.
- [114] S.M. Cohen, Modifying MOFs: new chemistry, new materials, *Chemical Science*, 1 (2010) 32-36.
- [115] C.T. Walsh, S. Garneau-Tsodikova, G.J. Gatto Jr, Protein posttranslational modifications: the chemistry of proteome diversifications, *Angewandte Chemie International Edition*, 44 (2005) 7342-7372.
- [116] S.C. Jones, C.A. Bauer, Diastereoselective heterogeneous bromination of stilbene in a porous metal–organic framework, *Journal of the American Chemical Society*, 131 (2009) 12516-12517.
- [117] T. Kawamichi, T. Haneda, M. Kawano, M. Fujita, X-ray observation of a transient hemiaminal trapped in a porous network, *Nature*, 461 (2009) 633-635.
- [118] H. Sato, R. Matsuda, K. Sugimoto, M. Takata, S. Kitagawa, Photoactivation of a nanoporous crystal for on-demand guest trapping and conversion, *Nature materials*, 9 (2010) 661-666.
- [119] Y. Wang, C. Wöll, Chemical reactions at isolated single-sites inside metal–organic frameworks, *Catalysis Letters*, 148 (2018) 2201-2222.
- [120] L. Duarte, R. Fausto, I. Reva, Structural and spectroscopic characterization of E-and Z-isomers of azobenzene, *Physical Chemistry Chemical Physics*, 16 (2014) 16919-16930.

- [121] M. Fujita, Y.J. Kwon, S. Washizu, K. Ogura, Preparation, clathration ability, and catalysis of a two-dimensional square network material composed of cadmium (II) and 4, 4'-bipyridine, *Journal of the American Chemical Society*, 116 (1994) 1151-1152.
- [122] D. Li, H.-Q. Xu, L. Jiao, H.-L. Jiang, Metal-organic frameworks for catalysis: State of the art, challenges, and opportunities, *EnergyChem*, 1 (2019) 100005.
- [123] C. Luo, F. Fu, X. Yang, J. Wei, C. Wang, J. Zhu, D. Huang, D. Astruc, P. Zhao, Highly Efficient and Selective Co@ ZIF-8 Nanocatalyst for Hydrogen Release from Sodium Borohydride Hydrolysis, *ChemCatChem*, 11 (2019) 1643-1649.
- [124] J. Cheng, X. Gu, P. Liu, H. Zhang, L. Ma, H. Su, Achieving efficient room-temperature catalytic H₂ evolution from formic acid through atomically controlling the chemical environment of bimetallic nanoparticles immobilized by isorecticular amine-functionalized metal-organic frameworks, *Applied Catalysis B: Environmental*, 218 (2017) 460-469.
- [125] P. Ji, Y. Song, T. Drake, S.S. Veroneau, Z. Lin, X. Pan, W. Lin, Titanium (III)-oxo clusters in a metal-organic framework support single-site Co (II)-hydride catalysts for arene hydrogenation, *Journal of the American Chemical Society*, 140 (2018) 433-440.
- [126] B. Li, J.G. Ma, P. Cheng, Silica-protection-assisted encapsulation of Cu₂O nanocubes into a metal-organic framework (ZIF-8) to provide a composite catalyst, *Angewandte Chemie*, 130 (2018) 6950-6953.
- [127] M. Zhao, K. Yuan, Y. Wang, G. Li, J. Guo, L. Gu, W. Hu, H. Zhao, Z. Tang, Metal-organic frameworks as selectivity regulators for hydrogenation reactions, *Nature*, 539 (2016) 76-80.
- [128] B. An, J. Zhang, K. Cheng, P. Ji, C. Wang, W. Lin, Confinement of ultrasmall Cu/ZnO_x nanoparticles in metal-organic frameworks for selective methanol synthesis from catalytic hydrogenation of CO₂, *Journal of the American Chemical Society*, 139 (2017) 3834-3840.
- [129] X. Sun, A.I.O. Suarez, M. Meijerink, T. Van Deelen, S. Ould-Chikh, J. Zečević, K.P. De Jong, F. Kapteijn, J. Gascon, Manufacture of highly loaded silica-supported cobalt Fischer – Tropsch catalysts from a metal organic framework, *Nature communications*, 8 (2017) 1680.

- [130] R.V. Jagadeesh, K. Murugesan, A.S. Alshammari, H. Neumann, M.-M. Pohl, J. Radnik, M. Beller, MOF-derived cobalt nanoparticles catalyze a general synthesis of amines, *Science*, 358 (2017) 326-332.
- [131] P. Zhang, C. Chen, X. Kang, L. Zhang, C. Wu, J. Zhang, B. Han, In situ synthesis of sub-nanometer metal particles on hierarchically porous metal–organic frameworks via interfacial control for highly efficient catalysis, *Chemical Science*, 9 (2018) 1339-1343.
- [132] S. Fan, W. Dong, X. Huang, H. Gao, J. Wang, Z. Jin, J. Tang, G. Wang, In situ-induced synthesis of magnetic Cu-CuFe₂O₄@ HKUST-1 heterostructures with enhanced catalytic performance for selective aerobic benzylic C–H oxidation, *Acs Catalysis*, 7 (2017) 243-249.
- [133] S. Ji, Y. Chen, Q. Fu, Y. Chen, J. Dong, W. Chen, Z. Li, Y. Wang, L. Gu, W. He, Confined pyrolysis within metal–organic frameworks to form uniform Ru₃ clusters for efficient oxidation of alcohols, *Journal of the American Chemical Society*, 139 (2017) 9795-9798.
- [134] X.-X. Zheng, L.-J. Shen, X.-P. Chen, X.-H. Zheng, C.-T. Au, L.-L. Jiang, Amino-modified Fe-terephthalate metal–organic framework as an efficient catalyst for the selective oxidation of H₂S, *Inorganic Chemistry*, 57 (2018) 10081-10089.
- [135] H. Duan, Y. Zeng, X. Yao, P. Xing, J. Liu, Y. Zhao, Tuning synergistic effect of Au–Pd bimetallic nanocatalyst for aerobic oxidative carbonylation of amines, *Chemistry of Materials*, 29 (2017) 3671-3677.
- [136] D. Li, X. Dai, X. Zhang, H. Zhuo, Y. Jiang, Y.-B. Yu, P. Zhang, X. Huang, H. Wang, Silver nanoparticles encapsulated by metal-organic-framework give the highest turnover frequencies of 10⁵ h⁻¹ for three component reaction by microwave-assisted heating, *Journal of Catalysis*, 348 (2017) 276-281.
- [137] N. Yuan, V. Pascanu, Z. Huang, A. Valiente, N. Heidenreich, S. Leubner, A.K. Inge, J. Gaar, N. Stock, I. Persson, Probing the evolution of palladium species in Pd@ MOF catalysts during the heck coupling reaction: an operando X-ray absorption spectroscopy study, *Journal of the American Chemical Society*, 140 (2018) 8206-8217.
- [138] X.-L. Lv, K. Wang, B. Wang, J. Su, X. Zou, Y. Xie, J.-R. Li, H.-C. Zhou, A base-resistant metalloporphyrin metal–organic framework for C–H bond halogenation, *Journal of the American Chemical Society*, 139 (2017) 211-217.

- [139] D.J. Xiao, E.D. Bloch, J.A. Mason, W.L. Queen, M.R. Hudson, N. Planas, J. Borycz, A.L. Dzubak, P. Verma, K. Lee, Oxidation of ethane to ethanol by N₂O in a metal–organic framework with coordinatively unsaturated iron (II) sites, *Nature chemistry*, 6 (2014) 590-595.
- [140] W. Xie, F. Wan, Basic ionic liquid functionalized magnetically responsive Fe₃O₄@ HKUST-1 composites used for biodiesel production, *Fuel*, 220 (2018) 248-256.
- [141] J.-w. Zhang, G.-p. Lu, C. Cai, Self-hydrogen transfer hydrogenolysis of β -O-4 linkages in lignin catalyzed by MIL-100 (Fe) supported Pd–Ni BMNPs, *Green Chemistry*, 19 (2017) 4538-4543.
- [142] Y.P. Wu, W. Zhou, J. Zhao, W.W. Dong, Y.Q. Lan, D.S. Li, C. Sun, X. Bu, Surfactant-assisted phase-selective synthesis of new cobalt MOFs and their efficient electrocatalytic hydrogen evolution reaction, *Angewandte Chemie*, 129 (2017) 13181-13185.
- [143] R. Wang, X.Y. Dong, J. Du, J.Y. Zhao, S.Q. Zang, MOF-derived bifunctional Cu₃P nanoparticles coated by a N, P-codoped carbon shell for hydrogen evolution and oxygen reduction, *Advanced Materials*, 30 (2018) 1703711.
- [144] M. Khalid, A.M. Honorato, H. Varela, L. Dai, Multifunctional electrocatalysts derived from conducting polymer and metal organic framework complexes, *Nano Energy*, 45 (2018) 127-135.
- [145] K. Rui, G. Zhao, Y. Chen, Y. Lin, Q. Zhou, J. Chen, J. Zhu, W. Sun, W. Huang, S.X. Dou, Hybrid 2D dual-metal–organic frameworks for enhanced water oxidation catalysis, *Advanced Functional Materials*, 28 (2018) 1801554.
- [146] Y. Deng, Y. Dong, G. Wang, K. Sun, X. Shi, L. Zheng, X. Li, S. Liao, Well-defined ZIF-derived Fe–N codoped carbon nanoframes as efficient oxygen reduction catalysts, *ACS applied materials & interfaces*, 9 (2017) 9699-9709.
- [147] X. Wang, Z. Chen, X. Zhao, T. Yao, W. Chen, R. You, C. Zhao, G. Wu, J. Wang, W. Huang, Regulation of coordination number over single Co sites: triggering the efficient electroreduction of CO₂, *Angewandte Chemie*, 130 (2018) 1962-1966.
- [148] X. Sun, L. Lu, Q. Zhu, C. Wu, D. Yang, C. Chen, B. Han, MoP nanoparticles supported on indium-doped porous carbon: outstanding catalysts for highly efficient CO₂ electroreduction, *Angewandte Chemie International Edition*, 57 (2018) 2427-2431.

- [149] D.-H. Nam, O.S. Bushuyev, J. Li, P. De Luna, A. Seifitokaldani, C.-T. Dinh, F.P. García de Arquer, Y. Wang, Z. Liang, A.H. Proppe, Metal–organic frameworks mediate Cu coordination for selective CO₂ electroreduction, *Journal of the American Chemical Society*, 140 (2018) 11378-11386.
- [150] H. Li, Y. Sun, Z.Y. Yuan, Y.P. Zhu, T.Y. Ma, Titanium phosphonate based metal–organic frameworks with hierarchical porosity for enhanced photocatalytic hydrogen evolution, *Angewandte Chemie International Edition*, 57 (2018) 3222-3227.
- [151] J.D. Xiao, L. Han, J. Luo, S.H. Yu, H.L. Jiang, Integration of Plasmonic Effects and Schottky Junctions into Metal–Organic Framework Composites: Steering Charge Flow for Enhanced Visible-Light Photocatalysis, *Angewandte Chemie International Edition*, 57 (2018) 1103-1107.
- [152] B. Han, X. Ou, Z. Deng, Y. Song, C. Tian, H. Deng, Y.J. Xu, Z. Lin, Nickel metal–organic framework monolayers for photoreduction of diluted CO₂: metal-node-dependent activity and selectivity, *Angewandte Chemie International Edition*, 57 (2018) 16811-16815.
- [153] Y. Zhao, Y. Dong, F. Lu, C. Ju, L. Liu, J. Zhang, B. Zhang, Y. Feng, Coordinative integration of a metal-porphyrinic framework and TiO₂ nanoparticles for the formation of composite photocatalysts with enhanced visible-light-driven photocatalytic activities, *Journal of Materials Chemistry A*, 5 (2017) 15380-15389.
- [154] W. Li, S. Xue, S. Watzele, S. Hou, J. Fichtner, A.L. Semrau, L. Zhou, A. Welle, A.S. Bandarenka, R.A. Fischer, Advanced Bifunctional Oxygen Reduction and Evolution Electrocatalyst Derived from Surface-Mounted Metal–Organic Frameworks, *Angewandte Chemie*, 132 (2020) 5886-5892.
- [155] P. Larkin, *Infrared and Raman spectroscopy: principles and spectral interpretation*, Elsevier 2017.
- [156] J. Kattner, H. Hoffmann, External reflection spectroscopy of thin films on dielectric substrates, *Handbook of vibrational spectroscopy*, (2006).
- [157] Y. Cui, B. Li, H. He, W. Zhou, B. Chen, G. Qian, Metal–organic frameworks as platforms for functional materials, *Accounts of chemical research*, 49 (2016) 483-493.
- [158] Y.Y. Zhu, G. Lan, Y. Fan, S.S. Veroneau, Y. Song, D. Micheroni, W. Lin, Merging photoredox and organometallic catalysts in a metal–organic framework significantly boosts photocatalytic activities, *Angewandte Chemie International Edition*, 57 (2018) 14090-14094.

- [159] H. Yonezawa, S. Tashiro, T. Shiraogawa, M. Ehara, R. Shimada, T. Ozawa, M. Shionoya, Preferential photoreaction in a porous crystal, metal–macrocycle framework: PdII-mediated olefin migration over [2+ 2] cycloaddition, *Journal of the American Chemical Society*, 140 (2018) 16610-16614.
- [160] R. Xu, T. Drake, G. Lan, W. Lin, Metal-Organic Layers Catalyze Photoreactions without Pore Size and Diffusion Limitations, *Chemistry—A European Journal*, 24 (2018) 15772-15776.
- [161] G. Lan, Z. Li, S.S. Veroneau, Y.-Y. Zhu, Z. Xu, C. Wang, W. Lin, Photosensitizing metal–organic layers for efficient sunlight-driven carbon dioxide reduction, *Journal of the American Chemical Society*, 140 (2018) 12369-12373.
- [162] T. Luo, L. Li, Y. Chen, J. An, C. Liu, Z. Yan, J.H. Carter, X. Han, A.M. Sheveleva, F. Tuna, Construction of CC bonds via photoreductive coupling of ketones and aldehydes in the metal-organic-framework MFM-300 (Cr), *Nature Communications*, 12 (2021) 3583.
- [163] T. Devic, O. David, M. Valls, J. Marrot, F. Couty, G. Férey, An illustration of the limit of the metal organic framework's isoreticular principle using a semirigid tritopic linker obtained by “click” chemistry, *Journal of the American Chemical Society*, 129 (2007) 12614-12615.
- [164] T. Gadzikwa, O.K. Farha, C.D. Malliakas, M.G. Kanatzidis, J.T. Hupp, S.T. Nguyen, Selective bifunctional modification of a non-catenated metal– organic framework material via “Click” chemistry, *Journal of the American Chemical Society*, 131 (2009) 13613-13615.
- [165] S. Bräse, C. Gil, K. Knepper, V. Zimmermann, Organic azides: an exploding diversity of a unique class of compounds, *Angewandte Chemie International Edition*, 44 (2005) 5188-5240.
- [166] O.L. Chapman, J.P. Le Roux, 1-Aza-1, 2, 4, 6-cycloheptatetraene, *Journal of the American Chemical Society*, 100 (1978) 282-285.
- [167] Y.Z. Li, J.P. Kirby, M.W. George, M. Poliakoff, G.B. Schuster, 1, 2-Didehydroazepines from the photolysis of substituted aryl azides: analysis of their chemical and physical properties by time-resolved spectroscopic methods, *Journal of the American Chemical Society*, 110 (1988) 8092-8098.
- [168] G.B. Schuster, M.S. Platz, Photochemistry of phenyl azide, *Advances in photochemistry*, 17 (1992) 69-143.

- [169] M. Tsotsalas, J. Liu, B. Tettmann, S. Grosjean, A. Shahnas, Z. Wang, C. Azucena, M. Addicoat, T. Heine, J. Lahann, Fabrication of highly uniform gel coatings by the conversion of surface-anchored metal–organic frameworks, *Journal of the American Chemical Society*, 136 (2014) 8-11.
- [170] P.O. Scokart, P.G. Rouxhet, Characterization of the basicity of oxides through the infrared study of pyrrole adsorption, *Journal of the Chemical Society, Faraday Transactions 1: Physical Chemistry in Condensed Phases*, 76 (1980) 1476-1489.
- [171] F.R. Benson, W.L. Savell, The chemistry of the vicinal triazoles, *Chemical Reviews*, 46 (1950) 1-68.
- [172] E. Leyva, M.S. Platz, G. Persy, J. Wirz, Photochemistry of phenyl azide: the role of singlet and triplet phenylnitrene as transient intermediates, *Journal of the American Chemical Society*, 108 (1986) 3783-3790.
- [173] E.D. Stenehjem, V.R. Ziatdinov, T.D.P. Stack, C.E. Chidsey, Gas-phase azide functionalization of carbon, *Journal of the American Chemical Society*, 135 (2013) 1110-1116.
- [174] F. Bebensee, C. Bombis, S.-R. Vadapoo, J.R. Cramer, F. Besenbacher, K.V. Gothelf, T.R. Linderoth, On-surface azide–alkyne cycloaddition on Cu (111): does it “click” in ultrahigh vacuum?, *Journal of the American Chemical Society*, 135 (2013) 2136-2139.
- [175] I.H. Park, E. Lee, S.S. Lee, J.J. Vittal, Chemical patterning in single crystals of metal–organic frameworks by [2+ 2] cycloaddition reaction, *Angewandte Chemie International Edition*, 58 (2019) 14860-14864.
- [176] C. Liu, T. Li, N.L. Rosi, Strain-promoted “click” modification of a mesoporous metal–organic framework, *Journal of the American Chemical Society*, 134 (2012) 18886-18888.
- [177] H. Dong, M. Shen, J.E. Redford, B.J. Stokes, A.L. Pumphrey, T.G. Driver, Transition metal-catalyzed synthesis of pyrroles from dienyl azides, *Organic letters*, 9 (2007) 5191-5194.
- [178] H. Hemetsberger, I. Spira, W. Schoenfelder, *J. Chem. Res.(S)*, (1977).
- [179] L. Qiu, C. Yu, N. Zhao, W. Chen, Y. Guo, X. Wan, R. Yang, Y. Liu, An expedient synthesis of fused heteroacenes bearing a pyrrolo [3, 2-b] pyrrole core, *Chemical Communications*, 48 (2012) 12225-12227.

- [180] Y.Y. Lai, J.M. Yeh, C.E. Tsai, Y.J. Cheng, Synthesis, Molecular and Photovoltaic Properties of an Indolo [3, 2-b] indole-Based Acceptor–Donor–Acceptor Small Molecule, *European Journal of Organic Chemistry*, 2013 (2013) 5076-5084.
- [181] N.-T. Suen, S.-F. Hung, Q. Quan, N. Zhang, Y.-J. Xu, H.M. Chen, Electrocatalysis for the oxygen evolution reaction: recent development and future perspectives, *Chemical Society Reviews*, 46 (2017) 337-365.
- [182] F. Song, L. Bai, A. Moysiadou, S. Lee, C. Hu, L. Liardet, X. Hu, Transition metal oxides as electrocatalysts for the oxygen evolution reaction in alkaline solutions: an application-inspired renaissance, *Journal of the American Chemical Society*, 140 (2018) 7748-7759.
- [183] Y. Liu, V.C. Kravtsov, R. Larsen, M. Eddaoudi, Molecular building blocks approach to the assembly of zeolite-like metal–organic frameworks (ZMOFs) with extra-large cavities, *Chemical Communications*, (2006) 1488-1490.
- [184] C. Liu, J. Wang, J. Wan, C. Yu, MOF-on-MOF hybrids: Synthesis and applications, *Coordination Chemistry Reviews*, 432 (2021) 213743.
- [185] J. Liang, Z. Liang, R. Zou, Y. Zhao, Heterogeneous catalysis in zeolites, mesoporous silica, and metal–organic frameworks, *Advanced Materials*, 29 (2017) 1701139.
- [186] Z. Öztürk, M. Filez, B.M. Weckhuysen, Decoding nucleation and growth of zeolitic imidazolate framework thin films with atomic force microscopy and vibrational spectroscopy, *Chemistry–A European Journal*, 23 (2017) 10915-10924.
- [187] W. Zheng, M. Liu, L.Y.S. Lee, Electrochemical instability of metal–organic frameworks: in situ spectroelectrochemical investigation of the real active sites, *Acs Catalysis*, 10 (2019) 81-92.
- [188] M.M. Alsabban, X. Yang, W. Wahyudi, J.-H. Fu, M.N. Hedhili, J. Ming, C.-W. Yang, M.A. Nadeem, H. Idriss, Z. Lai, Design and Mechanistic Study of Highly Durable Carbon-Coated Cobalt Diphosphide Core–Shell Nanostructure Electrocatalysts for the Efficient and Stable Oxygen Evolution Reaction, *ACS applied materials & interfaces*, 11 (2019) 20752-20761.
- [189] M. Favaro, J. Yang, S. Nappini, E. Magnano, F.M. Toma, E.J. Crumlin, J. Yano, I.D. Sharp, Understanding the oxygen evolution reaction mechanism on CoO_x using operando ambient-pressure X-ray photoelectron spectroscopy, *Journal of the American Chemical Society*, 139 (2017) 8960-8970.

- [190] H. Wen, S. Zhang, T. Yu, Z. Yi, R. Guo, ZIF-67-based catalysts for oxygen evolution reaction, *Nanoscale*, 13 (2021) 12058-12087.
- [191] D. Sheberla, J.C. Bachman, J.S. Elias, C.-J. Sun, Y. Shao-Horn, M. Dincă, Conductive MOF electrodes for stable supercapacitors with high areal capacitance, *Nature materials*, 16 (2017) 220-224.
- [192] Q. Wang, D. Astruc, State of the art and prospects in metal–organic framework (MOF)-based and MOF-derived nanocatalysis, *Chemical reviews*, 120 (2019) 1438-1511.
- [193] F. Tian, A.M. Mosier, A. Park, E.R. Webster, A.M. Cerro, R.S. Shine, L. Benz, In situ measurement of CO₂ and H₂O adsorption by ZIF-8 films, *The Journal of Physical Chemistry C*, 119 (2015) 15248-15253.
- [194] C. Wu, D. Xie, Y. Mei, Z. Xiu, K.M. Poduska, D. Li, B. Xu, D. Sun, Unveiling the thermolysis natures of ZIF-8 and ZIF-67 by employing in situ structural characterization studies, *Physical Chemistry Chemical Physics*, 21 (2019) 17571-17577.
- [195] W. Zhang, X. Jiang, X. Wang, Y.V. Kaneti, Y. Chen, J. Liu, J.S. Jiang, Y. Yamauchi, M. Hu, Spontaneous weaving of graphitic carbon networks synthesized by pyrolysis of ZIF-67 crystals, *Angewandte Chemie*, 129 (2017) 8555-8560.
- [196] Q. Cheng, L. Yang, L. Zou, Z. Zou, C. Chen, Z. Hu, H. Yang, Single cobalt atom and N codoped carbon nanofibers as highly durable electrocatalyst for oxygen reduction reaction, *Acs Catalysis*, 7 (2017) 6864-6871.
- [197] Q. Wang, Y. Ji, Y. Lei, Y. Wang, Y. Wang, Y. Li, S. Wang, Pyridinic-N-dominated doped defective graphene as a superior oxygen electrocatalyst for ultrahigh-energy-density Zn–air batteries, *ACS Energy Letters*, 3 (2018) 1183-1191.